NASA Contractor Report 3147

Numerical Method for Predicting Flow Characteristics and Performance of Nonaxisymmetric Nozzles - Theory

P. D. Thomas

CONTRACT NAS1-15084
SEPTEMBER 1979

NASA

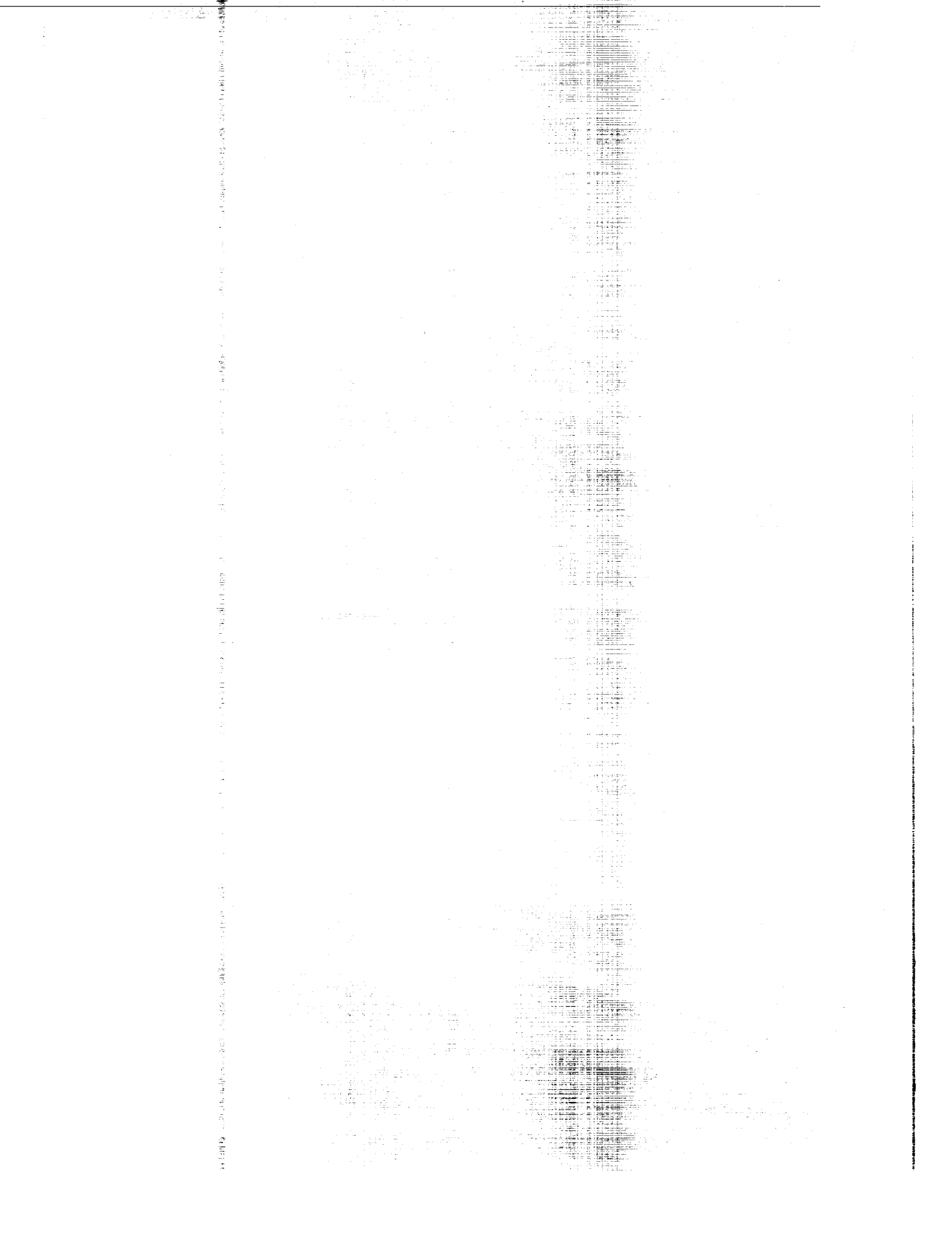

NASA Contractor Report 3147

Numerical Method for Predicting Flow Characteristics and Performance of Nonaxisymmetric Nozzles - Theory

P. D. Thomas
Lockheed Missiles & Space Company, Inc.
Palo Alto, California

Prepared for
Langley Research Center
under Contract NAS1-15084

National Aeronautics
and Space Administration

Scientific and Technical
Information Branch

1979

CONTENTS

ILLUSTRATIONS

Section 1

INTRODUCTION AND SUMMARY

1.1 OBJECTIVE

The objective of the work reported here is to develop a computer-implemented numerical method for predicting the flow characteristics and performance of three-dimensional jet exhaust nozzles. The immediate objective is to develop a method for an isolated nozzle. Both the internal exhaust gas flow and the external air flow with which it interacts are addressed. High Reynolds number turbulent flows are of primary interest for any combination of subsonic, transonic, and supersonic flow conditions inside or outside the nozzle. The method is designed to handle a variety of geometrically complex nozzle configurations, including nozzles that possess one plane of symmetry, two mutually perpendicular planes of symmetry, and nozzles with internal wedge plugs and external side plates. Of specific interest is the nonaxisymmetric nozzle configuration, illustrated in Fig. 1-1. The internal cross-sectional shape is circular at the entrance, is super-elliptical through a transition section, and becomes rectangular at the exit.

The author is indebted to Dr. Dieter K. Lezius, who provided the material on turbulence models that appears in Section 6, and to Mr. Jacques F. Middlecoff and Mrs. Karen L. Neier, who performed the bulk of the effort in programming the algorithm for computer solution.

1.2 APPROACH

The present approach has three primary features:

(1) A unified solution to the time-dependent Navier-Stokes equations in all regions of the flowfield and at all Mach numbers

(2) A general boundary-conforming curvilinear coordinate system and computational grid

(3) A fully implicit numerical method that is unconditionally stable with respect to the time step

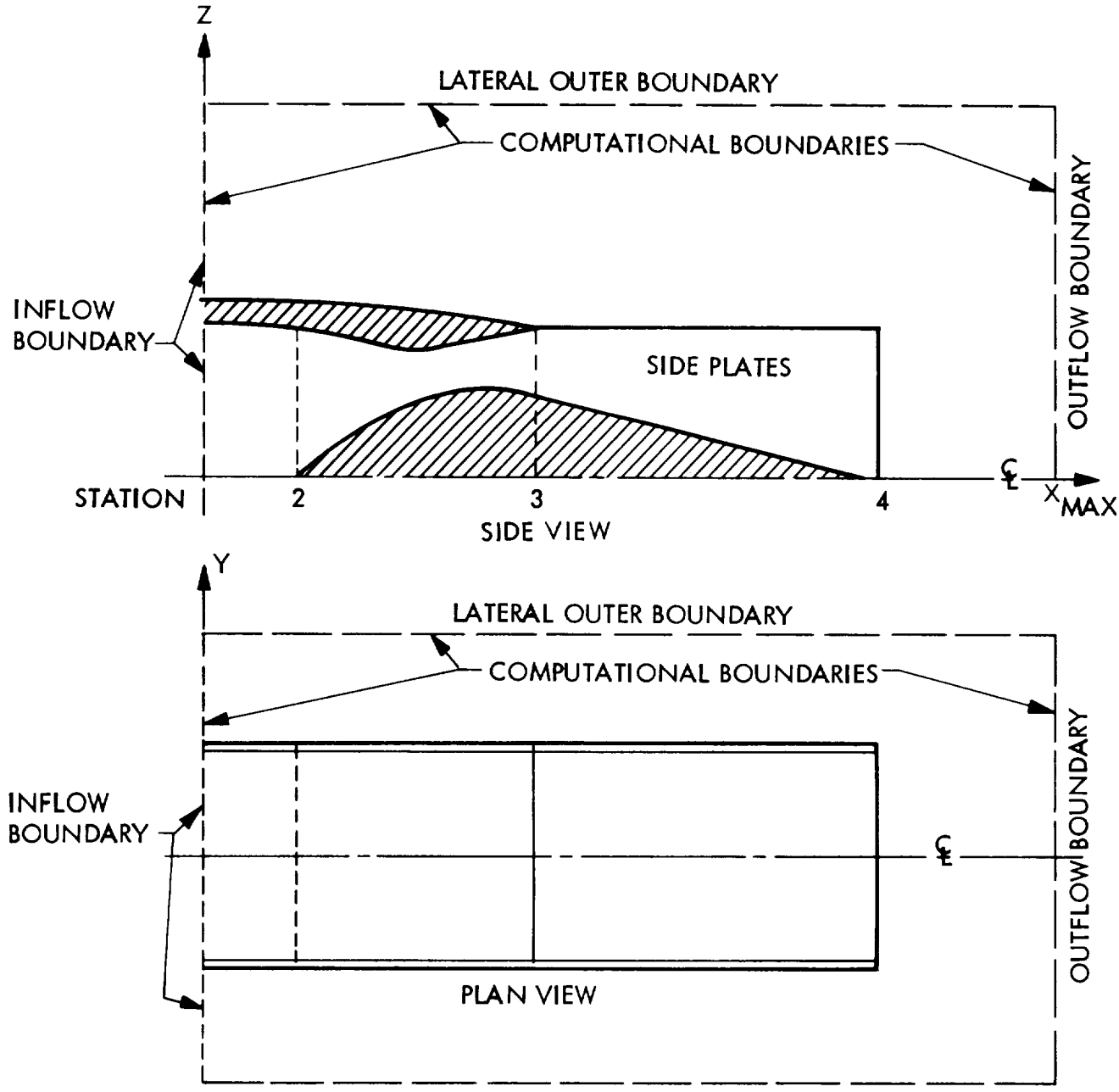

Fig. 1-1 Sketch of Nozzle Geometry and Computational Boundaries

The nozzle flows in question are steady. The approach adopted here yields the desired steady flow solution as the time-asymptotic limit of an unsteady flow. The implicit numerical method is applicable to the complete three-dimensional Navier-Stokes equations. However, in the interest of computational efficiency, we have elected to employ the "spatially parabolic" approximation in which the viscous transport processes in the general streamwise direction are neglected. The resulting equations retain all terms that are significant in wall boundary layers, whether separated or attached, and in free shear layers. They also retain all inviscid terms, so that predominantly inviscid regions of the flow are represented accurately.

The ability of the approximate equations to represent wall boundary layers and free shear layers accurately is of great importance for predicting the nozzle performance. Both the nozzle discharge coefficient and the thrust efficiency are strongly affected by the boundary layers; the former through blockage of the mean flow as a result of boundary layer displacement effects (viscous-inviscid interaction), and the latter by skin friction drag on all internal and external walls. For subsonic nozzle flow, the shear layer between the exhaust jet and the external stream may also affect the nozzle performance.

With this basic approach of solving the Navier-Stokes equations throughout the geometrically complex nozzle flow field, the use of some kind of implicit numerical method is essential for rational computation times with reasonable boundary-layer resolution. Virtually all nozzle internal and external flow conditions of interest are at high Reynolds numbers where the flow is turbulent and the boundary and shear layers are thin compared to a characteristic nozzle dimension. If one employs a finite-difference grid fine enough to accurately resolve the thin viscous layers, high computational efficiency can be achieved only with an implicit, unconditionally stable, numerical method. Explicit methods are inadequate because their conditional stability imposes severe limitations on the allowable time stepsize.

1.3 OVERVIEW OF THE REPORT

This report presents the theoretical foundation and formulation of the numerical method. A manual describing the computer program, its structure, and its application comprises a supplement to this report.

The basic equations and boundary conditions are presented in Section 2. The strong conservation-law form of the complete three-dimensional Navier-Stokes equations initially is formulated in Cartesian coordinates. However, a Cartesian coordinate system is entirely inappropriate for the geometrically complex nozzle configurations of interest. The equations are transformed to the equivalent strong conservation law form in a general system of curvilinear coordinates. One of the coordinates is oriented in the general streamwise direction, and the viscous transport processes in that direction are neglected (parabolic approximation).

The boundaries of the flow region in which the equations are solved are indicated schematically in Fig. 1-1. These include the nozzle walls, the symmetry planes, an upstream inflow boundary, a downstream outflow boundary, and one or more lateral outer boundaries. It is well known that the boundary conditions exert a dominant influence on the solution to any system of partial differential equations. The boundary conditions that are applied at the various boundary surfaces also are discussed in detail in Section 2.

In Section 3, the physical flow region depicted in Fig. 1-1 is mapped onto three-dimensional rectangular computational domain by a boundary-conforming curvilinear coordinate transformation. The transformation, i.e., the curvilinear coordinate system and computational grid, is generated numerically as the solution to an elliptic system of partial differential equations (Refs. 4, 10, 11, and 12). The boundary conditions for the elliptic system are the desired locations of the grid points that lie on the boundaries of the physical flow region. However, the original method has the shortcoming that, in practice, it is difficult to control the spacing between grid points

in the interior of the region. It is especially important to have good control over the interior grid spacing in the high Reynolds number flows of interest here, where adequate resolution of the steep flow variable gradients within wall boundary layers and free shear layers demands a locally refined grid.

The described shortcoming of the original method has been overcome. The modified method presented in Section 3 yields an elliptic system whose solution has the remarkable property that the grid point distribution in the interior of the flow region is controlled entirely by the selection of the grid point distribution along the boundaries.

The numerical method employed to solve the flow equations is discussed in detail in Section 4. The basic method employed at interior points of the grid is an implicit, non-iterative alternating-direction technique (Refs. 13 and 14). The accuracy of the numerical solution in the physical domain depends to a great extent on the accuracy which which the boundary conditions are represented numerically at the boundaries of the computational domain. In Section 4, we formulate implicit difference equations for the boundary grid points that are similar to those for interior points, but that embody the boundary conditions given in Section 2. The boundary point equations have the same time accuracy as the interior point equations, and are compatible with the latter in their spatial order of accuracy.

Section 5 presents the results of numerical experiments that have been conducted to test various aspects of the general method. A major portion of the experiments have been performed to develop and verify methods of computing the boundary conditions that are valid throughout the subsonic, transonic, and supersonic flow regimes. These experiments played a major role in the formulation of several of the boundary conditions given in Section 2, and of the boundary point difference equations given in Section 4.

Turbulence models that will be used to compute the effective viscosity coefficent μ and Prandtl number Pr in various subregions of the nozzle internal and external flowfield are discussed in Section 6.

Section 2

EQUATIONS AND BOUNDARY CONDITIONS

2.1 EQUATIONS IN CARTESIAN COORDINATES

The strong conservation-law form of the Navier-Stokes equations in Cartesian coordinates can be written in the compact vector notation

$$\vec{q}_t + \vec{f}_x + \vec{g}_y + \vec{h}_z = \vec{\sigma}_x + \vec{\theta}_y + \vec{\omega}_z$$

$$\vec{q} = (\rho,\ \rho u,\ \rho v,\ \rho w,\ \rho E)^T$$

$$\vec{f} = (\rho u,\ p + \rho u^2,\ \rho uv,\ \rho uw,\ \rho uH)^T$$

$$\vec{g} = (\rho v,\ \rho vu,\ p + \rho v^2,\ \rho vw,\ \rho vH)^T$$

$$\vec{h} = (\rho w,\ \rho wu,\ \rho wv,\ p + \rho w^2,\ \rho wH)^T$$

$$E = e + (u^2 + v^2 + w^2)/2$$

$$H = E + p/\rho \qquad (2.1)$$

where u, v, w are the velocity components in the coordinate directions x, y, z; ρ is the density p the pressure, e the specific internal energy; and $\vec{\sigma}$, $\vec{\theta}$, $\vec{\omega}$ represent the viscous stress and work terms for each coordinate direction. Presently available algebraic turbulence models generally assume that the first and second viscosity coefficients are related according to the Stokes hypothesis $\lambda = -2\,\mu/3$. The viscous stress, work, and heat conduction terms then can be written in terms of the turbulent viscosity μ and thermal conductivity k as follows.

$$\vec{\sigma} = \mu \begin{bmatrix} 0 \\ (2/3)\,(2u_x - v_y - w_z) \\ v_x + u_y \\ w_x + u_z \\ (2/3)\,u\,(2u_x - v_y - w_z) + v\,(v_x + u_y) + w\,(w_x + u_z) + (k/\mu)\,T_x \end{bmatrix} \tag{2.2a}$$

$$\vec{\theta} = \mu \begin{bmatrix} 0 \\ u_y + v_x \\ (2/3)\,(2v_y - u_x - w_z) \\ w_y + v_z \\ u\,(u_y + v_x) + (2/3)\,v\,(2v_y - u_x - w_z) + w\,(w_y + v_z) + (k/\mu)\,T_y \end{bmatrix} \tag{2.2b}$$

$$\vec{\omega} = \mu \begin{bmatrix} 0 \\ u_z + w_x \\ v_z + w_y \\ (2/3)\,(2w_z - u_x - v_y) \\ u\,(u_z + w_x) + v\,(v_z + w_y) + (2/3)\,w\,(2w_z - u_x - v_y) + (k/\mu)\,T_z \end{bmatrix} \tag{2.2c}$$

Equations (2.1) are supplemented by the equation of state which, for a thermally and calorically perfect gas, may be written in the form

$$p/\rho = RT = (\gamma - 1)\,e = c^2/\gamma \tag{2.3}$$

where R is the gas constant, γ is the specific heat ratio, and c is the speed of sound.

2.1.1 Non-Dimensionalization

The foregoing equations can be cast in dimensionless form by introducing the normalized flow variables

$$\bar{\rho} = \rho/\rho_\infty \quad , \quad \bar{p} = p/p_\infty \quad , \quad \bar{T} = T/T_\infty \quad , \quad \bar{\mu} = \mu/\mu_\infty$$

$$(\bar{u}, \bar{v}, \bar{w}) = (u, v, w)/c_\infty \quad , \quad \bar{\epsilon} = \rho E/\rho_\infty c_\infty^2$$

$$(\bar{x}, \bar{y}, \bar{z}) = (x, y, z)/L \quad , \quad \bar{t} = c_\infty t/L \tag{2.4}$$

where L is a reference length scale and the subscript ∞ denotes some convenient reference state. We define the Reynolds and Mach numbers at the reference state as

$$Re_\infty = \rho_\infty V_\infty L/\mu_\infty \qquad M_\infty = V_\infty/c_\infty \tag{2.5}$$

where $V_\infty = \sqrt{u_\infty^2 + v_\infty^2 + w_\infty^2}$. Equations (2.1) to (2.3) then assume the dimensionless form given below, where we have suppressed the overbars for simplicity. Eqs. (2.6) and all equations throughout the remainder of the report are written in dimensionless variables.

$$\vec{q}_t + \vec{f}_x + \vec{g}_y + \vec{h}_z = Re^{-1} (\vec{\sigma}_x + \vec{\theta}_y + \vec{\omega}_z) \tag{2.6a}$$

$$c^2 = p/\rho = T = \gamma (\gamma - 1) (\epsilon/\rho - V^2/2) \tag{2.6b}$$

where

$$
\begin{aligned}
Re &= Re_\infty / M_\infty \\
Pr &= \mu c_p / k \\
\vec{q} &= (\rho,\ \rho u,\ \rho v,\ \rho w,\ \epsilon)^T \\
\vec{f} &= [\rho u,\ (p/\gamma + \rho u^2),\ \rho uv,\ \rho uw,\ u\,(p/\gamma + \epsilon)]^T \\
\vec{g} &= [\rho v,\ \rho vu,\ (p/\gamma + \rho v^2),\ \rho vw,\ v\,(p/\gamma + \epsilon)]^T \\
\vec{h} &= [\rho w,\ \rho wu,\ \rho wv,\ (p/\gamma + \rho w^2),\ w\,(p/\gamma + \epsilon)]^T
\end{aligned}
\tag{2.7}
$$

$$
\vec{\sigma} = \mu \begin{bmatrix}
0 \\
(2/3)\,(2u_x - v_y - w_z) \\
v_x + u_y \\
w_x + u_z \\
(2/3)\,u\,(2u_x - v_y - w_z) + v\,(v_x + u_y) + w\,(w_x + u_z) + [(\gamma - 1)\,Pr]^{-1} T_x
\end{bmatrix}
$$

$$
\vec{\theta} = \mu \begin{bmatrix}
0 \\
u_y + v_x \\
(2/3)\,(2v_y - u_x - w_z) \\
w_y + v_z \\
u\,(u_y + v_x) + (2/3)\,v\,(2v_y - u_x - w_z) + w\,(w_y + v_z) + [(\gamma - 1)Pr]^{-1} T_y
\end{bmatrix}
$$

$$\vec{\omega} = \mu \begin{bmatrix} 0 \\ u_z + w_x \\ v_z + w_y \\ (2/3)\,(2\,w_z - u_x - v_y) \\ u\,(u_z + w_x) + v\,(v_z + w_y) + (2/3)\,w\,(2\,w_z - u_x - v_y) + [(\gamma - 1)\mathrm{Pr}]^{-1}\,T_z \end{bmatrix}$$

2.2 TRANSFORMATION TO GENERAL CURVILINEAR COORDINATES

The task of solving Eqs. (2.6) numerically within a given flow region R bounded by a closed surface S is simplified greatly by transforming the equations to a new boundary-conforming curvilinear coordinate system (Refs. 1 to 5). Here, a boundary-conforming coordinate system is one in which the boundary surface S is a coordinate surface.

We introduce a time-dependent invertible mapping transformation of R onto boundary conforming curvilinear coordinates (Refs. 3 to 6). Here the precise meaning of the

$$x,\ y,\ z,\ t \underset{T^{-1}}{\overset{T}{\rightleftharpoons}} \xi,\ \eta,\ \zeta, \tau \qquad \begin{aligned} \xi &= \xi\,(x, y, z, t) \\ \eta &= \eta\,(x, y, z, t) \\ \zeta &= \zeta\,(x, y, z, t) \\ \tau &= t \end{aligned} \qquad (2.8)$$

term "boundary-conforming" is that, in these coordinates, the boundary S is composed only of segments of coordinates surfaces ξ = const., η = const., ζ = const. That is,

the surface S has the time-invariant functional representation $f(\xi, \eta, \zeta) = 0$ independently of time, τ. The mapping otherwise may be arbitrarily defined if it is invertible and satisfies this constraint.

In applying this transformation to Eq. (2.6a) one usually retains the dependent variables associated with the original Cartesian coordinate system.

Upon transforming to ξ, η, ζ coordinates with the aid of the chain rule for partial derivatives, Eq. (2.6a) becomes (Refs. 3 to 7))

$$\hat{q}_\tau + \hat{\vec{f}}_\xi + \hat{g}_\eta + \hat{h}_\zeta = Re^{-1}\left(\hat{\sigma}_\xi + \hat{\theta}_\eta + \hat{\omega}_\zeta\right)$$

$$\begin{aligned}
\hat{q} &= J\vec{q} \\
\hat{f} &= \hat{\xi}_t \vec{q} + \hat{\xi}_x \vec{f} + \hat{\xi}_y \vec{g} + \hat{\xi}_z \vec{h} \\
\hat{g} &= \hat{\eta}_t \vec{q} + \hat{\eta}_x \vec{f} + \hat{\eta}_y \vec{g} + \hat{\eta}_z \vec{h} \\
\hat{h} &= \hat{\zeta}_t \vec{q} + \hat{\zeta}_x \vec{f} + \hat{\zeta}_y \vec{g} + \hat{\zeta}_z \vec{h} \\
\hat{\sigma} &= \hat{\xi}_x \vec{\sigma} + \hat{\xi}_y \vec{\theta} + \hat{\xi}_z \vec{\omega} \\
\hat{\theta} &= \hat{\eta}_x \vec{\sigma} + \hat{\eta}_y \vec{\theta} + \hat{\eta}_z \vec{\omega} \\
\hat{\omega} &= \hat{\zeta}_x \vec{\sigma} + \hat{\zeta}_y \vec{\theta} + \hat{\zeta}_z \vec{\omega}
\end{aligned} \tag{2.9}$$

where J is the Jacobian of the inverse transformation T^{-1}

$$J = \frac{\partial(x, y, z)}{\partial(\xi, \eta, \zeta)} \tag{2.10}$$

and where

$$\hat{\xi}_t = J\xi_t \quad , \quad \hat{\xi}_x = J\xi_x \quad , \quad \hat{\xi}_y = J\xi_y \quad , \quad \text{etc.} \tag{2.11}$$

We observe that Eq. (2.6a) transforms into Eq. (2.9) only if the mapping functions (2.8) satisfy identically the following relations (Ref. 6)

$$\hat{\xi}_{x\xi} + \hat{\eta}_{x\eta} + \hat{\zeta}_{x\zeta} = 0 \tag{2.12a}$$

$$\hat{\xi}_{y\xi} + \hat{\eta}_{y\eta} + \hat{\zeta}_{y\zeta} = 0 \tag{2.12b}$$

$$\hat{\xi}_{z\xi} + \hat{\eta}_{z\eta} + \hat{\zeta}_{z\zeta} = 0 \tag{2.12c}$$

$$J_\tau + \hat{\xi}_{t\xi} + \hat{\eta}_{t\eta} + \hat{\zeta}_{t\zeta} = 0 \tag{2.13}$$

One can verify by direct calculation that these relations hold analytically as long as the mapping functions possess continuous second partial derivatives.

The mapping functions (2.8) need not be known analytically in order to obtain numerical solutions to the transformed Navier-Stokes equations (2.9). Once the ξ, η, ζ computational domain is covered by a finite-difference grid, the inverse transformation T^{-1} can be defined numerically in terms of the Cartesian coordinates $x(\tau)$, $y(\tau)$, $z(\tau)$ of the grid points, from which the partial derivatives x_τ, y_τ, x_ξ, y_ξ, etc., are computed by using difference formulas. The coefficients that appear in Eq. (2.9) then can be evaluated from the following identities (Ref. 6):

$$
\begin{aligned}
\hat{\xi}_x &= y_\eta z_\zeta - y_\zeta z_\eta & \hat{\eta}_x &= y_\zeta z_\xi - y_\xi z_\zeta \\
\hat{\xi}_y &= z_\eta x_\zeta - z_\zeta x_\eta & \hat{\eta}_y &= z_\zeta x_\xi - z_\xi x_\zeta \\
\hat{\xi}_z &= x_\eta y_\zeta - x_\zeta y_\eta & \hat{\eta}_z &= x_\zeta y_\xi - x_\xi y_\zeta \\
\hat{\zeta}_x &= y_\xi z_\eta - y_\eta z_\xi & \hat{\xi}_t &= -(\hat{\xi}_x x_\tau + \hat{\xi}_y y_\tau + \hat{\xi}_z z_\tau) \\
\hat{\zeta}_y &= z_\xi x_\eta - z_\eta x_\xi & \hat{\eta}_t &= -(\hat{\eta}_x x_\tau + \hat{\eta}_y y_\tau + \hat{\eta}_z z_\tau) \\
\hat{\zeta}_z &= x_\xi y_\eta - x_\eta y_\xi & \hat{\zeta}_t &= -(\hat{\zeta}_x x_\tau + \hat{\zeta}_y y_\tau + \hat{\zeta}_z z_\tau)
\end{aligned}
\qquad (2.14)
$$

Care must be exercised, however, to ensure that the finite-difference representation of the spatial derivatives x_ξ, y_ξ, x_η, $\hat{f}_\xi$, $\hat{g}_\eta$, etc. is such that the identities (2.12) hold true numerically (Ref. 7). Similarly, for time-dependent transformations associated with moving boundaries, special measures must be taken to ensure that Eq. (2.13), the "Geometric Conservation Law," also is satisfied numerically (Ref. 6). The reason lies in the fact that violation of any of Eqs. (2.12) or (2.13) induces first-order numerical errors in conservation of mass, momentum and energy.

2.3 PARABOLIC APPROXIMATION

For the nozzle flow problems of present interest, we shall assume that both the Cartesian and the curvilinear coordinate systems are oriented with the x and ξ axes running in the general streamwise flow direction. Because the dominant viscous effects are associated with the cross-stream directions η, ζ, we may employ the so-called "parabolic approximation." In this approximation, we simply neglect all viscous terms in the R. H. S. of Eq. (2.9) that involve derivatives with respect to ξ. Before doing so, however, we shall examine the structure of the viscous terms.

Consider, for example, the quantity $\hat{\theta}$ defined in (2.9). Upon inserting $\vec{\sigma}$, $\vec{\theta}$, $\vec{\omega}$ as defined below Eq. (2.7) and transforming to ξ, η, ζ coordinates with the chain

rule, one finds that the resulting equation can be split naturally into three terms, each of which contains derivatives in a single coordinate direction

$$\hat{\theta} = \hat{\theta}^{(\xi)} + \hat{\theta}^{(\eta)} + \hat{\theta}^{(\zeta)} \tag{2.15}$$

$$\hat{\theta}^{(\xi)} = \mu J \begin{bmatrix} 0 \\ (\nabla\eta \cdot \nabla\xi) u_\xi + (\xi_x \nabla\eta - 2/3\, \eta_x \nabla\xi) \cdot \vec{V}_\xi \\ (\nabla\eta \cdot \nabla\xi) v_\xi + (\xi_y \nabla\eta - 2/3\, \eta_y \nabla\xi) \cdot \vec{V}_\xi \\ (\nabla\eta \cdot \nabla\xi) w_\xi + (\xi_z \nabla\eta - 2/3\, \eta_z \nabla\xi) \cdot \vec{V}_\xi \\ (\nabla\eta \cdot \nabla\xi) [T/(\gamma - 1)\mathrm{Pr} + V^2/2]_\xi + [(\vec{V} \cdot \nabla\xi)\nabla\eta - 2/3\, (\vec{V} \cdot \nabla\eta)\nabla\xi] \cdot \vec{V}_\xi \end{bmatrix} \tag{2.16a}$$

$$\hat{\theta}^{(\eta)} = \mu J \begin{bmatrix} 0 \\ (\nabla\eta \cdot \nabla\eta) u_\eta + 1/3\, \eta_x (\nabla\eta \cdot \vec{V}_\eta) \\ (\nabla\eta \cdot \nabla\eta) v_\eta + 1/3\, \eta_y (\nabla\eta \cdot \vec{V}_\eta) \\ (\nabla\eta \cdot \nabla\eta) w_\eta + 1/3\, \eta_z (\nabla\eta \cdot \vec{V}_\eta) \\ (\nabla\eta \cdot \nabla\eta) [T/(\gamma - 1)\mathrm{Pr} + V^2/2]_\eta + 1/3\, (\vec{V} \cdot \nabla\eta)(\nabla\eta \cdot \vec{V}_\eta) \end{bmatrix} \tag{2.16b}$$

$$\hat{\theta}^{(\zeta)} = \mu J \begin{bmatrix} 0 \\ (\nabla\eta \cdot \nabla\zeta) u_\zeta + (\xi_x \nabla\eta - 2/3\, \eta_x \nabla\zeta) \cdot \vec{V}_\zeta \\ (\nabla\eta \cdot \nabla\zeta) v_\zeta + (\xi_y \nabla\eta - 2/3\, \eta_y \nabla\zeta) \cdot \vec{V}_\zeta \\ (\nabla\eta \cdot \nabla\zeta) w_\zeta + (\xi_z \nabla\eta - 2/3\, \eta_z \nabla\zeta) \cdot \vec{V}_\zeta \\ (\nabla\eta \cdot \nabla\zeta) [T/(\gamma - 1)\mathrm{Pr} + V^2/2]_\zeta + [(\vec{V} \cdot \nabla\zeta)\nabla\eta - 2/3\, (\vec{V} \cdot \nabla\eta)\nabla\zeta] \cdot \vec{V}_\zeta \end{bmatrix} \tag{2.16c}$$

where standard Cartesian vector notation is used:

$$\vec{V} = (u, v, w) \quad , \quad V = |\vec{V}| \quad , \quad \vec{V}_\eta = (u_\eta, v_\eta, w_\eta)$$

$$\nabla\eta = (\eta_x, \eta_y, \eta_z) \quad , \quad \text{etc.}$$

Equations (2.15) and (2.16) have useful symmetry properties. For example, Eq. (2.16b) defining $\hat{\theta}^{(\eta)}$ can be deduced directly from $\hat{\theta}^{(\xi)}$ in (2.16a) by making the simple substitution $\xi \rightarrow \eta$. Similarly, $\hat{\theta}^{(\zeta)}$ in Eq. (2.16c) can be obtained from (2.16a) by making the substitution $\xi \rightarrow \zeta$.

The transformed viscous terms $\hat{\sigma}$ and $\hat{\omega}$ each can be split in analogous fashion:

$$\hat{\omega} = \hat{\omega}^{(\xi)} + \hat{\omega}^{(\eta)} + \hat{\omega}^{(\zeta)} \tag{2.17}$$

$$\hat{\sigma} = \hat{\sigma}^{(\xi)} + \hat{\sigma}^{(\eta)} + \hat{\sigma}^{(\zeta)} \tag{2.18}$$

The individual terms in (2.17) can be deduced from Eq. (2.16) by making the substitutions $\theta \rightarrow \omega$, $\eta \rightarrow \zeta$. Similarly, the terms in (2.18) can be deduced from (2.16) by substitution of $\theta \rightarrow \sigma$, $\eta \rightarrow \xi$.

With Eqs. (2.15) through (2.18) in hand, we obtain the parabolic approximation simply by neglecting all ξ-differentiated terms

$$\hat{\sigma}_\xi = \hat{\theta}^{(\xi)} = \hat{\omega}^{(\xi)} = 0 \tag{2.19}$$

The Navier-Stokes equations (2.9) then reduce to

$$\hat{q}_\tau + \hat{f}_\xi + \hat{g}_\eta + \hat{h}_\zeta = Re^{-1} \left\{ \left[\hat{\theta}^{(\eta)} + \hat{\theta}^{(\zeta)} \right]_\eta + \left[\hat{\omega}^{(\eta)} + \omega^{(\zeta)} \right]_\zeta \right\} \tag{2.20}$$

2.4 CURVILINEAR COORDINATE GEOMETRY AND BOUNDARY CONDITIONS

2.4.1 Coordinate Geometry

Equation (2.20) is to be solved numerically, subject to certain admissible boundary conditions that must be satisfied on the various computational boundaries illustrated in Fig. 1-1. The curvilinear coordinate system (ξ, η, ζ) is defined such that the computational boundaries coincide with coordinate surfaces. We shall restrict attention to nozzle configurations that have either one plane of symmetry $y = 0$, or two mutually perpendicular symmetry planes $y = 0$ and $z = 0$. The two types of configuration are illustrated in Fig. 2-1. The curvilinear coordinate system, which may be nonorthogonal, is oriented so that the ξ coordinate runs in the general streamwise direction. For convenience, the family of coordinate surfaces ξ = const. generally will be taken as planes normal to the Cartesian X-axis.

The upstream inflow and downstream outflow boundaries are defined to be members of this family ξ = const. (Fig. 1-1). The boundary-conforming cross-stream coordinates η, ζ are defined so that all nozzle walls either are members of one or the other of the two families of coordinate surfaces η = const. or ζ = const. or are composed of intersecting segments of both families η = const. and ζ = const. The lateral outer computational boundary is defined in similar fashion as a surface η = const. or ζ = const., or as a composite of the two. The symmetry planes are also members of one of the latter families. For example, the symmetry plane in Fig. 2-1a is represented as a surface η = const., whereas in Fig. 2-1b, one symmetry plane is a surface η = const., and the other is a surface ζ = const. The boundary conditions that hold at the various boundary surfaces are as follows.

2.4.2 Wall Boundary Conditions

At the nozzle walls, the velocity vector must vanish and either the wall temperature T_w or heat flux Q_w may be specified. For the latter, we restrict attention to the adiabatic wall case $Q_w = 0$.

$$u = v = w = 0 \tag{2.21}$$

and

$$T = T_w \tag{2.22}$$

or

$$-k(\vec{n} \cdot \nabla T) = 0 \tag{2.23a}$$

where $\vec{n}$ is the local vector normal to the wall. For a wall that coincides with the surface η = const., the normal vector is $\vec{n} = \nabla\eta$, and Eq. (2.23a) becomes

$$\nabla\eta \cdot \nabla T = (\nabla\eta \cdot \nabla\xi)\, T_\xi + (\nabla\eta \cdot \nabla\eta)\, T_\eta + (\nabla\eta \cdot \nabla\zeta)\, T_\zeta = 0$$

However, the term involving T_ξ is neglected in the parabolic approximation, and the adiabatic wall boundary condition is then

$$(\nabla\eta \cdot \nabla\eta)\, T_\eta + (\nabla\eta \cdot \nabla\zeta)\, T_\zeta = 0 \tag{2.23b}$$

The corresponding boundary condition for an adiabatic wall that coincides with the surface ζ = const. (see Fig. 2-1a) can be deduced from (2.23b) by making the substitution $\eta \rightarrow \zeta, \zeta \rightarrow \eta$.

2.4.3 Symmetry Boundary Conditions

At a symmetry plane, the normal component of velocity is an odd function of position relative to the plane, whereas all other flow variables are even functions. The Cartesian coordinates also are either even or odd at a symmetry plane. For example, at the symmetry plane $\eta = 0$ in Fig. 2-1a, y and v are odd functions of η; whereas x, z, and all flow variables other than v are even

$$y(-\eta) = -y(\eta) \quad , \quad v(-\eta) = -v(\eta) \tag{2.24a}$$

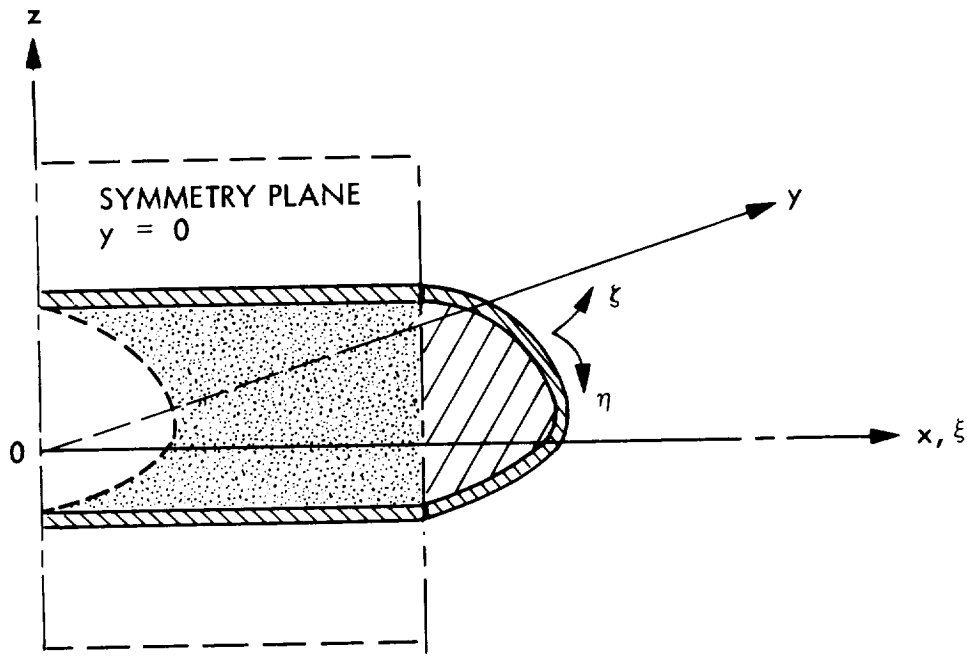

Fig. 2-1a Configuration With One Symmetry Plane

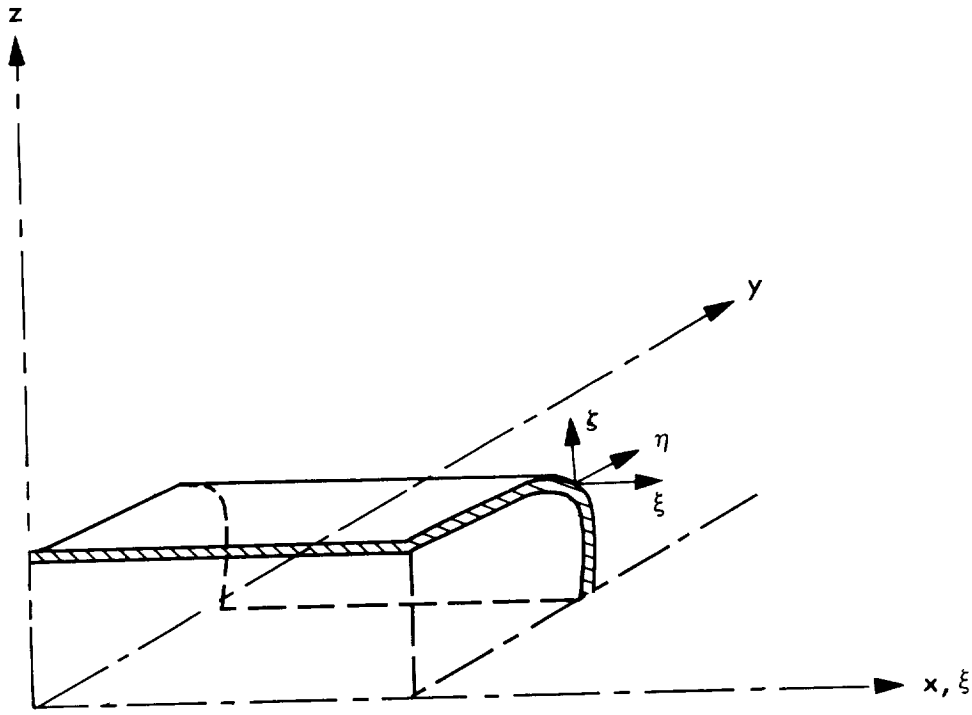

Fig. 2-1b Configuration With Two Symmetry Planes

$$x(-\eta) = x(\eta) \quad , \quad z(-\eta) = z(\eta) \quad , \quad u(-\eta) = u(\eta)$$
$$w(-\eta) = w(\eta) \quad , \quad \rho(-\eta) = \rho(\eta) \quad , \quad \text{etc.} \tag{2.24b}$$

As is well known, any odd function of η must vanish at $\eta = 0$.

This information can be used in Eq. (2.20) to evaluate the η-differentiated terms at the symmetry plane $\eta = 0$. One need only apply the well-known theorem which states that the derivative of an even function is odd, the derivative of an odd function is even, the product of an even and an odd function is odd, and the product of two even or of two odd functions is even.

It then follows from Eq. (2.24) that, for each of the vectors $\hat{g}$, $\hat{\theta}^{(\eta)}$, and $\hat{\theta}^{(\zeta)}$, the third component is even, whereas the other four components are odd functions of η. The derivative of the third component thus is odd, and hence must vanish at $\eta = 0$.

$$\left(\hat{g}_3\right)_\eta = \left[\hat{\theta}_3^{(\eta)}\right]_\eta = \left[\hat{\theta}_3^{(\zeta)}\right]_\eta = 0 \qquad \text{at} \qquad \eta = 0 \tag{2.25}$$

The derivatives of the other four components are even, and can be evaluated in the one-sided sense. For example, for the first component of $\hat{g}$, we have

$$\left(\hat{g}_1\right)_\eta = \left(\hat{g}_1\right)_{\eta+} = \lim_{\eta \to 0+} \left[\frac{\hat{g}_1(\eta) - \hat{g}_1(0)}{\eta}\right] \tag{2.26}$$

The horizontal symmetry plane $\zeta = 0$ in Fig. 2-1b can be treated in similar fashion.

2.4.4 Freestream Boundary Conditions

If the external freestream conditions are selected as the non-dimensionalizing reference conditions in Eqs. (2.4), then the following boundary conditions must be satisfied in the asymptotic sense at infinite distance from the nozzle:

$$p = 1 \quad , \quad \rho = 1 \quad , \quad u = u_\infty \tag{2.27a}$$

$$\hat{\theta}(\eta) = \hat{\theta}(\zeta) = \hat{\omega}(\eta) = \hat{\omega}(\zeta) = 0 \tag{2.27b}$$

It is assumed that the x-axis is aligned with the freestream velocity vector, so that $v_\infty = w_\infty = 0$. In practice, boundary conditions (2.27) must be applied at lateral outer computational boundary located a finite distance from the nozzle (Fig. 1-1), and it is not always permissible to impose the remaining freestream conditions $v = w = 0$ at that boundary. Numerical experiments have shown difficulties in converging to a time-asymptotic steady state solution for subsonic and transonic flow when the latter conditions are imposed (see Section 5). In general, the velocity components v and w must be computed at the boundary as well as in the interior flow region.

2.4.5 Upstream Inflow Boundary Conditions

To discover what boundary conditions are permissible at the inflow boundary, we appeal to the quasi-one-dimensional unsteady method of characteristics applied to Eq. (2.20). According to the method, the five-component vector equation (2.20) is regarded as a hyperbolic system of partial differential equations in τ and ξ. The η and ζ differentiated terms are treated simply as inhomogeneous "forcing function" terms. The analysis is cumbersome; we shall omit the details and merely summarize the major results for the case where $\xi = \xi(x)$ only, i.e., where the inflow boundary is a plane normal to the x-axis.

The hyperbolic system of five scalar equations has three distinct characteristics $\lambda_i = d\xi/d\tau$, one of which is of multiplicity three

$$\begin{aligned} \lambda_1 = \lambda_2 = \lambda_3 &= u\xi_x \\ \lambda_4 &= (u + c)\,\xi_x \\ \lambda_5 &= (u - c)\,\xi_x \end{aligned} \tag{2.28}$$

where $\xi_x > 0$ for any non-singular coordinate transformation (2.6). The characteristic form of the system is

$$v_\tau + \lambda_1 v_\xi = f_1 \tag{2.29a}$$

$$w_\tau + \lambda_1 w_\xi = f_2 \tag{2.29b}$$

$$(p_\tau + \lambda_3 p_\xi) - c^2(\rho_\tau + \lambda_3 \rho_\xi) = f_3 \tag{2.29c}$$

$$(p_\tau + \lambda_4 p_\xi) + \rho c(u_\tau + \lambda_4 u_\xi) = f_4 \tag{2.29d}$$

$$(p_\tau + \lambda_5 p_\xi) - \rho c(u_\tau + \lambda_5 u_\xi) = f_5 \tag{2.29e}$$

where $f_1, f_2, \ldots$ are cumbersome functions of the flow variables and of the η- and ζ- differentiated terms in (2.20), and where the operators

$$\frac{\partial}{\partial \tau} + \lambda_i \frac{\partial}{\partial \xi}$$

represent directional derivatives along the characteristics.

If u is supersonic ($u > c$), all five characteristics (2.28) have positive slope in the $\xi - \tau$ plane; i.e., all characteristics are directed downstream. We conclude that all flow variables may be specified a priori as inflow boundary conditions whenever $u > c$.

For subsonic inflow $u < c$, all characteristics remain of positive slope except λ_5, which has negative slope. Information propagates upstream along that characteristic from the interior of the flow region toward the inflow boundary, and the last of Eqs. (2.29) yields one relation among the five independent flow variables. Thus, four independent quantities may be specified as boundary conditions. Of these, one sees from Eqs. (2.29a,b) that two must specify the transverse velocity components or, equivalently, the velocity vector's direction cosines. It appears that some freedom exists in the choice of the remaining two boundary conditions. However, Eq. (2.29c) may be recognized as the isentropic relation between pressure and density perturbations

along a "streamline." This suggests that the entropy or, equivalently, the stagnation pressure, may be specified as an inflow boundary condition. On physical grounds, we elect to specify the stagnation temperature as the remaining inflow boundary condition.

The boundary conditions on the stagnation pressure $p_o(\xi = 0, \eta, \zeta)$ and stagnation temperature $T_o(\xi = 0, \eta, \zeta)$ provide two independent algebraic relations among the local values of the flow variables at each point of the inflow boundary $\xi = 0$. These relations can be represented in terms of the particle-isentropic flow equations

$$T_o/T = 1 + (\gamma - 1)M^2/2$$

$$p/p_o = (T/T_o)^{\gamma/(\gamma-1)}$$

where $M^2 = V^2/T$ is the local Mach number written in terms of the dimensionless velocity and temperature [Eqs. (2.4)]. With the aid of the equation of state (2.6b), these relations can be written in the form

$$T_o = (\gamma - 1)\left[\gamma\epsilon/\rho - (\gamma - 1)V^2/2\right] \tag{2.30a}$$

$$p_o = \rho T_o \left\{\gamma\left[1/(\gamma - 1) - \epsilon/\rho T_o\right]\right\}^{-1/(\gamma-1)} \tag{2.30b}$$

The described inflow boundary condition results for the three-dimensional "parabolized" Navier-Stokes equations (2.20) are essentially the same as those presented in Ref. 8 for two-dimensional inviscid flow.

2.4.6 Downstream Outflow Boundary

Arguments similar to those given above for the upstream inflow boundary may be used at the outflow boundary. For $u > c$, all characteristics have positive slope and emanate from the interior toward the boundary. The flow variables at the boundary are completely determined by the interior flow, and no boundary conditions may be

specified. For $u < c$, the single characteristic λ_5 emanates from the boundary, and one boundary condition may be specified. It is common to specify the pressure as equal to its freestream value (Refs. 8 and 9).

$$p = 1 \qquad \text{when} \qquad u < c \tag{2.31}$$

However, we shall employ this boundary condition only when dealing with the internal flow in an isolated nozzle; that is, when the outflow boundary is located at the nozzle exit plane. For general cases involving both internal and external flow where the outflow boundary is located downstream of the nozzle exit, we shall specify no outflow boundary conditions. All flow variables at the outflow boundary will be computed from Eqs. (2.20) as described in section 4.2.2. This approach has the following justification.

The system (2.20) is not strictly hyperbolic because the viscous terms on the R.H.S. have parabolic qualities. Parabolic systems may be viewed as possessing degenerate vertical characteristics $d\xi/d\tau = 0$ along which information is propagated instantaneously from the lateral outer boundary. Freestream pressure is imposed at the latter boundary [see Eq. (2.27a)], and we rely on the parabolic behavior of the equations to relay the freestream pressure information to all points of the outflow boundary. The numerical experiments described in Section 5 attest to the validity of this approach.

Section 3

GENERATION OF COMPUTATIONAL GRIDS

The generation of computational grids suitable for carrying out accurate numerical solutions to the three-dimensional Navier-Stokes equations is currently the subject of intensive research. For a wide class of nozzle configurations that includes the configuration depicted in Fig. 1-1, a three-dimensional grid can be built up by constructing a sequence of two-dimensional grids in successive cross-sectional planes. For each cross-sectional plane between the upstream inflow boundary and the nozzle exit, a two-dimensional grid must be generated both for the flow region internal to the nozzle and for the flow region outside the nozzle. The two flow regions are illustrated in Fig. 3-1a for a nozzle whose interior and exterior walls have a super-elliptical shape described by the equation

$$(y/a)^N + (z/b)^N = 1 \qquad (3.1)$$

where a, b, and N may vary with position, x, along the nozzle. For the present, we shall restrict attention to nozzle configurations that have two mutually perpendicular planes of symmetry, and shall assume that the Cartesian coordinate system is oriented so that the symmetry planes coincide with the coordinate planes $y = 0$ and $z = 0$, respectively.

Two substantial advantages are gained by introducing a boundary-conforming curvilinear coordinate transformation that maps the physical flow region in the cross-sectional plane (y, z) onto a rectangular computational domain (η, ξ). First, a uniform rectangular grid can be employed in the (η, ξ) domain that simplifies the numerical finite-difference representation of the flow equations. Second, the boundary conditions can be computed more easily and more accurately. Because of the boundary-

conforming character of the mapping transformation peripheral grid points lie directly on the boundaries. This avoids the tedious and inaccurate interpolation or extrapolation procedures that would be required to compute or to impose boundary conditions when the boundaries lie between grid points.

Thompson, Thames, and Mastin (Ref. 4) have given a general method for generating such boundary-conforming coordinate transformations. In the method, one computes the (y, z) coordinates of the grid points in physical space as solutions to an elliptic system of partial differential equations. The equations are formulated in a rectangular computational domain (η, ζ), and are solved numerically over a uniform, rectangular grid in that domain.

Figure 3-2 shows an example of such a mapping of the region interior to the nozzle of Fig. 3-1 onto a rectangular (η, ζ) computational domain. Points A, B, C of Fig. 3-1 map onto the corners A', B', C' of the computational domain in Fig. 3-2, where the point B is placed at the location where the curvature of the nozzle wall is greatest. This mapping produces a quasi-rectangular grid in the physical domain of Fig. 3-1 when the Thompson, Thames, Mastin (TTM) method is applied to generate the grid numerically. The TTM method employs the following inhomogeneous Laplace equations as the generating system

$$\begin{aligned} \eta_{yy} + \eta_{zz} &= P(\eta, \zeta) \\ \zeta_{yy} + \zeta_{zz} &= Q(\eta, \zeta) \end{aligned} \tag{3.2}$$

These equations are transformed to ζ, η coordinates by interchanging the roles of dependent and independent variables. This yields an elliptic system of quasilinear equations

$$\alpha y_{\eta\eta} - 2\beta y_{\eta\zeta} + \gamma y_{\zeta\zeta} = -J^2 (P y_{\eta} + Q y_{\zeta})$$

$$\alpha z_{\eta\eta} - 2\beta z_{\eta\zeta} + \gamma z_{\zeta\zeta} = -J^2 (P z_{\eta} + Q z_{\zeta})$$

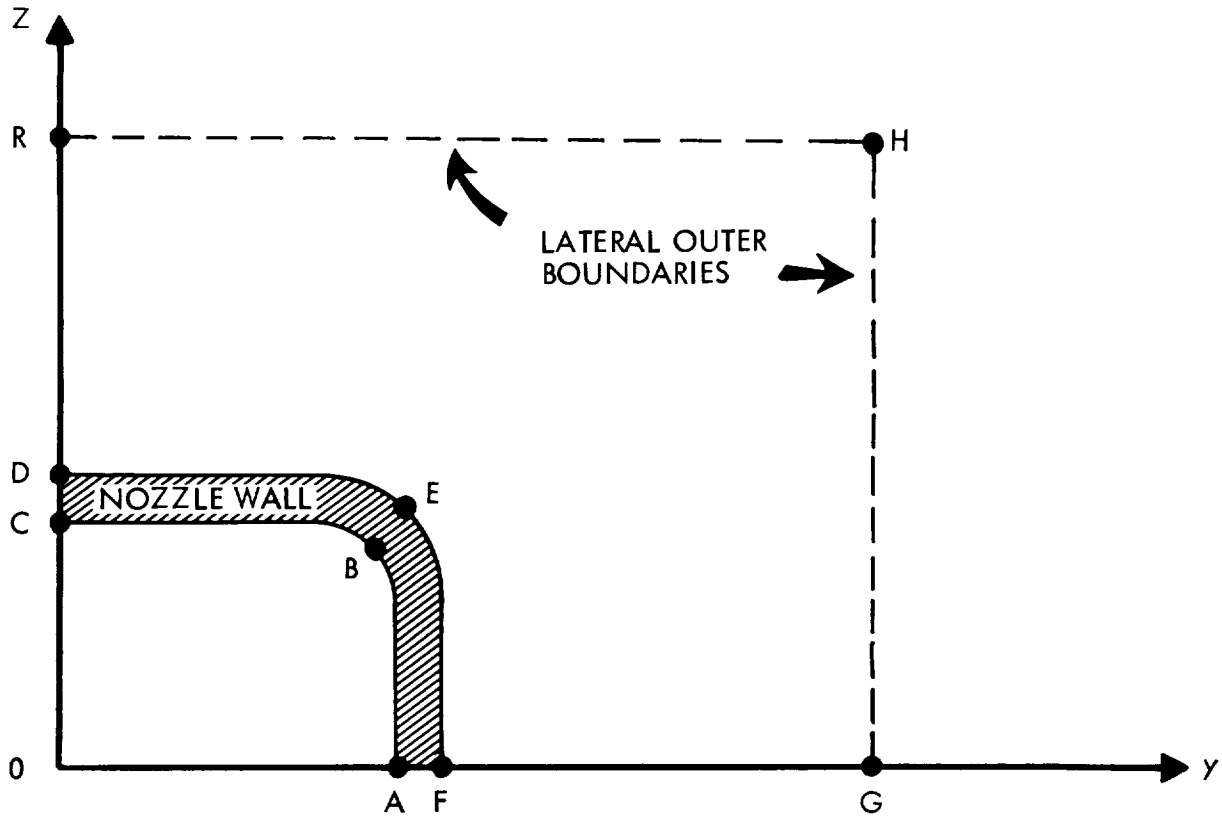

Fig. 3-1 Cross Section of Physical Flow Region for Super-Elliptical Nozzle

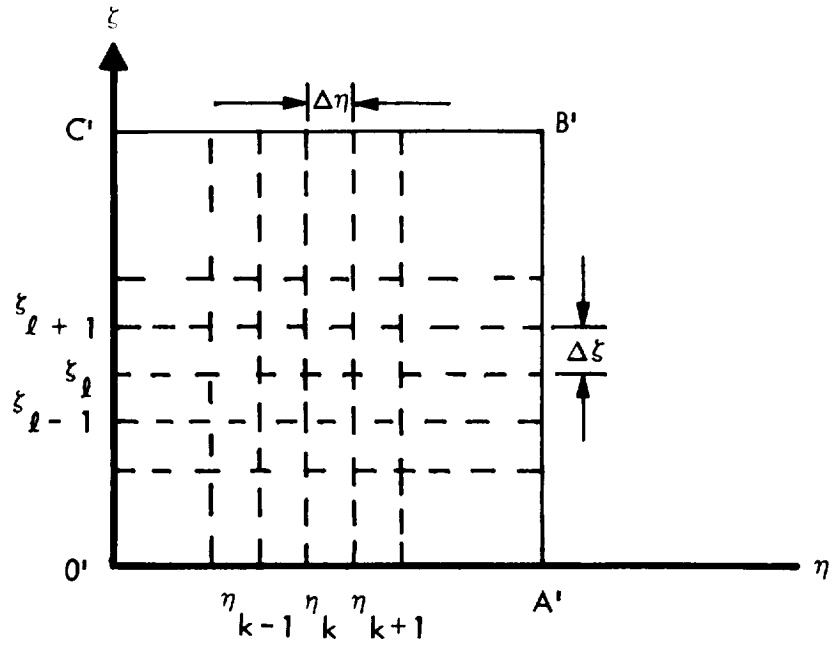

Fig. 3-2 Rectangular Computational Domain for the Nozzle Interior

and

$$\alpha = y_\zeta^2 + z_\zeta^2$$

$$\beta = y_\eta\, y_\zeta + z_\eta\, z_\zeta$$

$$\gamma = y_\eta^2 + z_\eta^2 \tag{3.3}$$

where J denotes the Jacobian of the transformation

$$J = \frac{\partial (y, z)}{\partial (\eta, \zeta)} = y_\eta\, z_\zeta - y_\zeta\, z_\eta \tag{3.4}$$

Equations (3.3) are solved numerically on a uniform, rectangular grid $\Delta\eta$, $\Delta\zeta$. For a simply connected physical domain such as the nozzle interior, Dirichlet boundary conditions may be specified over the entire closed boundary O' A' B' C' O' of the computational domain. The boundary values are the (y,z) coordinates of the physical grid points that correspond to each of the mesh points (η_k , ζ_ℓ) on the boundary of the rectangular computational domain.

The physical grid points may be spaced as desired along the boundaries of the flow region. However, the major shortcoming of the TTM method is that, in practice, it is difficult to control the spacing between grid points in the interior of the flow region. The interior grid spacing is governed primarily by the elliptic system (3.3) itself. The boundary values have a strong influence on the grid spacing only in the immediate neighborhood of the boundaries, despite the strongly elliptic character of Eqs. (3.3). It is especially important to have good control over the interior grid spacing in the high Reynolds number flows of present interest, where adequate resolution of the steep velocity gradients within wall boundary layers and free shear layers demands a locally refined grid.

Various forms of the source terms P, Q in Eqs. (3.3) have been devised that contain adjustable parameters and that provide some measure of control over the interior grid spacing. This ad hoc approach has been used with success in particular applications (Refs. 10, 11, and 12), but the forms of these terms and the values of the adjustable parameters are highly problem-dependent. No generally useful method has yet been devised that can be relied upon to provide an effective means of grid control for a wide class of boundary geometries.

An example is given in Figs. 3-3 and 3-4 to illustrate the difficulty of controlling the grid in the nozzle interior. Figure 3-3 displays a quasi-elliptical grid generated by the TTM method by using simple Laplace equations ($P = Q = 0$). The parameters of the super-ellipse arc CD are $N = 1.55$, $b/a = 1.4$. The quasi-elliptical shape of the grid was achieved by specifying the boundary values so that the regular point B on the lower boundary AC of the physical domain maps onto the lower right-hand corner point of the rectangular computational domain of Fig. 3-2. The point B plays a role akin to that of the focus in the classical system of orthogonal elliptical coordinates. Equally spaced boundary values (y, z) were specified along each of the boundary segments AB, BC, CD, and DA. The resulting grid is smooth and regular in the interior, and would be suitable for inviscid flow computations. However, this grid would be incapable of resolving the nozzle wall boundary layer in a viscous flow. In an attempt to obtain a locally refined grid near the nozzle wall, an exponential distribution of boundary values was specified along the boundary segments AB and OC. The resulting grid, displayed in Fig. 3-4, is wholly unsatisfactory. Evidently, the influence of the boundary values does not penetrate very deeply into the interior, in spite of the elliptic character of Eqs. (3.3). The interior grid is affected primarily by the generating equations, rather than by the boundary values.

Equally poor results are obtained whenever highly stretched boundary values are used with $P = Q = 0$. A further example for a quasi-rectangular mapping of a high-degree super-ellipse ($N = 10$) is displayed in Fig. 3-5.

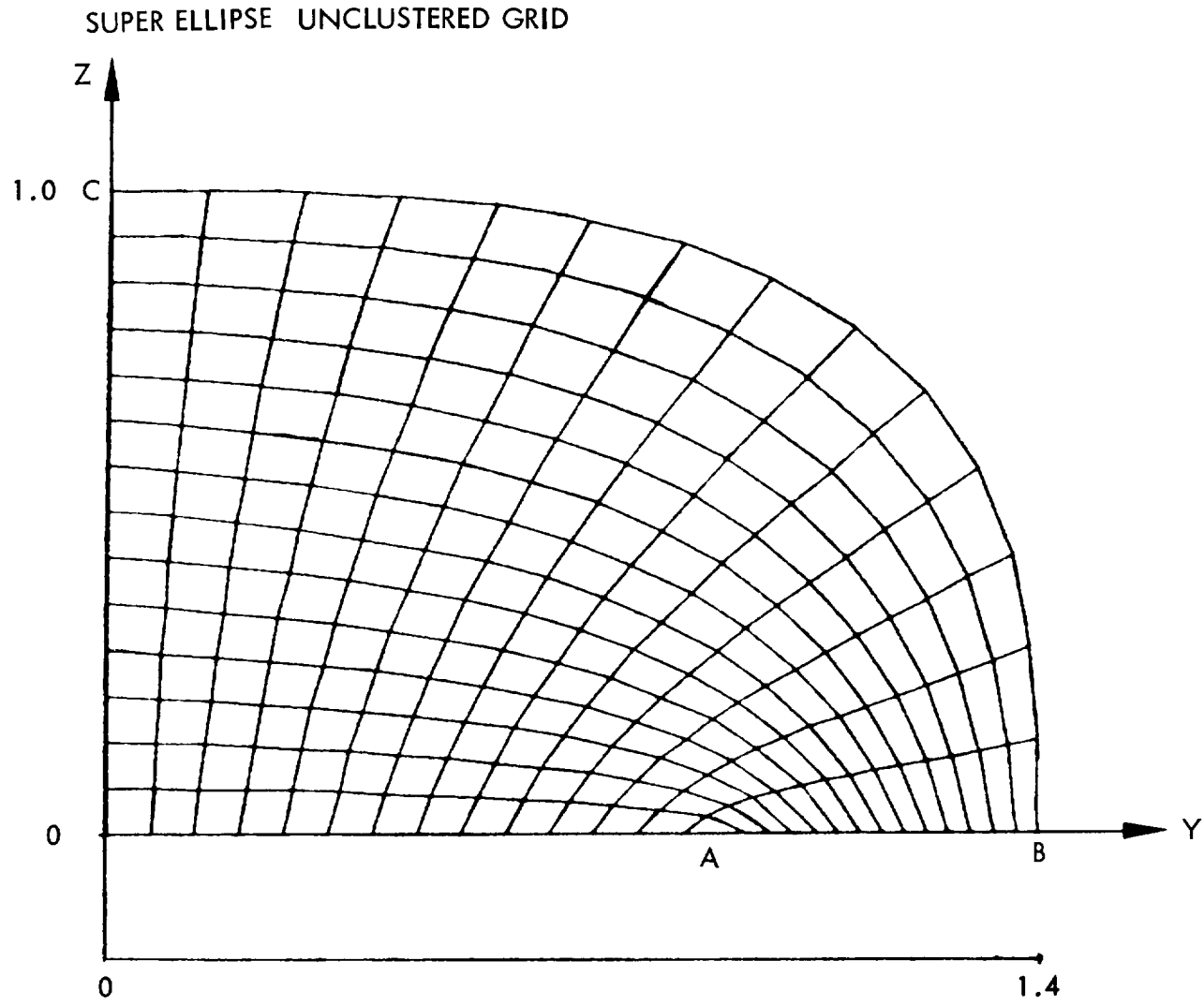

Fig. 3-3 Quasi-Elliptical Interior Grid Generated by Equally Spaced Boundary Values and P = Q = 0. N = 1.55, b/a = 1.4

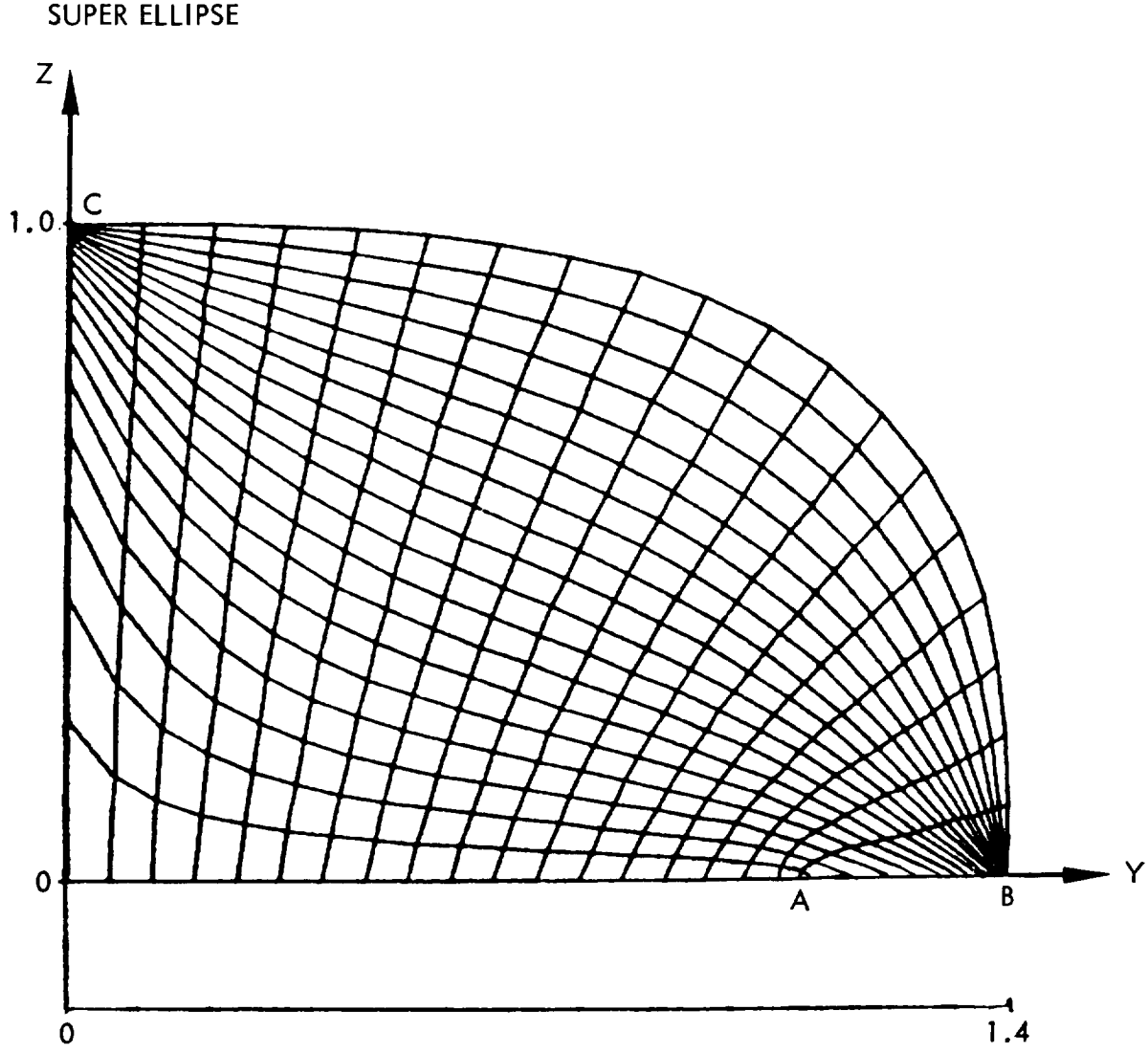

Fig. 3-4 Quasi-Elliptical Grid Generated by Exponentially Spaced Boundary Values on Segments AB, OC With P = Q = 0

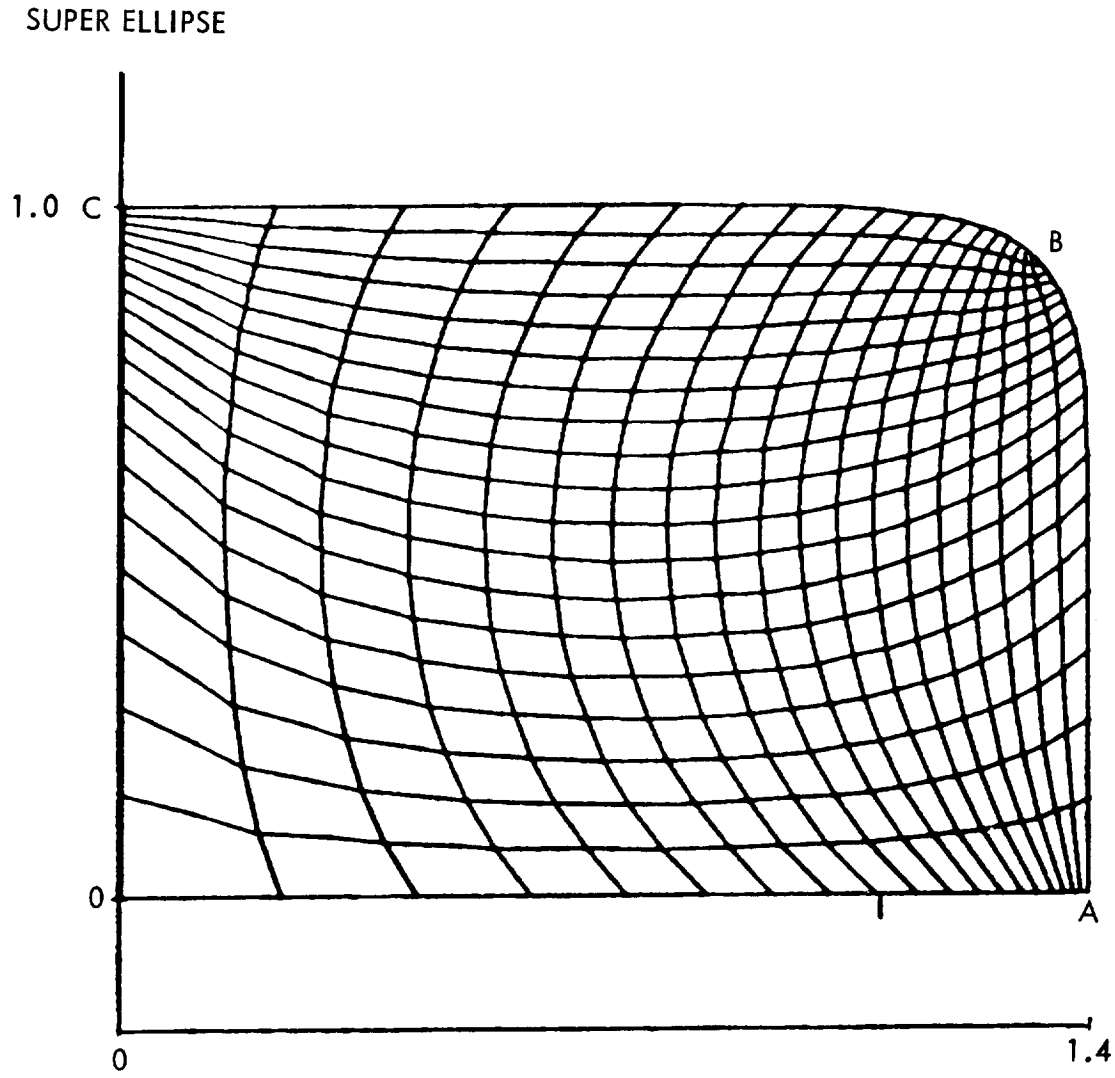

Fig. 3-5 Quasi-Rectangular Grid Generated by Exponentially Spaced Boundary Values and P = Q = 0. N = 10, b/a = 1.4

The described shortcoming of the TTM method has been overcome by devising general source terms P and Q that are computed from the Dirichlet boundary values, and that vary continuously throughout the computational domain. This results in an elliptic generating system whose solutions have the remarkable property that the grid point distribution in the interior of the physical flow region is controlled entirely by the user's selection of the grid point distribution along the boundaries. This is accomplished by choosing source terms such that Eqs. (3.3) possess exponential solutions, although the terms themselves are not exponentials functions. The terms contain arbitrary parameters that are evaluated locally at the boundaries of the computational domain by using a finite-difference representation of the limiting form of the system (3.3) that is valid at the boundaries. Interpolation of these parameters into the interior from the boundaries then defines the parameters at each mesh point of the computational domain. Numerical solution of Eqs. (3.3) by standard successive line over-relaxation (SLOR) then results in a grid throughout the physical domain that is controlled entirely by the selection of grid points on the boundaries of that domain.

The source terms have the form

$$P = \varphi(\eta, \xi)(\eta_y^2 + \eta_z^2)$$

$$Q = \psi(\eta, \xi)(\xi_y^2 + \xi_z^2) \tag{3.5}$$

where the parameters φ, ψ are yet to be specified. Upon introducing these terms, Eq. (3.3) assume the form

$$\alpha(y_{\eta\eta} + \varphi y_\eta) - 2\beta y_{\eta\xi} + \gamma(y_{\xi\xi} + \psi y_\xi) = 0$$

$$\alpha(z_{\eta\eta} + \varphi z_\eta) - 2\beta z_{\eta\xi} + \gamma(z_{\xi\xi} + \psi z_\xi) = 0 \tag{3.6}$$

One can verify easily that Eqs. (3.6) possess exponential solutions if the parameters φ, ψ are locally constant. Given a set of boundary values (y, z) on the boundary of the computational domain, one can determine the parameters by requiring that the given boundary values satisfy appropriate limiting forms of Eqs. (3.6) along the boundary of the computational domain. For example, along either of the vertical boundaries η - const. in Fig. 3-2, the limiting form of Eqs. (3.6) is

$$\text{Along } \eta = \text{const.} \begin{cases} y_{\xi\xi} + \psi y_{\xi} = 0 & (3.7a) \\ z_{\xi\xi} + \psi z_{\xi} = 0 & (3.7b) \end{cases}$$

Similarly, the limiting form for horizontal boundaries ξ = const. is

$$\text{Along } \xi = \text{const.} \begin{cases} y_{\eta\eta} + \varphi y_{\eta} = 0 & (3.8a) \\ z_{\eta\eta} + \varphi z_{\eta} = 0 & (3.8b) \end{cases}$$

For the quasi-rectangular mapping of the nozzle interior shown in Fig. 3-1 onto the computational domain shown in Fig. 3-2, a finite-difference representation of Eq. (3.7b) can be used to compute the parameter ψ locally at each mesh point along the vertical boundaries η = const.

$$\psi(\eta, \xi) = - z_{\xi\xi}/z_{\xi} \qquad (3.9a)$$

$$(z_{\xi})_{k,\ell} = (z_{k,\ell+1} - z_{k,\ell-1})/2\Delta\xi \qquad (3.9b)$$

$$(z_{\xi\xi})_{k,\ell} = (z_{k,\ell+1} - 2z_{k,\ell} + z_{k,\ell-1})/\Delta\xi^2 \qquad (3.9c)$$

The parameter $\phi(\eta, \xi)$ is evaluated similarly from Eq. (3.8b).

For more complicated mappings one or the other of Eqs. (3.7) may lead to an indeterminate equation for ψ. For example, the quasi-elliptical mapping shown in Fig. 3-3 is such that Eq. (3.7b) is indeterminate along the right-hand vertical boundary of the computational domain of Fig. 3-2, and Eq. (3.7a) must be used in place of (3.7b) to evaluate ψ. For an arbitrary nonsingular mapping, one can show that one or the other of Eqs. (3.7) is always determinate at each point of the boundary, and defines a unique value of the parameter ψ at that point. This follows from the fact that, along the boundary, y and z are related by the equation $f(y,z) = 0$ that describes the geometric shape of the boundary curve in the physical domain. Thus, in principle, either of Eqs. (3.7) can be used to compute the parameter ψ. In practice, the best results are obtained by employing Eq. (3.7a) locally at points where $y_\zeta \geq z_\zeta$, and Eq. (3.7b) locally at points where $y_\zeta < z_\zeta$. A similar statement holds for the parameter φ in Eqs. (3.8).

Once the parameter ψ is defined at each mesh point of the vertical boundaries η = const. in the computational domain, its value at interior mesh points can be computed by linear interpolation along horizontal mesh lines ζ = const. Similarly, φ is computed by interpolation between the boundaries ζ = const. at which it is defined by Eqs. (3.8). Equations (3.6) then are solved by SLOR iteration in the computational domain to generate the grid in the physical domain.

Figure 3-6 shows the physical grid generated by the described technique for the interior and exterior flow regions of the super-elliptical nozzle geometry illustrated in Fig. 3-1. The grid, highly refined near the nozzle walls to resolve the wall boundary layers, was generated simply by inputting an exponential grid point distribution along each boundary of the computational domain illustrated in Fig. 3-7b. Observe the smooth, regular character of the grid, the near-orthogonality of the grid lines to the nozzle wall, and the nearly uniform spacing between the wall and nearest wall-like grid line over the whole length of the wall.

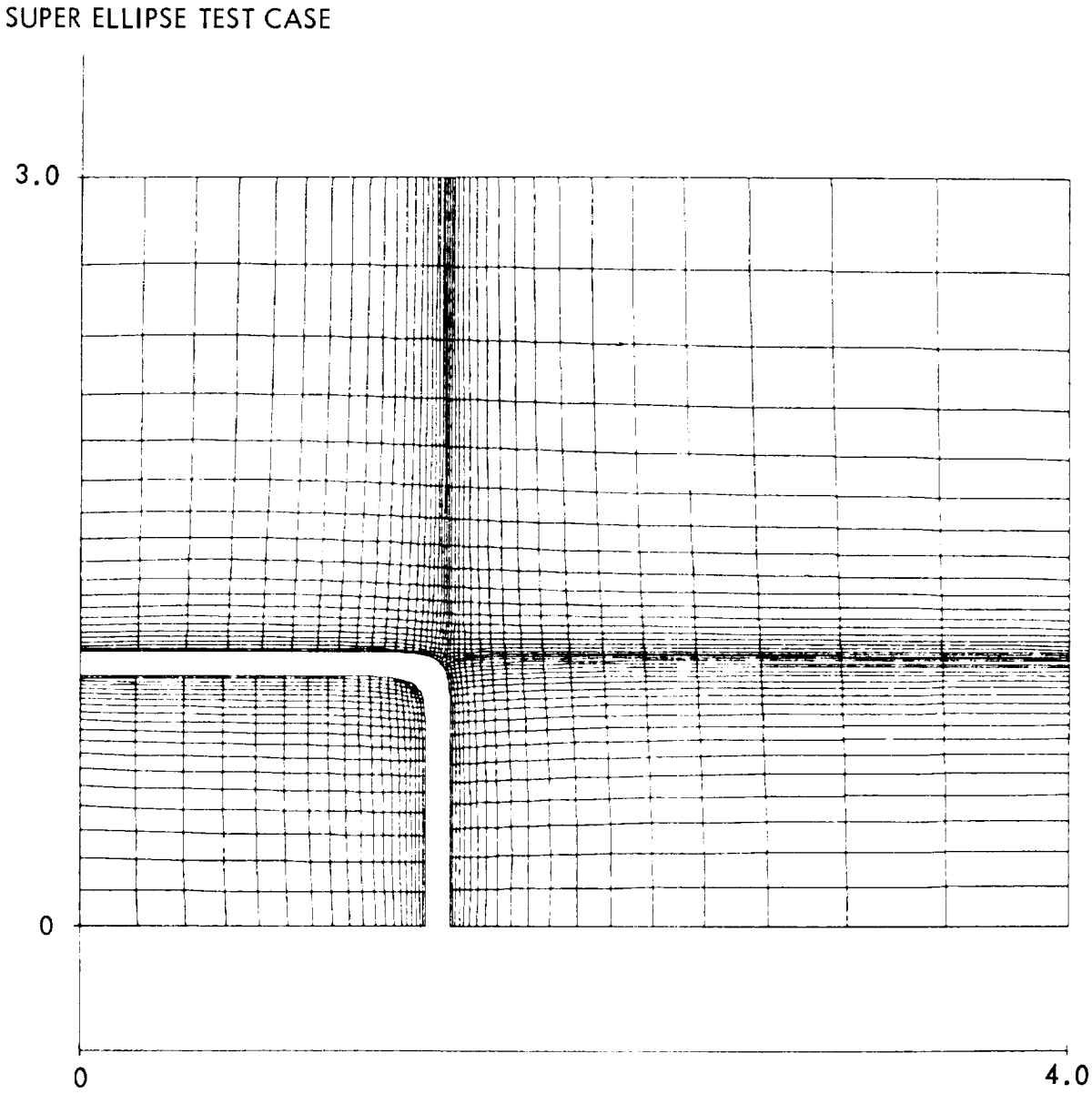

Fig. 3-6a Cross Section of Grid for Interior and Exterior Flow Regions of a Super-Elliptical Nozzle

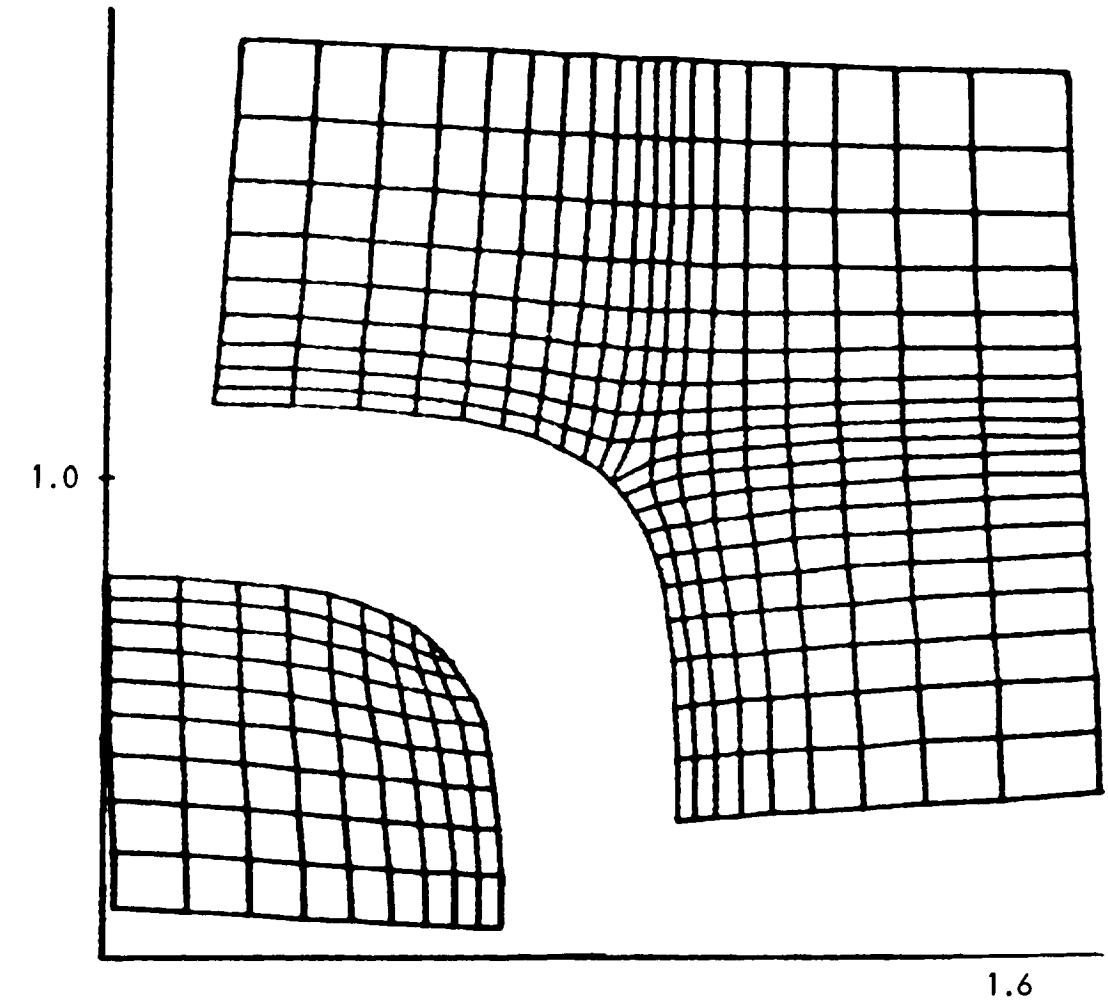

Fig. 3-6b Magnified View of Grid Near Corner of Nozzle

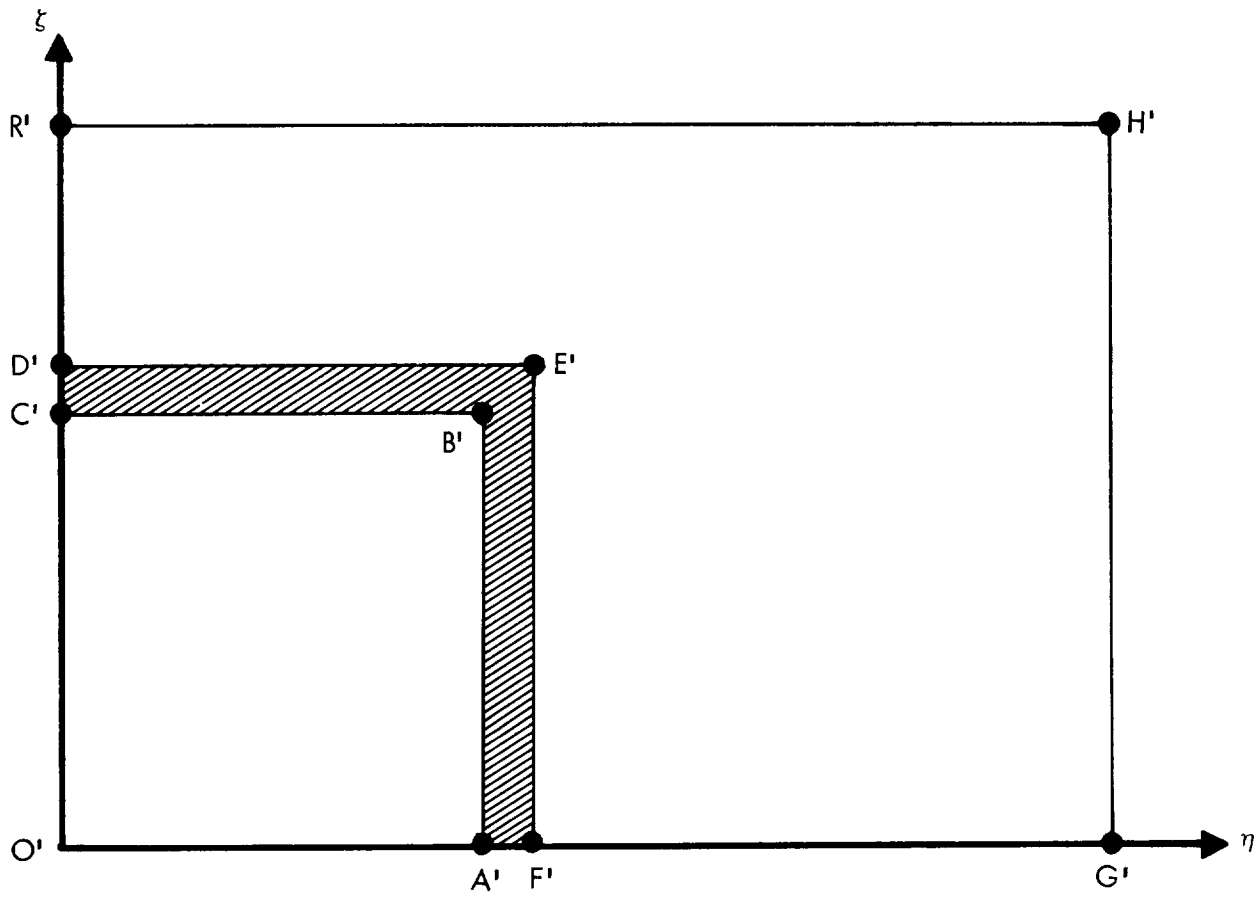

Fig. 3-7 Computational Domain Corresponding to Figs. 3-1 and 3-6a

Although the grid illustrated in Fig. 3-6 was generated using an exponential distribution of grid points along the physical boundaries of the flow region, the present technique is valid in general for any arbitrary boundary point distribution. In essence, the numerical evaluation of the parameters φ, ψ at the boundaries simply is a convenient way to construct a curve-fit to the boundary values with local embedded exponential functions. The interpolation of these parameters into the interior of the computational domain simply extends the range of the curve-fit parameters into the interior. The elliptic equation system then merely provides a reliable, automatic means for translating the parameters into a local exponential curve-fit at each interior point that reflects the boundary value distribution, and that has the properties of regularity and montonicity required of non-singular coordinate transformations.

For an arbitrarily selected cross-sectional plane $x = \text{const.}$, the described procedure automatically generates a boundary-conforming curvilinear coordinate transformation T [Eq. (2.8)] that maps the flow region bounded between the symmetry planes and the lateral outer boundaries onto a rectangle $0 \leq \eta \leq \eta_{max}$, $0 \leq \zeta \leq \zeta_{max}$. The latter then is subdivided into a rectangular grid of uniform spacing $\Delta\eta$, $\Delta\zeta$. The coordinates of the grid points are then

$$\eta_k = (k - 1)\,\Delta\eta \qquad 1 \leq k \leq K \tag{3.9a}$$

$$\zeta_\ell = (\ell - 1)\,\Delta\zeta \qquad 1 \leq \ell \leq L \tag{3.9b}$$

Repetition of the procedure for a sequence of cross-sectional planes x_j defines a three-dimensional transformation that maps the entire nozzle flow region of Fig. 1-1 onto a rectangular solid $0 \leq \xi \leq \xi_{max}$, $0 \leq \eta \leq \eta_{max}$, $0 \leq \zeta \leq \zeta_{max}$. A uniform grid spacing $\Delta\xi$ then completes the definition of the computational space

$$\xi_j = (j - 1)\,\Delta\xi \qquad 1 \leq j \leq J \tag{3.9c}$$

Without loss of generality, we may choose

$$\Delta\xi = \Delta\eta = \Delta\zeta = 1 \tag{3.10}$$

so that the triplet of indices (j, k, ℓ) describes uniquely the coordinates of each grid point in the computational space. For general mappings, each computational grid point has an image point $(x_{j,k,\ell}, y_{j,k,\ell}, z_{j,k,\ell})$ in the physical space illustrated in Fig. 1-1. However, note that the mapping used here employs cross-sectional planes. Consequently, the x-coordinate of a grid point depends only on the index j. Furthermore, we shall assume that the physical grid is stationary; i.e., that the mapping functions (2.8) are independent of time t. Time-dependent mappings are useful in problems that involve free boundaries such as external shock waves (see Ref. 6), but are unnecessary in the present application.

The coordinates x_j define the physical location of the cross-sectional planes, and may be selected arbitrarily. In each such plane j, the coordinates $y_{j,k,\ell}$ and $z_{j,k,\ell}$ of the grid points in physical space are computed numerically from the elliptic system (3.3). The manner in which these numerically-generated coordinate transformations are used in flowfield computations is explained in Section 4, which presents the difference equations derived from the flow equations that have been summarized in Section 2.

Section 4

IMPLICIT DIFFERENCE EQUATIONS AND SOLUTION TECHNIQUE

The Navier-Stokes equations (2.20) are to be solved numerically in the computational space defined in Section 3, subject to the boundary conditions given by Eqs. (2.21) through (2.31). We shall employ an implicit numerical method to avoid the severely limited time stepsize that would be imposed by the numerical stability bound of an explicit method. For the latter type of method, one can show that the maximum stable time step allowed by an explicit scheme is proportional to the smallest distance between any two grid points in physical space, whenever that grid spacing is sufficiently fine to resolve accurately the thin viscous wall boundary layers and free shear layers in the nozzle flowfield. The resultingly great number of time steps needed to attain convergence to the desired steady-state solution easily can lead to impractically long computer runtime. Properly formulated implicit methods are free of such severe numerical stability criteria.

The numerical methods developed by Beam and Warming (Ref. 13) and by Briley and MacDonald (Ref. 14) basically are similar in their use of implicit time-differencing and of alternating direction techniques (spatial operator factorization) for the multi-dimensional Navier-Stokes equations. Beam and Warming first applied the method to the conservation-law form of the full Navier-Stokes equations for two-dimensional laminar flow in Cartesian coordinates. The method was combined with the general mapping in Eq. (2.8) by Steger (Ref. 3) for two-dimensional plane flow; by Kutler, et al. (Ref. 15) for axisymmetric flow; and by Pulliam and Steger (Ref. 7); and by Thomas and Lombard (Ref. 6) for three-dimensional flow. However, the latter four references employed the "thin-layer" approximation to the Navier-Stokes equations in which the viscous terms associated with only one of the three coordinate directions are retained. The thin layer approximation is obtained by dropping the first three terms from the R.H.S. of Eq. (2.20). We shall apply the Beam-Warming method to Eq. (2.20) itself. We derive first the difference equations for interior grid points. The boundary conditions require special treatment, and will be dealt with later in Section 4.2.

4.1 INTERIOR GRID POINTS

In Ref. 13, Beam and Warming approximated the spatial derivative terms in the Navier-Stokes equations by standard second-order accurate central difference operators, and employed general implicit time-differencing of either first- or second-order accuracy, depending upon the choice of a parameter. We shall employ the first-order accurate Euler-implicit time-differencing, since we seek only the asymptotic steady-state solution. The accuracy of the steady-state numerical solution is governed by the spatial difference operators (Ref. 13).

4.1.1 Time Differencing

The first-order accurate implicit time-differenced form of Eq. (2.20) is

$$\frac{\Delta\hat{q}}{\Delta\tau} + \left(\frac{\partial\hat{f}}{\partial\xi} + \frac{\partial\hat{g}}{\partial\eta} + \frac{\partial\hat{h}}{\partial\zeta}\right)^{n+1} = R_e^{-1}\left\{\left[\frac{\partial}{\partial\eta}\,\hat{\theta}(\eta) + \frac{\partial}{\partial\zeta}\,\hat{\omega}(\zeta)\right]^{n+1} + \left[\frac{\partial}{\partial\eta}\,\hat{\theta}(\zeta) + \frac{\partial}{\partial\xi}\,\hat{\omega}(\eta)\right]^{n}\right\} \quad (4.1)$$

where the superscript n denotes the time level, Δ is the classical forward time difference operator

$$\begin{aligned} \Delta\hat{q} &= \hat{q}^{n+1} - \hat{q}^{n} \\ \Delta\tau &= \tau^{n+1} - \tau^{n} \end{aligned} \quad (4.2)$$

and, for later convenience, we have switched from the subscript notation to the standard partial differential operator notation for spatial derivatives.

Note that the viscous cross-derivative terms—the terms in the second set of brackets in Eq. (4.1)—are evaluated explicitly at time τ^n, whereas all other terms are evaluated implicitly at the advanced time $\tau^{n+1} = \tau^n + \Delta\tau$ (Ref. 13). As shown in the latter reference, this treatment of the cross-derivative terms does not compromise the stability of the numerical method. The remaining terms are locally linearized in time by using local Taylor series expansions. For the inviscid flux vectors $\hat{f}$ and $\hat{g}$, the linearization is

$$\hat{f}^{n+1} = \hat{f}^{n} + F^{n}\Delta\hat{q} + \cdots$$

$$\hat{g}^{n+1} = \hat{g}^{n} + G^{n}\Delta\hat{q} + \cdots \qquad (4.3)$$

$$\hat{h}^{n+1} = \hat{h}^{n} + H^{n}\Delta\hat{q} + \cdots$$

where $F, G, H,$ are the Jacobian matrices

$$F = \partial\hat{f}/\partial\hat{q} \qquad G = \partial\hat{g}/\partial\hat{q} \qquad H = \partial\hat{h}/\partial\hat{q} \qquad (4.4a)$$

It follows from Eqs. (2.9) that the Jacobian F is given by

$$F = \xi_t I + \xi_x F' + \xi_y G' + \xi_z H' \qquad (4.4b)$$

$$F' = \partial\vec{f}/\partial\vec{q} \qquad G' = \partial\vec{g}/\partial\vec{q} \qquad H' = \partial\vec{h}/\partial\vec{q} \qquad (4.4c)$$

$$I = \text{Identity matrix} \qquad (4.4d)$$

The corresponding expressions that define matrices G and H can be obtained from (4.4b) by the substitutions $\xi \rightarrow \eta$ and $\xi \rightarrow \zeta$, respectively.

The Taylor series expansions given in Eq. (4.3) are valid only if the coordinate transformation (2.8) is independent of time

$$\hat{\xi}_t = \hat{\eta}_t = \hat{\zeta}_t = 0 \qquad (4.4e)$$

This implies that the grid is stationary in physical space (x, y, z). The reader is referred to Ref. 6, where the general case is treated for moving grids associated with time-dependent coordinate transformations.

The viscous terms are linearized similarly as follows:

$$\left[\hat{\theta}(\eta)\right]^{n+1} = \left[\hat{\theta}(\eta)\right]^{n} + R^{n}\Delta\hat{q} + \cdots \tag{4.5a}$$

$$\left[\hat{\omega}(\zeta)\right]^{n+1} = \left[\hat{\omega}(\zeta)\right]^{n} + S^{n}\Delta\hat{q} + \cdots \tag{4.5b}$$

where R, S are matrices whose elements are differential operators. The notation such as $R\Delta\hat{q}$ thus is to be interpreted not as the product of a matrix R and a vector $\Delta\hat{q}$, but rather as a matrix operator that operates on the vector $\Delta\hat{q}$. The expressions that define the operators R, S are derived in Appendix A.

The expansions (4.3) and (4.5) allow Eq. (4.1) to be written in the operational form

$$\left\{I + \Delta\tau\left[\frac{\partial}{\partial\xi}F + \frac{\partial}{\partial\eta}\left(G - Re^{-1}R\right) + \frac{\partial}{\partial\zeta}\left(H - Re^{-1}S\right)\right]\right\}^{n}\Delta\hat{q} = \hat{r}^{n} \tag{4.6}$$

where the linear operator notation is to be interpreted as follows:

$$\left(\frac{\partial}{\partial\xi}F\right)^{n}\Delta\hat{q} \equiv \frac{\partial}{\partial\xi}\left(F^{n}\Delta\hat{q}\right) \tag{4.7}$$

That is, the spatial differential operator acts upon the product $F^{n}\Delta\hat{q}$ and not upon the matrix F^{n} itself [cf. Eqs. (4.5) and (A.6), and Ref. 13]. The R.H.S. of Eq. (4.6) consists of the spatially differentiated terms in Eq. (4.1), evaluated at time level n

$$\hat{r}^{n} = -\Delta\tau\left\{\frac{\partial f}{\partial\xi} + \frac{\partial}{\partial\eta}\left[\hat{g} - Re^{-1}\hat{\theta}(\zeta)\right] + \frac{\partial}{\partial\zeta}\left[\hat{h} - Re^{-1}\hat{\omega}(\eta)\right] - Re^{-1}\left[\frac{\partial}{\partial\eta}\hat{\theta}(\eta) + \frac{\partial}{\partial\zeta}\hat{\omega}(\zeta)\right]\right\}^{n} \tag{4.8}$$

The various terms in Eq. (4.8) are grouped in a fashion that is convenient for the spatial differencing to be performed later.

The final form of the time-differencing algorithm is obtained by noting that the spatially three-dimensional operator on the L.H.S. of (4.6) can be factored into a product of one-dimensional operators, with a remainder term that is of the same order as the temporal truncation error of (4.6) itself (Ref. 13). The factored operator equation is

$$\left\{\left[I + \Delta\tau \frac{\partial}{\partial\xi} F\right]\left[I + \Delta\tau \frac{\partial}{\partial\eta}\left(G - Re^{-1}R\right)\right]\right.$$
$$\left.\left[I + \Delta\tau \frac{\partial}{\partial\zeta}\left(H - Re^{-1}S\right)\right]\right\}^n \Delta\hat{q} = \hat{r}^n \qquad (4.9)$$

Although the three operators are not commutative, the truncation error is of second order in $\Delta\tau$ for any arrangement of the three factors.

Once the spatial derivative operators are replaced by finite-difference operators, the solution vector $\hat{q}^{n+1}$ is obtained through the ADI (Alternating Direction Implicit) sequence

$$\left[I + \Delta\tau \frac{\partial}{\partial\xi} F\right]^n \Delta\hat{q}^{**} = \hat{r}^n$$

$$\left[I + \Delta\tau\left(\frac{\partial}{\partial\eta} G - Re^{-1}\frac{\partial}{\partial\eta} R\right)\right]^n \Delta\hat{q}^{*} = \Delta\hat{q}^{**} \qquad (4.10)$$

$$\left[I + \Delta\tau\left(\frac{\partial}{\partial\zeta} H - Re^{-1}\frac{\partial}{\partial\zeta} S\right)\right]^n \Delta\hat{q} = \Delta\hat{q}^{*}$$

$$\hat{q}^{n+1} = \hat{q}^n + \Delta\hat{q}$$

where the operators in parentheses in the second and third factors of Eq. (4.9) have been rearranged in a form more convenient for spatial differencing.

4.1.2 Spatial Differencing

The spatial differencing of Eqs. (4.10) can be represented conveniently in terms of classical difference operators. We shall employ the half-mesh shift operator $E^{1/2}$ and two central operators: the averaging operator $\mu = \left(E^{1/2} + E^{-1/2}\right)/2$, and the central difference operator $\delta = E^{1/2} - E^{-1/2}$. For a mesh function f defined at mesh points j, the operators are defined as follows (Ref. 16):

$$E^{\pm 1/2} f_j = f_{j \pm 1/2} \tag{4.11a}$$

$$\mu f_j = \left(f_{j+1/2} + f_{j-1/2}\right)/2 \tag{4.11b}$$

$$\delta f_j = f_{j+1/2} - f_{j-1/2} \tag{4.11c}$$

However, we must deal with three-dimensional mesh functions such as f_{jkl}. To avoid confusion about the spatial direction in which a given operator acts, we shall append a subscript to indicate that direction. For example, we have

$$\mu_k f_{jkl} = \left(f_{j,k+1/2,l} + f_{j,k-1/2,l}\right)/2 \tag{4.12}$$

The single subscript also will serve to distinguish between the averaging operator and the viscosity coefficient, both of which are represented by the symbol μ.

We consider first the spatial differencing of the term $\hat{r}^n$ in the first of Eqs. (4.10) as defined in Eq. (4.8). The superscript n indicating the time level will be suppressed for brevity. The first-order spatial derivative operator $\partial/\partial\xi$ of the first term in braces in Eq. (4.8) is represented as follows by a central difference formula that is accurate to second order in the spatial grid spacing $\Delta\xi$.

$$\frac{\partial \hat{f}}{\partial \xi} \sim \left(\mu_j \delta_j \hat{f}_{jkl}\right)/\Delta\xi \equiv \left(\hat{f}_{j+1,k,l} - \hat{f}_{j-1,k,l}\right)/2\Delta\xi \tag{4.13a}$$

$$\Delta\xi = 1$$

The increment $\Delta\xi$ will be omitted from this and from subsequent spatial difference formulas by virtue of Eq. (3.10). The derivative operators $\partial/\partial\eta$, $\partial/\partial\zeta$ of the second and third terms in braces in Eq. (4.8) are represented by the corresponding central difference operators

$$\frac{\partial}{\partial\eta}\left[\hat{g} - Re^{-1}\,\hat{\theta}^{(\zeta)}\right] \sim \mu_k\,\delta_k\left[\hat{g} - Re^{-1}\,\hat{\theta}^{(\zeta)}\right]_{jkl} \tag{4.13b}$$

$$\frac{\partial}{\partial\zeta}\left[\hat{h} - Re^{-1}\,\hat{\omega}^{(\eta)}\right] \sim \mu_l\,\delta_l\left[\hat{h} - Re^{-1}\,\hat{\omega}^{(\eta)}\right]_{jkl} \tag{4.13c}$$

The same difference operators are used to represent the derivatives that enter into the vectors $\hat{\theta}^{(\zeta)}$ and $\hat{\omega}^{(\eta)}$. For example, the first term in the second component of the vector $\hat{\theta}^{(\zeta)}$ is [Eq. (2.16c)].

$$\mu J\,(\nabla\eta\cdot\nabla\zeta)\,U_\zeta \sim \left[\mu J\,(\eta_x\zeta_x + \eta_y\zeta_y + \eta_z\zeta_z\right]_{jkl}\mu_l\delta_l U_{jkl} \tag{4.13d}$$

One sees from Eq. (2.16b) that the first term enclosed by the last set of brackets in Eq. (4.8) involves repeated derivatives with respect to η. Both the outer derivative $\partial/\partial\eta$ of the term in question and the inner derivatives that enter into $\hat{\theta}^{(\eta)}$ in Eq. (2.16b) are represented by the central difference operator δ_k

$$\frac{\partial}{\partial\eta} \sim \delta_k \tag{4.14a}$$

Thus, quantities such as $\partial/\partial\eta\,(\mu J\,|\nabla\eta|^2\,\partial U/\partial\eta)$ that appear when the term $\partial\hat{\theta}^{(\eta)}/\partial\eta$ is written in expanded form are differenced as follows:

$$\frac{\partial}{\partial\eta}\left(\mu J\,|\nabla\eta|^2\,\frac{\partial U}{\partial\eta}\right) \sim \delta_k\left(\mu J\,|\nabla\eta|^2\,\delta_k U\right) \tag{4.14b}$$

The last term in Eq. (4.8) is differenced similarly in terms of the operator δ_l

$$\frac{\partial}{\partial\zeta} \sim \delta_l \tag{4.14c}$$

Each spatially differentiated term on the left of Eqs. (4.10) involves either an ordinary matrix such as F or a matrix of spatial differential operators such as R. Each such matrix is the Jacobian of one of the terms that comprise the quantity $\hat{r}$ in (4.8). For consistency, the spatial derivative operators that appear in each term on the left of (4.10) are represented by the same difference operators that are used for the corresponding term of $\hat{r}$ in (4.8). For example, in the first of Eqs. (4.10), the term involving the Jacobian of the inviscid flux vector $\hat{f}$ in Eq. (4.8) is differenced as is (4.13a).

$$\frac{\partial}{\partial \xi} F \sim \mu_j \delta_j F \tag{4.15}$$

Similarly, the terms $(\partial/\partial\eta)G$ and $(\partial/\partial\zeta)H$ are differenced as in Eqs. (4.13b) and (4.13c), respectively. Finally, Eqs. (4.14a) and (4.14c) are used for the last term in parentheses in each of the second and third of Eqs. (4.10).

When the curvilinear coordinate system and the computational grid are generated numerically as described in Section 3, the grid generation procedure yields only the x, y, z coordinates of each grid point in physical space. The "metric coefficients" $\hat{\xi}_x$, $\hat{\xi}_y$, etc. then must be computed from Eqs. (2.14). This can be accomplished by using the central difference operator $\mu\delta$ to represent the spatial derivatives. The final difference equations for interior points then take the operational form

$$\left[I + \Delta\tau \mu_j \delta_j F\right]^n \Delta\hat{q}^{**}_{jkl} = \hat{r}^n_{jkl} \tag{4.16a}$$

$$\left[I + \Delta\tau \left(\mu_k \delta_k G - Re^{-1} \delta_k R\right)\right]^n \Delta\hat{q}^{*}_{jkl} = \Delta\hat{q}^{**}_{jkl} \tag{4.16b}$$

$$\left[I + \Delta\tau \left(\mu_l \delta_l H - Re^{-1} \delta_l S\right)\right]^n \Delta\hat{q}_{jkl} = \Delta q^{*}_{jkl} \tag{4.16c}$$

$$\hat{q}^{n+1}_{jkl} = \hat{q}^n_{jkl} + \Delta\hat{q}_{jkl} \tag{4.16d}$$

where

$$\hat{r}^n_{jkl} = -\Delta\tau\left\{\mu_j \delta_j \hat{f} + \mu_k \delta_k \left[\hat{g} - Re^{-1}\hat{\theta}^{(\zeta)}\right] + \mu_l \delta_l \left[\hat{h} - Re^{-1}\hat{\omega}^{(\eta)}\right] - Re^{-1}\left[\delta_k \hat{\theta}^{(\eta)} + \delta_l \hat{\omega}^{(\zeta)}\right]\right\}^n \tag{4.17}$$

and where it is understood that the spatial derivatives involved in $\hat{\theta}^{(\zeta)}$ and $\hat{\omega}^{(\eta)}$ are differenced as described following Eq. (4.13c), and those involved in $\hat{\theta}^{(\eta)}$, $\hat{\omega}^{(\zeta)}$, R, and S are differenced according to Eq. (4.14).

Each step of the ADI sequence (4.16) involves the solution of a linear system of equations having a block-tridiagonal coefficient matrix. For example, upon applying the operator on the L.H.S. of Eq. (4.16a), we obtain

$$-\frac{\Delta\tau}{2}\left(F^n \Delta\hat{q}^{**}_{j-1}\right) + \Delta\hat{q}^{**}_j + \frac{\Delta\tau}{2}\left(F^n \Delta\hat{q}^{**}_{j+1}\right) = \hat{r}^n_j \quad , \quad 2 \le j \le J-1 \tag{4.18}$$

where the subscripts k,l have been suppressed. The block-tridiagonal structure is readily apparent, inasmuch as the Jacobian matrices $F^n_{j\pm1}$ (the blocks) are 5X5 square matrices.

However, the system of Eq. (4.18) is incomplete; it involves only J-2 equations among the J unknown values of $\Delta\hat{q}^{**}$. The missing equations are those for the boundary points j = 1, J. To close the system, Steger (Ref. 3) and Pulliam and Steger (Ref. 7) simply assume $\Delta\hat{q}^{**}_1 = \Delta\hat{q}^{**}_J = 0$; i.e., that the flow conditions at the boundaries do not change over a time step. After the sequence (4.16) is completed for interior points, they then update the values of $\vec{q}$ at the boundaries by ad hoc methods that are intended to satisfy the boundary conditions at steady state. This time-lagging approach implies only a zero-order time accuracy at the boundaries. The approach does not necessarily degrade the accuracy of the steady-state solution, depending on the updating procedures, but it may retard the rate of convergence to steady state. The numerical experiments described in Section 5 suggest that this is the case.

Rather than use the time-lagging approach, we follow the approach taken in Ref. 15, and formulate implicit difference equations for the boundary grid points that are similar to those for interior points, but that embody the boundary conditions of Section 2.4.

4.2 BOUNDARY POINTS

In this subsection, we formulate boundary point-difference equations that have the same time accuracy as the interior point equations, and that are compatible with the latter

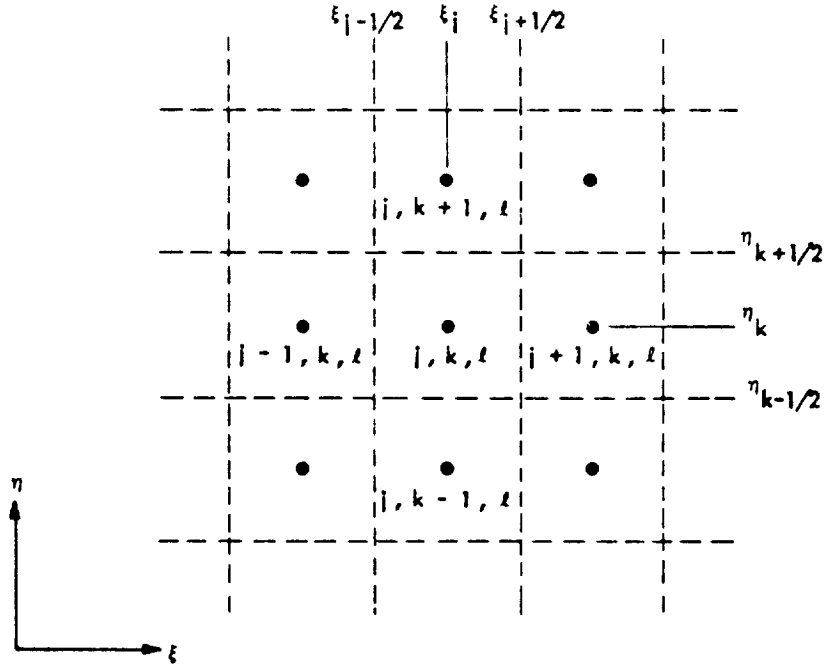

Fig. 4-1a Sketch of Computational Grid in a Plane ζ = Constant

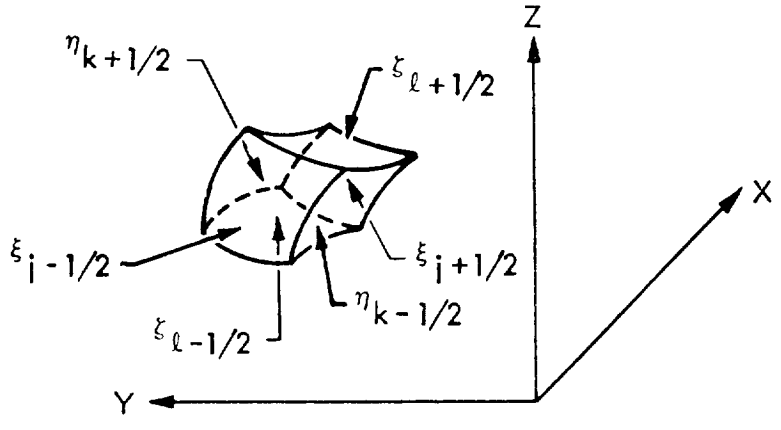

In the finite volume method, the value of $\hat{f}$ at a cell face is defined as the average of values at the two neighboring grid points

$$\hat{f}_{j+1/2,k,\ell} = (\hat{f}_{jk\ell} + \hat{f}_{j+1,k,\ell})/2 = \mu_j \hat{f}_{j+1/2,k,\ell} \tag{4.20b}$$

When the left-hand equality of (4.20b) is substituted into that of (4.20a), the resulting equation is identical to Eq. (4.13a); namely, the central difference that is obtained by applying the operators δ_j and μ_j in sequence. Similar results hold for all the spatially differentiated terms of Eq. (4.1). Furthermore, by the mean value theorem, the first term in the volume integrated version of (4.1) represents the time derivative of the cell-averaged value of $\hat{q}$, and is properly located at the cell centroid; i.e., at the grid point j, k, ℓ (Ref. 6). This geometrical interpretation simplifies the task of devising boundary-point difference operators that are consistent with the central differences employed at interior points. We consider first the outflow boundary $\xi = \xi_{max}$.

Outflow Boundary. Associated with each point of the outflow boundary is a half-cell, as illustrated in Fig. 4-2. The centroid of the half-cell is indicated by the asterisk. For the outflow boundary, the only exterior derivative in Eq. (4.1) is the first term in parentheses on the L.H.S. The natural differencing of this term that is compatible with the use of (4.20a) at the adjacent interior point is

$$\left(\frac{\partial \hat{f}}{\partial \xi}\right)_J \sim (\hat{f}_J - \hat{f}_{J-1/2})/(\Delta\xi/2) = \nabla_j \hat{f}$$

$$\Delta\xi = 1 \tag{4.21}$$

where the indicated equivalence to the backward difference operator of Eq. (4.19b) follows from Eq. (4.20b). The time derivative term in (4.1) must be applied at the centroid of the half-cell

$$\left(\frac{\partial \hat{q}}{\partial \tau}\right)_J \sim \frac{\Delta \hat{q}_*}{\Delta \tau} \tag{4.22a}$$

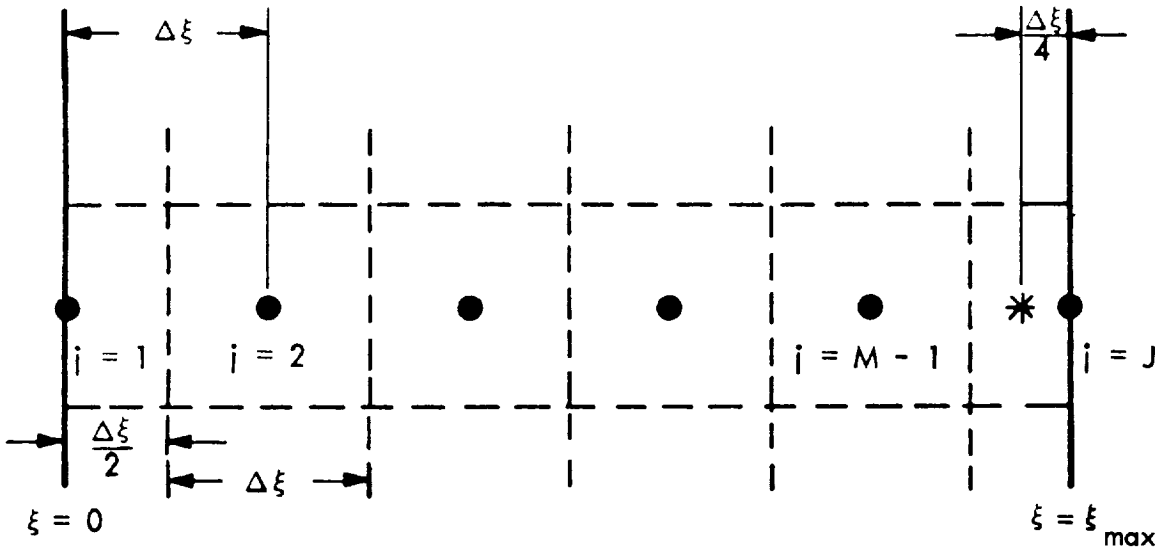

Fig. 4-2 Sketch of Interior Cells and Boundary Half-Cells Along the Coordinate ξ

where

$$\hat{r}^n_{jkl} = -\Delta\tau\left\{\mu_j \delta_j \hat{f} + \mu_k \delta_k \left[\hat{g} - Re^{-1}\hat{\theta}^{(\zeta)}\right] + \mu_l \delta_l \left[\hat{h} - Re^{-1}\hat{\omega}^{(\eta)}\right] - Re^{-1}\left[\delta_k \hat{\theta}^{(\eta)} + \delta_l \hat{\omega}^{(\zeta)}\right]\right\}^n \tag{4.17}$$

and where it is understood that the spatial derivatives involved in $\hat{\theta}^{(\zeta)}$ and $\hat{\omega}^{(\eta)}$ are differenced as described following Eq. (4.13c), and those involved in $\hat{\theta}^{(\eta)}$, $\hat{\omega}^{(\zeta)}$, R, and S are differenced according to Eq. (4.14).

Each step of the ADI sequence (4.16) involves the solution of a linear system of equations having a block-tridiagonal coefficient matrix. For example, upon applying the operator on the L.H.S. of Eq. (4.16a), we obtain

$$-\frac{\Delta\tau}{2}\left(F^n \Delta\hat{q}^{**}_{j-1}\right) + \Delta\hat{q}^{**}_j + \frac{\Delta\tau}{2}\left(F^n \Delta\hat{q}^{**}_{j+1}\right) = \hat{r}^n_j \quad , \quad 2 \le j \le J-1 \tag{4.18}$$

where the subscripts k,l have been suppressed. The block-tridiagonal structure is readily apparent, inasmuch as the Jacobian matrices $F^n_{j\pm1}$ (the blocks) are 5X5 square matrices.

However, the system of Eq. (4.18) is incomplete; it involves only J-2 equations among the J unknown values of $\Delta\hat{q}^{**}$. The missing equations are those for the boundary points j = 1, J. To close the system, Steger (Ref. 3) and Pulliam and Steger (Ref. 7) simply assume $\Delta\hat{q}^{**}_1 = \Delta\hat{q}^{**}_J = 0$; i.e., that the flow conditions at the boundaries do not change over a time step. After the sequence (4.16) is completed for interior points, they then update the values of $\vec{q}$ at the boundaries by ad hoc methods that are intended to satisfy the boundary conditions at steady state. This time-lagging approach implies only a zero-order time accuracy at the boundaries. The approach does not necessarily degrade the accuracy of the steady-state solution, depending on the updating procedures, but it may retard the rate of convergence to steady state. The numerical experiments described in Section 5 suggest that this is the case.

Rather than use the time-lagging approach, we follow the approach taken in Ref. 15, and formulate implicit difference equations for the boundary grid points that are similar to those for interior points, but that embody the boundary conditions of Section 2.4.

4.2 BOUNDARY POINTS

In this subsection, we formulate boundary point-difference equations that have the same time accuracy as the interior point equations, and that are compatible with the latter in their spatial order of accuracy. As indicated in the preceding subsection, the present treatment of boundary points differs from that in Refs. 13, 3, 6, and 7. The present treatment for Eqs. (2.20) is patterned after that presented in Ref. 15 for the complete Navier-Stokes equations (2.9), in that it provides a fully implicit set of equations for the boundary points.

4.2.1 Time Differencing

The time differencing for boundary points is the same as that for interior points, as given in Eq. (4.1). However, it is convenient to perform the spatial differencing before linearizing the equations in time (cf. subsection 4.1, where the time linearization is performed first). With this approach, the boundary conditions enter naturally into the difference equations, and the formulation of the implicit operator matrices for the viscous terms is effected more easily.

4.2.2 Spatial Differencing

In addition to the central operators given in Eq. (4.11), we shall employ the classical forward difference operator Δ, and the backward difference operator ∇. For a mesh function f_{jkl}, the operators for the j direction are defined as follows

$$\Delta_j f_{jk\ell} = (f_{j+1} - f_j)_{k\ell} \tag{4.19a}$$

$$\nabla_j f_{jk\ell} = (f_j - f_{j-1})_{k\ell} \tag{4.19b}$$

The corresponding operators for the k and ℓ directions are identified by the latter indices as subscripts. The subscripts will serve to distinguish the backward difference operator from the vector gradient operator (Section 2), both of which are identified by the symbol ∇; and to distinguish the forward spatial operator from the time operator of Eqs. (4.2).

When Eq. (4.1) is applied at a point on the boundary of the computational space ξ, η, ζ, the spatial derivatives in that equation fall into two classes: interior derivatives taken in directions that lie in the boundary surface itself, and one-sided exterior derivatives taken in the direction normal to the boundary. For example, at the inflow boundary $\xi = 0$ and the outflow boundary $\xi = \xi_{max}$, the derivatives $\partial/\partial\eta$ and $\partial/\partial\zeta$ are interior derivatives along the boundary surface, and $\partial/\partial\xi$ is an exterior derivative in the direction normal to the boundary. All interior derivatives in Eq. (4.1) can be differenced in exactly the same fashion at the boundaries as at interior points of the computational space (see subsection 4.1.2). The exterior derivatives must be treated differently. Before doing so, however, it is instructive to interpret geometrically the central difference operators that are employed in subsection 4.1.2.

As demonstrated in Ref. 6, the use of central difference operators at an interior grid point of the computational space is equivalent to applying the finite-volume method (Refs. 17, 18) to a cubical cell enclosing that grid point. As illustrated in Fig. 4-1a for a cross-sectional plane ζ = const., half-integer subscripts effectively define the faces of a cubical cell of unit volume $\Delta\xi \ \Delta\eta \ \Delta\zeta = 1$ that encloses each interior point. The dashed lines in the figure delineate the cell boundaries. If Eq. (4.1) is integrated over the volume of cell jkl in the figure and the resulting equation is divided by the cell volume $\Delta\xi \ \Delta\eta \ \Delta\zeta$ then, for example, there appears a term that represents the first derivative $\partial\hat{f}/\partial\xi$ as

$$(\partial\hat{f}/\partial\xi)_{jk\ell} = (\hat{f}_{j+1/2,k,\ell} - \hat{f}_{j-1/2,k,\ell})/\Delta\xi = \delta_j \hat{f}_{jk\ell}$$

$$\Delta\xi = 1 \qquad (4.20a)$$

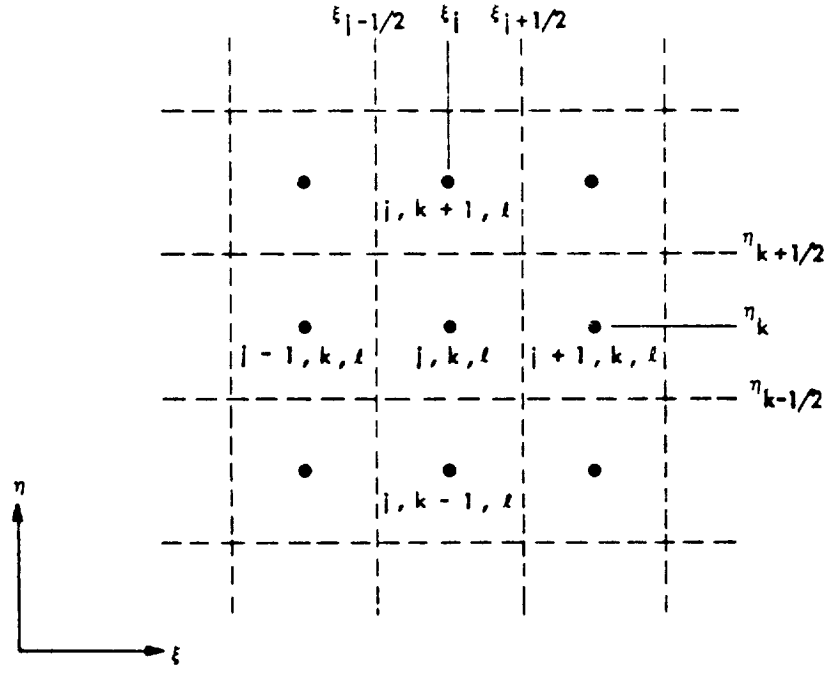

Fig. 4-1a Sketch of Computational Grid in a Plane ζ = Constant

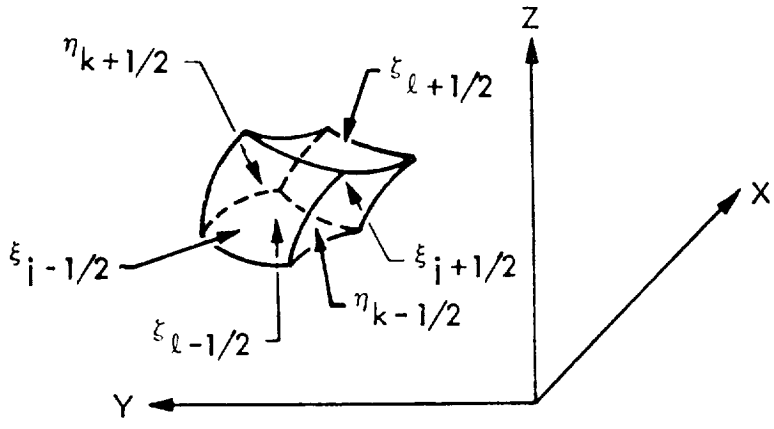

Fig. 4-1b Image of Cell j , k , ℓ in Physical Space

In the finite volume method, the value of $\hat{f}$ at a cell face is defined as the average of values at the two neighboring grid points

$$\hat{f}_{j+1/2,k,\ell} = (\hat{f}_{jk\ell} + \hat{f}_{j+1,k,\ell})/2 = \mu_j \hat{f}_{j+1/2,k,\ell} \tag{4.20b}$$

When the left-hand equality of (4.20b) is substituted into that of (4.20a), the resulting equation is identical to Eq. (4.13a); namely, the central difference that is obtained by applying the operators δ_j and μ_j in sequence. Similar results hold for all the spatially differentiated terms of Eq. (4.1). Furthermore, by the mean value theorem, the first term in the volume integrated version of (4.1) represents the time derivative of the cell-averaged value of $\hat{q}$, and is properly located at the cell centroid; i.e., at the grid point j, k, ℓ (Ref. 6). This geometrical interpretation simplifies the task of devising boundary-point difference operators that are consistent with the central differences employed at interior points. We consider first the outflow boundary $\xi = \xi_{max}$.

Outflow Boundary. Associated with each point of the outflow boundary is a half-cell, as illustrated in Fig. 4-2. The centroid of the half-cell is indicated by the asterisk. For the outflow boundary, the only exterior derivative in Eq. (4.1) is the first term in parentheses on the L.H.S. The natural differencing of this term that is compatible with the use of (4.20a) at the adjacent interior point is

$$\left(\frac{\partial \hat{f}}{\partial \xi}\right)_J \sim (\hat{f}_J - \hat{f}_{J-1/2})/(\Delta\xi/2) = \nabla_j \hat{f}$$

$$\Delta\xi = 1 \tag{4.21}$$

where the indicated equivalence to the backward difference operator of Eq. (4.19b) follows from Eq. (4.20b). The time derivative term in (4.1) must be applied at the centroid of the half-cell

$$\left(\frac{\partial \hat{q}}{\partial \tau}\right)_J \sim \frac{\Delta \hat{q}_*}{\Delta \tau} \tag{4.22a}$$

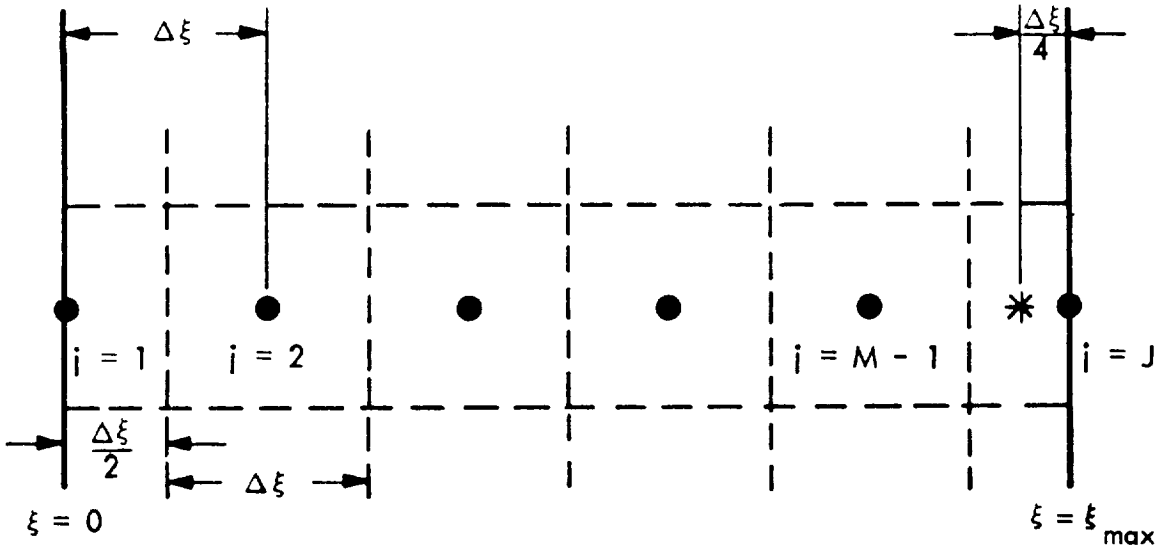

Fig. 4-2 Sketch of Interior Cells and Boundary Half-Cells Along the Coordinate ξ

The latter can be related to the corresponding quantities at the neighboring grid points within the spatial order of accuracy of (4.21) by linear interpolation (Refs. 6 and 15)

$$\Delta\hat{q}_* = (3\,\Delta q_J + \Delta\hat{q}_{J-1})/4$$

$$= [I - (1/4)\,\nabla_j]\,\Delta\hat{q}_J \tag{4.22b}$$

Upon inserting Eqs. (4.21) and (4.22) into Eq. (4.1) along with the central difference operators of subsection 4.1.2 for the interior spatial derivatives $\partial/\partial\eta$ and $\partial/\partial\zeta$, the time linearization and implicit operator factorization can be performed directly to yield an ADI sequence similar to the interior point sequence (4.16) for interior points. The first step of the sequence for outflow boundary point is

$$[I + \Delta\tau\,\nabla_j\,(F^n - \alpha I)]\,\Delta\hat{q}^{**}_{J,k,\ell} = \hat{r}_{J,k,\ell} \tag{4.23a}$$

$$\alpha = 1/4\,\Delta\tau \tag{4.23b}$$

where the term on the R.H.S. can be obtained from the interior point equation (4.17) by the substitution $\mu_j\,\delta_j \rightarrow \nabla_j$ in the first term on the right of the latter equation. The other steps of the sequence are identical to those given by Eqs. (4.16b through d).

The described sequence is valid only for purely supersonic outflow, or for problems that involve an external flow. In these cases, the full set of flow equations is used at the outflow boundary, and the latter is situated downstream of the nozzle exit (see subsection 2.4.6). For purely internal flows, we must modify the ADI sequence to account for the boundary condition given in Eq. (2.31). With the aid of the equation of state (2.6b) and the definition of $\hat{q}$ given below Eq. (2.9), the boundary condition can be written in the form

$$\mathcal{J}(\hat{q}) = \hat{q}_5 - \hat{q}_1^{-1}\left(\hat{q}_2^2 + \hat{q}_3^2 + \hat{q}_4^2\right) - J/\gamma\,(\gamma - 1) = 0 \tag{4.24}$$

where $\hat{q}_i$, $i = 1,2,\ldots,5$ denote the components of the vector $\hat{q}$ and J is the Jacobian of Eq. (2.10). This boundary condition is to be satisfied at time τ^{n+1}

$$\mathcal{J}^{n+1}(\hat{q}) = 0 \tag{4.25a}$$

The latter is linearized in time as follows:

$$\mathcal{J}^{n+1} = \mathcal{J}^n + \left(\frac{\partial \mathcal{J}}{\partial \hat{q}}\right)^n \Delta\hat{q} = 0 \tag{4.25b}$$

We write the linearized boundary condition in the form

$$\nu^n \Delta\hat{q} = -\mathcal{J}^n \tag{4.26a}$$

where ν denotes the row vector

$$\nu = \frac{\partial \mathcal{J}}{\partial \hat{q}} = (V^2/2\ ,\ -u\ ,\ -v\ ,\ -w\ ,\ 1) \tag{4.26b}$$

The linearized algebraic boundary condition is used in place of the u-momentum equation, i.e., in place of the third component of the time-linearized and spatially differenced version of Eq. (4.1). The resulting vector equation can be written in the operational form

$$\left\{M + \Delta\tau\left[\nabla_j(\tilde{F} - \alpha\tilde{I}) + \mu_k\delta_k\tilde{G} + \mu_\ell\delta_\ell\tilde{H} - Re^{-1}(\delta_k\tilde{R} + \delta_\ell\tilde{S})\right]\right\}^n \Delta\hat{q}_{Jk\ell} = \tilde{r}_{Jk\ell} \tag{4.27}$$

All elements are zero in the third row vector of each of the matrices $\tilde{F}$, $\tilde{I}$, $\tilde{G}$, $\tilde{H}$ and of the operator matrices $\tilde{R}$, $\tilde{S}$; the matrices otherwise are identical to F, I, G, H, R, S

as defined in subsection 4.1.1. The third row vector of the matrix M is ν as defined in Eq. (4.26b); the other elements of M are those of the identity matrix I. Finally, the third component of the vector on the right of (4.27) is equal to the R.H.S. of Eq. (4.26a); the other components are those of $\hat{r}_{Jk\ell}$ in Eq. (4.23a).

The operator on the left of (4.27) can be factored easily after multiplying the equation by M^{-1}, and the resulting ADI sequence can be written in the form (Ref. 14).

$$\left[M + \Delta\tau \nabla_j (\tilde{F} - \alpha\tilde{I})\right]^n \Delta\hat{q}^{**}_{Jk\ell} = \tilde{r}^n_{Jk\ell} \tag{4.28a}$$

$$\left[M + \Delta\tau (\mu_k \delta_k \tilde{G} - Re^{-1} \delta_k \tilde{R})\right]^n \Delta\hat{q}^{*}_{Jk\ell} = M^n \Delta\hat{q}^{**}_{Jk\ell} \tag{4.28b}$$

$$\left[M + \Delta\tau (\mu_\ell \delta_\ell \tilde{H} - Re^{-1} \delta_\ell \tilde{S})\right]^n \Delta\hat{q}_{Jk\ell} = M^n \Delta\hat{q}^{*}_{Jk\ell} \tag{4.28c}$$

Inflow Boundary. The algebraic inflow boundary conditions on the total pressure, total temperature, and transverse velocity components (see subsection 2.4.5) are treated in the manner described above for the algebraic outflow boundary condition in Eq. (2.31). The implicitly-differenced form of the mass conservation equation is used along with the algebraic inflow boundary conditions to form a complete system of implicit linearized equations for inflow boundary grid points. The ADI sequence has the same form as Eq. (4.28) and can be obtained from the latter by the substitutions $J \rightarrow 1$, $\alpha \rightarrow -\alpha$, and $\nabla_j \rightarrow \Delta_j$. Note that the latter substitution also must be made in the R.H.S. term $\hat{r}$.

Freestream Boundaries. The computational space described in Section 3 is such that the freestream boundary conditions of subsection 2.4.3 apply at either of the boundaries $\eta = \eta_{max}$, $\zeta = \zeta_{max}$, depending upon the nature of the curvilinear coordinate system. For the grid geometry depicted in Fig. (3-6a), both are freestream boundaries. We describe below the treatment of Eq. (4.1) for boundary points $\eta = \eta_{max}$ (k = K).

The interior derivatives $\partial/\partial\xi$, $\partial/\partial\zeta$ are differenced centrally as for interior and points (see subsection 4.1.2). Backward difference operators are used to represent the exterior first derivatives $\partial\hat{g}/\partial\eta$ and $\partial\theta^{(\xi)}/\partial\eta$ in the manner described earlier for exterior derivatives at the outflow boundary. The derivative $\partial\hat{\theta}^{(\eta)}/\partial\eta$ is differenced as

$$\frac{\partial\theta^{(\eta)}}{\partial\eta} \sim \left(\hat{\theta}^{(\eta)}_{j,K,\ell} - \hat{\theta}^{(\eta)}_{j,K-1/2,\ell}\right)\Big/(\Delta\eta/2)$$

In view of the boundary conditions (2.27b), the spatially differenced form of Eq. (4.1) for the boundary point j, K, ℓ then becomes

$$(I - (1/4)\nabla_k)\Delta\hat{q}_{j,K,\ell} + \Delta\tau\,(\mu_j\delta_j\hat{f} + \nabla_k\hat{g} + \mu_\ell\delta_\ell\hat{h})^{n+1} = -\Delta\tau\,Re^{-1}\left\{2E_k^{-1/2}\left[\hat{\theta}^{(\eta)}_{j,K,\ell}\right]^{n+1} + E_k^{-1}\left[\hat{\theta}^{(\xi)}_{j,K,\ell}\right]^{n}\right\} \tag{4.29}$$

where E is the classical shift operator (Ref. 16). For a mesh function $f_{j,k,\ell}$, the shift operators in Eq. (4.29) are defined by

$$E_k^{-1} f_{jk\ell} = f_{j,k-1,\ell} \tag{4.30a}$$

$$E_k^{-1/2} f_{jk\ell} = f_{j,k-1/2,\ell} \tag{4.30b}$$

Upon performing the time-linearization Eqs. (4.3) and (4.5a), the resulting implicit difference equation is

$$\left\{I + \Delta\tau\left[\mu_j\delta_j F + \nabla_k(G - \alpha I) + 2\,Re^{-1}E_k^{-1/2}R + \mu_\ell\delta_\ell H\right]^n\right\}\Delta\hat{q}_{jK\ell} = \hat{r}^n_{jK\ell} \tag{4.31a}$$

and

$$\hat{r}_{jK\ell} = -\Delta\tau \left\{ \mu_j \delta_j \hat{f} + \nabla_k \hat{g} + \mu_\ell \delta_\ell \hat{h} + Re^{-1} \left[2\, E_k^{-1/2}\, \hat{\theta}^{(\eta)} + E_k^{-1}\, \hat{\theta}^{(\xi)} \right] \right\}^n_{jK\ell} \qquad (4.31b)$$

Note that the differential operator $\partial/\partial\eta$ that enters into the quantities $\hat{\theta}^{(\eta)}$ and R [see Eq. (2.10b) and Eq. (A.4) of Appendix A] may be replaced by the central difference operator δ_k as is done in subsection 4.1.2 for interior points, because the operator $E_k^{-1/2}$ shifts the point of application of the operator δ_k backward by half the mesh spacing.

The three algebraic boundary conditions (2.27a) are used in place of the mass, u-momentum, and energy equations, i.e., in place of the first, second, and fifth components of the vector Eq. (4.31). The final ADI sequence for the freestream boundary points then can be obtained in a fashion analogous to that employed in Eqs. (4.24) to (4.28) for outflow boundary points.

Wall Boundaries. The ADI sequence for wall-boundary points can be obtained in a fashion similar to that outlined above for the freestream boundary. As shown in Ref. 15, the algebraic boundary conditions (2.21) replace the three momentum equations, namely, the second, third, and fourth components of the vector equation (4.1). When the wall temperature is specified according to Eq. (2.22), the latter replaces the energy equation (Ref. 15) namely the fifth component of Eq. (4.1). For an adiabatic wall, the boundary conditions (2.21) and (2.23b) simplify the spatially-differenced form of the energy equation in much the same way as the freestream boundary conditions (2.27b) contribute to the simplicity of Eqs. (4.31).

Symmetry Planes. At a symmetry plane such as the vertical plane $\eta = 0$ for the nozzle configuration depicted in Fig. (3.6a), the exterior derivatives $\partial/\partial\eta$ in Eq. (4.1) are evaluated as described in subsection 2.4.3. In the third component of the vector Eq. (4.1), these derivatives vanish according to Eq. (2.25). In the

remaining four components, the differential operator $\partial/\partial\eta$ may be replaced by the forward difference operator Δ_k, which is consistent with Eq. (2.26).

The treatment of the time derivative term $\Delta\hat{q}/\Delta\tau$ is different from that used at all other types of boundary. At a symmetry boundary, each boundary point is considered to lie at the centroid of a full cell enclosing the point. The time-derivative term thus is centered at the grid point itself, and the counterpart of Eq. (4.22b) does not apply.

Once the time-linearization is performed, the resulting implicit operator may be factored to obtain the ADI operator sequence corresponding to the interior point sequence (4.16).

4.3 SMOOTHING

The algorithm of subsection 4.1 is neutrally stable (Ref. 13)in that short wavelength spatial disturbances are undamped. An explicit smoothing term is appended to the R.H.S. of Eq. (4.16) to prevent nonlinear instabilities and to provide a dissipative mechanism for computing embedded shock waves. Steger (Ref. 3) and Pulliam and Steger (Ref. 7) employ a nonconservative fourth-order smoothing term for each coordinate direction. Such higher-order terms do not compromise the second-order spatial accuracy of the algorithm. However, the analysis given in Ref. 6 shows that these nonconservative smoothing terms generate errors in global conservation that degrade the solution. This degradation is confirmed by the numerical experiments described in Section 5. This defect is overcome by the conservative smoothing term developed by Thomas (Ref.15). The form of this term for the ξ coordinate direction is

$$s_{jk\ell} = -(\beta\Delta\tau)\,\delta_j J\delta_j^3 \vec{q}_{jk\ell} \tag{4.32a}$$

$$s_{2k\ell} = -(\beta\Delta\tau)\,E_j^{1/2}\,J\delta_j^3 \vec{q}_{jk\ell} \tag{4.32b}$$

where J is the Jacobian in Eq. (4.10) and β is a constant. The first equation applies at those interior points located more than two mesh intervals $\Delta\xi$ from the boundaries, and the second equation applies at the point $j = 2$ immediately adjacent to the left hand boundary in Fig. 4-2. The corresponding term for the point adjacent to the right hand boundary is obtained from Eq. (4.32b) by the substitution $E_j^{1/2} \rightarrow -E_j^{-1/2}$. No smoothing term is applied at the end points themselves. The smoothing terms in Eq. (4.32) remain valid at boundary points that lie in the surfaces $\eta = \text{const.}$ or $\zeta = \text{const.}$ where the difference operators δ_j represent interior derivatives $\partial/\partial\xi$.

Similar smoothing terms apply for the other two coordinate directions η, ζ. For grid points in the neighborhood of a symmetry plane, the smoothing term for the direction normal to the symmetry plane is similar to Eq. (4.32a), with appropriate modification to account for the symmetry properties of $\vec{q}$. The linear stability boundary of the set of smoothing terms is (Ref. 15)

$$\Delta\tau \sum_{i=1}^{3} \beta_i \left\{ 1 + (\Delta x_i/2) \max_{x_i} [\partial(\ell n J)/\partial x_i] \right\} \leq 1/8 \qquad (4.33)$$

where x_i, $i = 1, 2, 3$ represents the coordinate directions ξ, η, ζ, respectively. The smoothing coefficients β_i must be selected to satisfy this inequality.

4.4 PROPERTIES OF THE NUMERICAL METHOD

A linear stability analysis shows that the difference equations of subsection 4.1 are unconditionally stable for arbitrary values of the time step $\Delta\tau$ (Ref. 19). Since only the steady-state solution is of interest in the present application, we point out several important features of the method that ensure an accurate steady state solution.

First, at steady state, the term $\hat{r}$ on the R.H.S. of Eq. (4.16a) vanishes [cf. Eq. (2.20)]. Because Eqs. (4.16) yield a direct solution for the change in the flow variable vector

over a time step, the fact that $\hat{r}$ is proportional to $\Delta\tau$ implies that the steady state solution is independent of the magnitude of the time step (Ref.13). The accuracy of the solution then depends only on the accuracy with which the spatial derivative terms in Eq. (2.20) are represented on the finite-difference grid and, of course, on the fineness of the grid. These derivatives are approximated at interior points by difference operators whose truncation error is of second order in the spatial grid spacing, and can be expected to yield reasonable accuracy for a given grid. The difference operators employed at boundary points have a local truncation error that is of first order in the grid spacing. However, by examining the entire system of difference equations for the computational domain, one can show that global second-order accuracy is achieved; i.e., the global truncation error is of second order (Ref. 15). Furthermore, strict global conservation is maintained to within machine roundoff error. That is, the difference equations possess the same property of global conservation as the partial differential Eq. (2.20).

The global conservation property of the differential equations spanning the physical flow region is that only the fluxes through the boundary of the region contribute to the volume integral of the physical variables. For the difference equations given in subsections 4.1 and 4.2, the volume integral of the physical variables is expressed naturally as a quadrature sum. When the difference equations are summed with the appropriate weights of the quadrature, global conservation is achieved if the physical fluxes make a net contribution only at the boundaries, and any ad hoc smoothing terms make no contribution.

It is easy to show that the weighted sum of the difference equations over all interior and boundary grid points retains the global conservation property of the differential equations when the weights are chosen according to the midpoint quadrature rule. The latter is appropriate because it is consistent with the second-order spatial accuracy of the central difference operators that are employed at interior points of the grid. The smoothing terms presented in subsection 4.3 are differenced in a conservative fashion and obey homogeneous boundary conditions. This ensures that the weighted sum of these terms over all grid points forms a telescoping series in which the contributions from adjacent interior points cancel, and the contribution from each boundary point is zero. Thus, the smoothing terms do not compromise the global conservation property of the difference equations.

Section 5
NUMERICAL EXPERIMENTS

An array of numerical experiments have been conducted to test various aspects of the numerical method. The bulk of the experiments have been performed to develop and verify methods of computing the boundary conditions that are valid throughout the subsonic, transonic, and supersonic flow regimes. Experiments also have been performed to explore the effects of explicit smoothing terms on the solution.

The test problem selected is that of the external laminar flow over a flat plate of finite length at a freestream Reynolds number $Re_\infty = 10^5$, Prandtl number $Pr = 1$, and viscosity proportional to temperature, $\mu = T$. For the subsonic flow experiments, the freestream Mach number is $M_\infty = 0.1$. The computational grid for this case is shown in Figs. 5-1 and 5-2, and features parabolic boundary-layer curvilinear coordinates. The lateral outer computational boundary is placed approximately ten boundary layer thicknesses away from the plate. The grid is stretched exponentially in the z direction to resolve the thin viscous layer. The number of grid points in the x, y, and z directions is $15 \times 5 \times 15$. The stretching in the z direction places about half of the grid points within the boundary layer.

All test runs employ the implicit adiabatic wall boundary computation technique of Ref. 15 (see section 4.2.2). The initial conditions are as follows. Pressure is assumed uniform and equal to its freestream value, $p = 1$. Velocity is taken from the Blasius boundary layer solution for incompressible flow (Ref. 20). Temperature is computed from the velocity through the Crocco relation, and density follows from the equation of state.

Each set of experiments is discussed below in a separate subsection. The conclusions drawn are summarized separately at the end of each subsection.

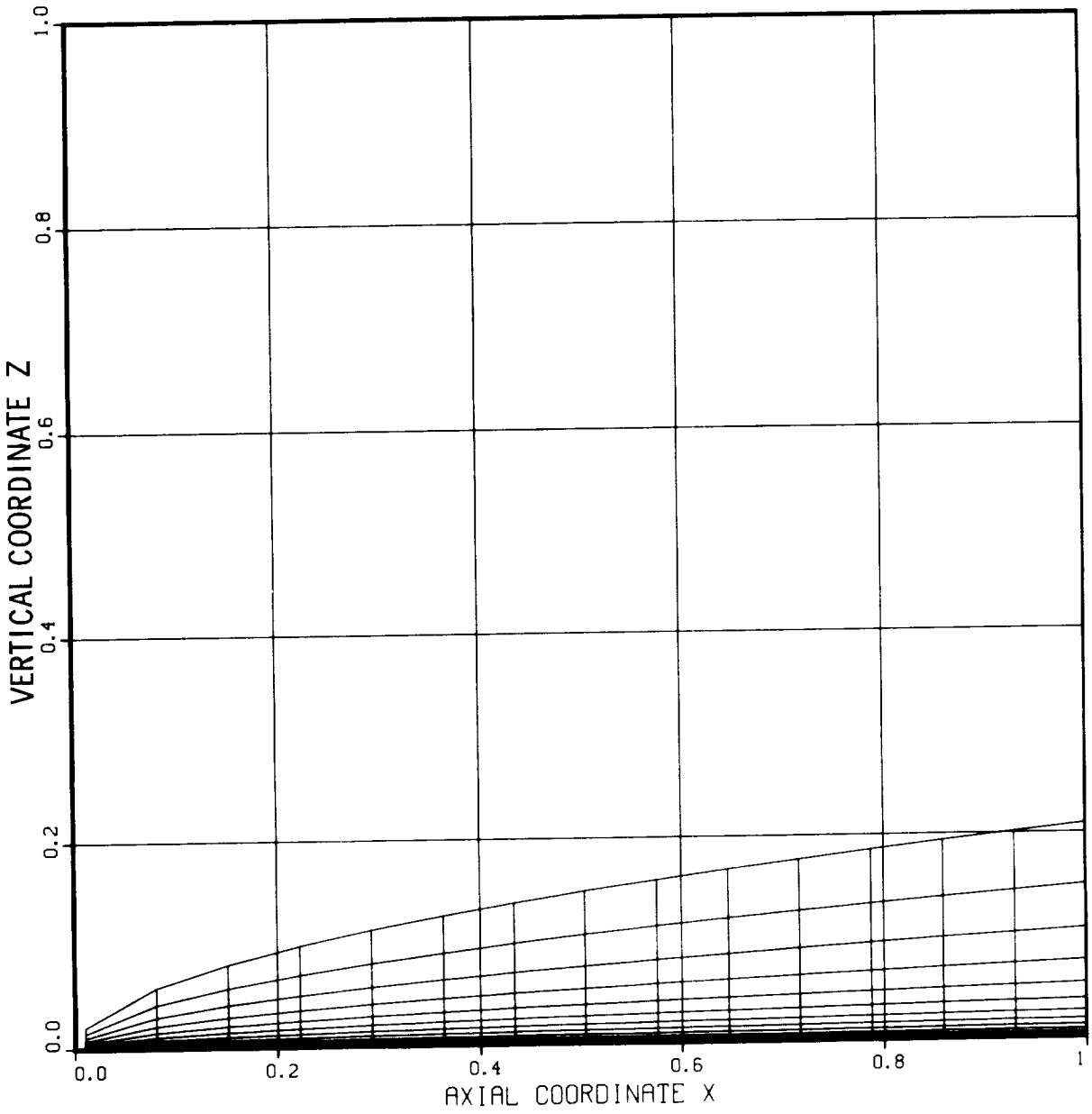

Fig. 5-1 Side View of Computational Grid in Physical Space for Flat Plate Geometry, $M_\infty = 0.1$, $Re_\infty = 10^5$

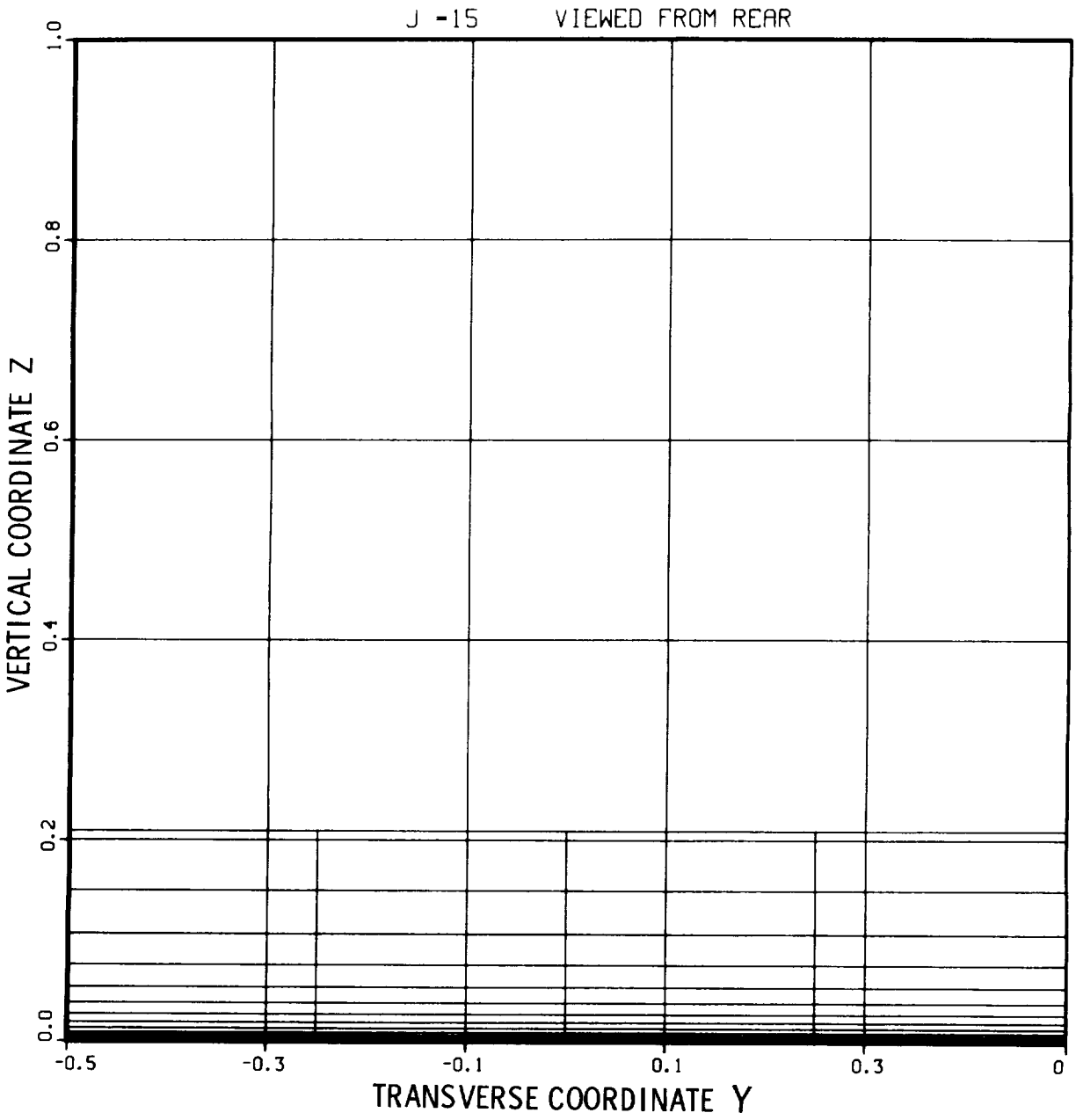

Fig. 5-2 Computational Grid for Flat Plate Geometry Viewed From Rear. $M_\infty = 0.1$, $Re_\infty = 10^5$

5.1 OUTFLOW BOUNDARY CONDITION TESTS

As discussed in section 2.4.5, the quasi-one-dimensional theory of characteristics implies that no boundary conditions are to be specified when the x-component of outflow velocity is supersonic, $u > c$. Conditions at the boundary exert no influence on the upstream flow, and simple extrapolation methods can be used to compute the flow variables at the boundary. An improvement over extrapolation is to compute the flow variables from the equations, using "upwind" difference operators for the terms that contain spatial derivatives in the direction normal to the boundary (Ref. 6). Such operators are termed "conservative" if the resulting difference equations possess the same global conservation property as the differential equations that govern the flow (see Section 4.4). This conservative outflow boundary computation procedure has been applied successfully by Thomas and Lombard (Ref. 6) in supersonic external viscous flows that contain a subsonic region embedded in the near-wall region of the boundary layer. The presence of an outer supersonic region was believed responsible for the success of this procedure, inasmuch as characteristics theory suggests that a boundary condition is required when the flow is subsonic (see section 2.4.6).

According to the latter theory, four characteristics are directed from the interior toward the boundary, and one emanates from the boundary toward the interior. The latter is responsible for the upstream influence of the boundary, and implies that a boundary condition is necessary, say, the boundary pressure. The boundary condition, together with the four compatibility relations that hold along the other four characteristics then could be used to compute the flow variables at points of the boundary where $u < c$. The implicit solution of the compatibility relations in a fashion consistent with the implicit method for interior points is much more complicated than the conservative outflow boundary computation procedure. Numerical experiments therefore have been performed to investigate the validity of the latter procedure for subsonic and transonic flows.

The test case is for the flat plate problem described earlier, with a freestream Mach number $M_\infty = 0.1$. Freestream boundary conditions $p = \rho = 1$, $u = M_\infty$, $v = w = 0$ were imposed at the lateral outer boundary $z = z_{max}(x)$, and held fixed throughout

the computation. Conditions at the inflow boundary also were held fixed at their initial values. The nonconservative smoothing terms (Refs. 3, 7, and 13) were used. A constant time stepsize $\Delta\tau = 0.005$ was used. This value is twenty times larger than the stable limit of explicit numerical schemes as given by the Courant stability criterion. That is, the Courant number for the calculation is $Co = 20$.

Figure 5-3 shows the computed surface pressure distribution after 100 steps. The pressure peak at the left is probably a result of the simple inflow boundary condition. Note the smoothness of the pressure distribution near the trailing edge of the plate where the conservative outflow boundary computation procedure is used. This result shows that the procedure yields smooth, stable results even when the subsonic region is not confined to the near-wall portion of the viscous layer.

We conclude that the procedure is valid for subsonic and transonic flow, as well as for the supersonic external flow problems for which it was employed originally in Ref. 6. It is likely that the success of the procedure is due partly to the use of conservative boundary-point difference operators, and partly to the fact that the viscous flow equations are spatially parabolic in the transverse y, z directions, rather than being strictly hyperbolic as assumed in the quasi-one-dimensional theory of characteristics. We conjecture that the parabolicity allows information about the freestream conditions to be transmitted along the outflow boundary to the wall, and obviates the need for the pressure to be specified as a boundary condition. Having confirmed its general validity, the conservative outflow boundary computation procedure is used in all subsequent numerical computations.

5.2 FREESTREAM BOUNDARY CONDITIONS

Although the numerical experiment just described confirmed the validity of the conservative outflow boundary condition procedure, it revealed that a truly steady-state solution is difficult to obtain for subsonic flow $M_\infty < 1$ if all freestream flow conditions are imposed at the lateral outer boundary $z = z_{max}$. Further computation shows that, although the numerical method remains stable for Courant numbers

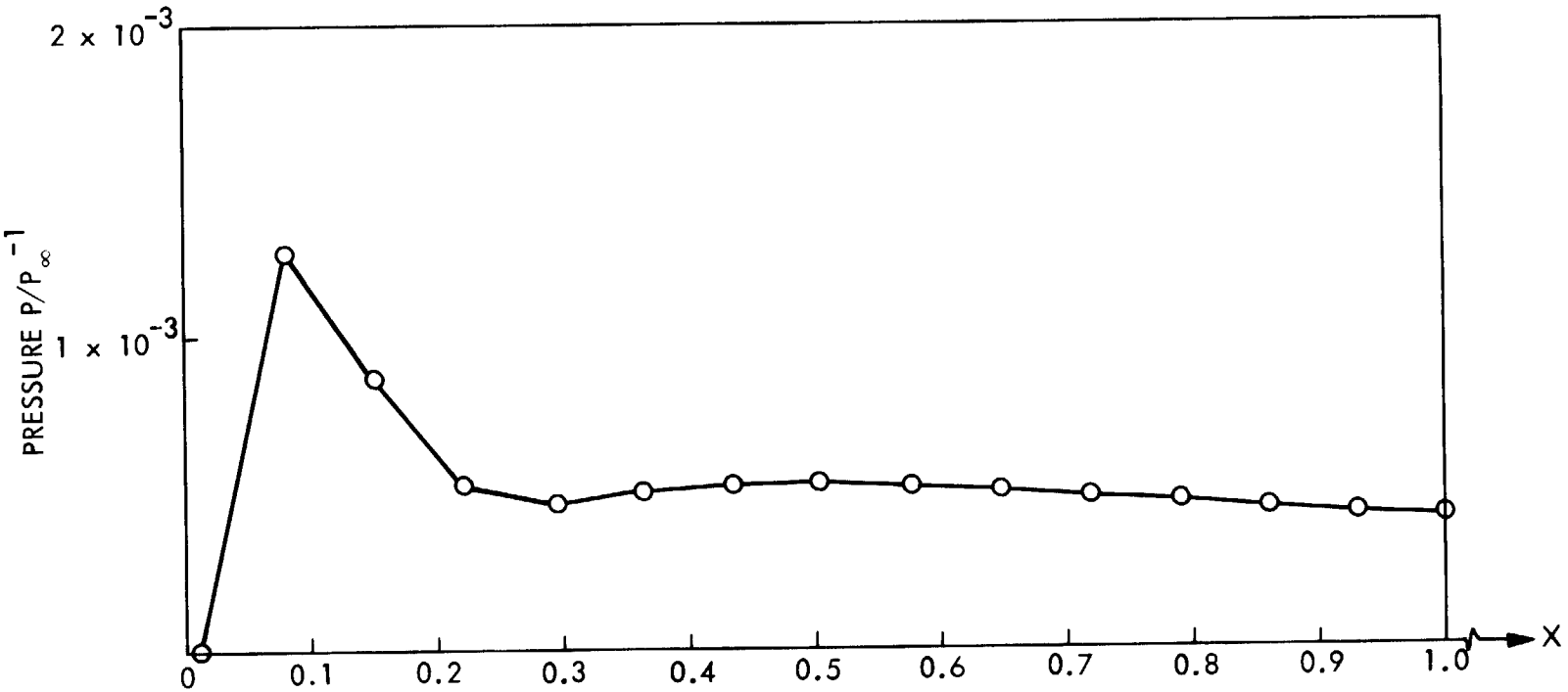

Fig. 5-3 Surface Pressure Distribution for Case 1 (a) After 100 Steps. Courant No. $Co_{max} = 20$

as high as 400, the solution continues to change with time even after many hundreds of steps. After many numerical experiments to investigate possible causes of the persistent unsteadiness in the solution, the evidence became strong that the difficulty lay in the use of freestream boundary conditions at the outer boundary.

It is known from second-order boundary layer theory that the displacement effect of the viscous layer near the wall induces a first-order perturbation of the outer inviscid flow (Ref. 21). Specifically, a finite velocity v is induced in the direction normal to the wall. Apparently, this induced normal velocity does not decay with distance away from the wall in a wholly subsonic flow, and one cannot impose at the outer computational boundary the freestream conditions $v = w = 0$, no matter how far that boundary is placed from the wall.

A variety of numerical experiments were conducted to develop a valid method for the outer boundary. The first of these experimented with a generalization of the conservative outflow boundary computation procedure in which the only boundary conditions applied were that the viscous stress and heat conduction terms must vanish at the boundary because the freestream flow is inviscid. All flow variables then are computed implicitly from the mass, momentum, and energy conservation equations. However, better results were obtained by imposing freestream boundary conditions on the density, streamwise velocity u, and pressure. The transverse velocity components v, w are computed from the transverse momentum equations as in the generalized outflow boundary computation procedure.

A steady-state solution was obtained in about 150 steps, using a time stepsize that corresponds to a Courant number $Co = 200$. The results are displayed in Figs. 5-4 to 5-11. The first seven of these figures show vertical profiles of the velocity components, the density, and the pressure. The velocity profiles at a station midway along the plate (Fig. 5-4) are smooth. Note that the vertical velocity v (dashed line) remains non-zero all the way to the outer boundary. The density profile of Fig. 5-5 at the same station is plotted on a greatly expanded scale, because the maximum density change between the wall and the freestream boundary is less than 0.2% at the

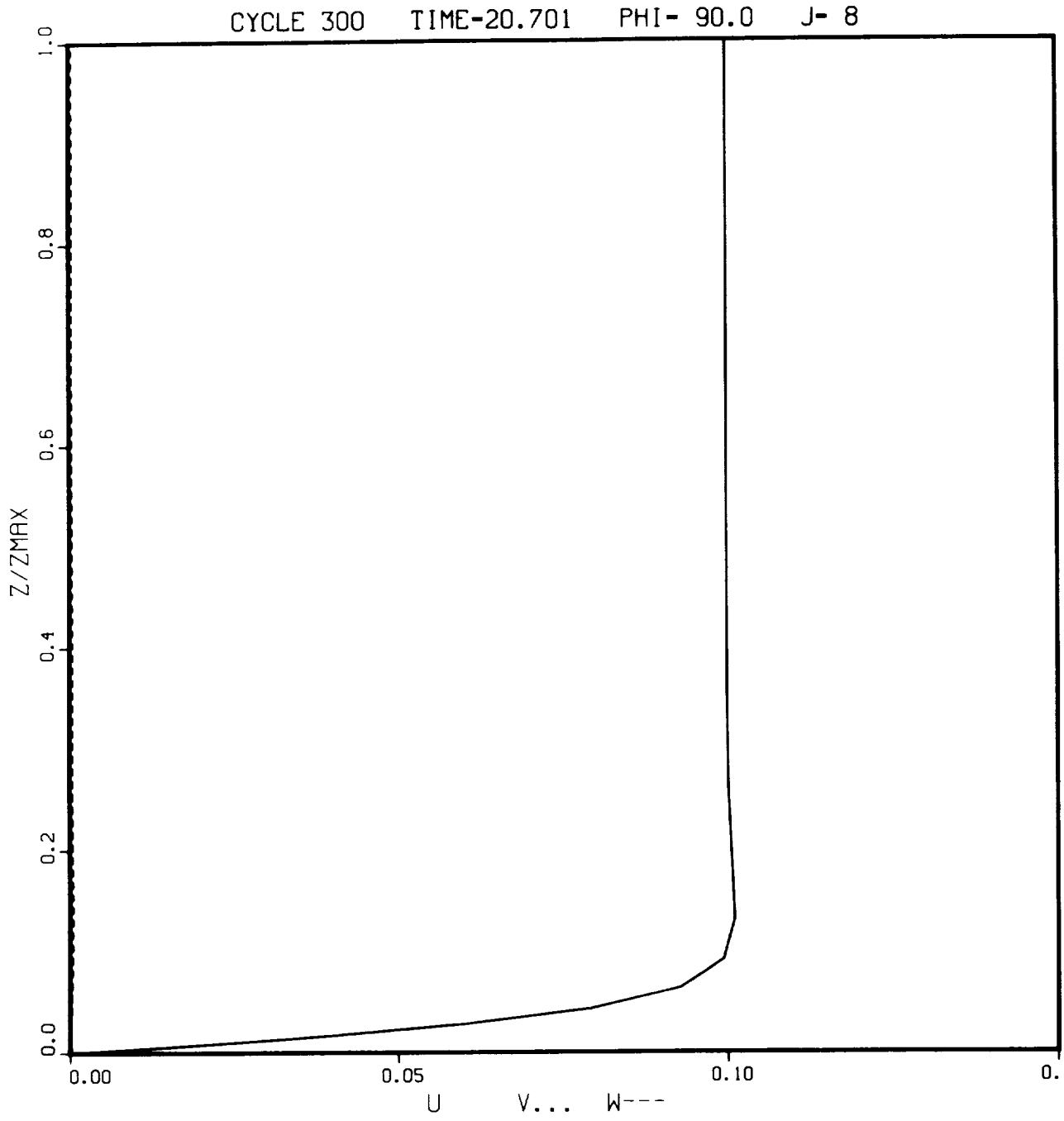

Fig. 5-4 Velocity Profiles at a Station Midway Along Plate, $M_\infty = 0.1$, $Re_\infty = 10^5$

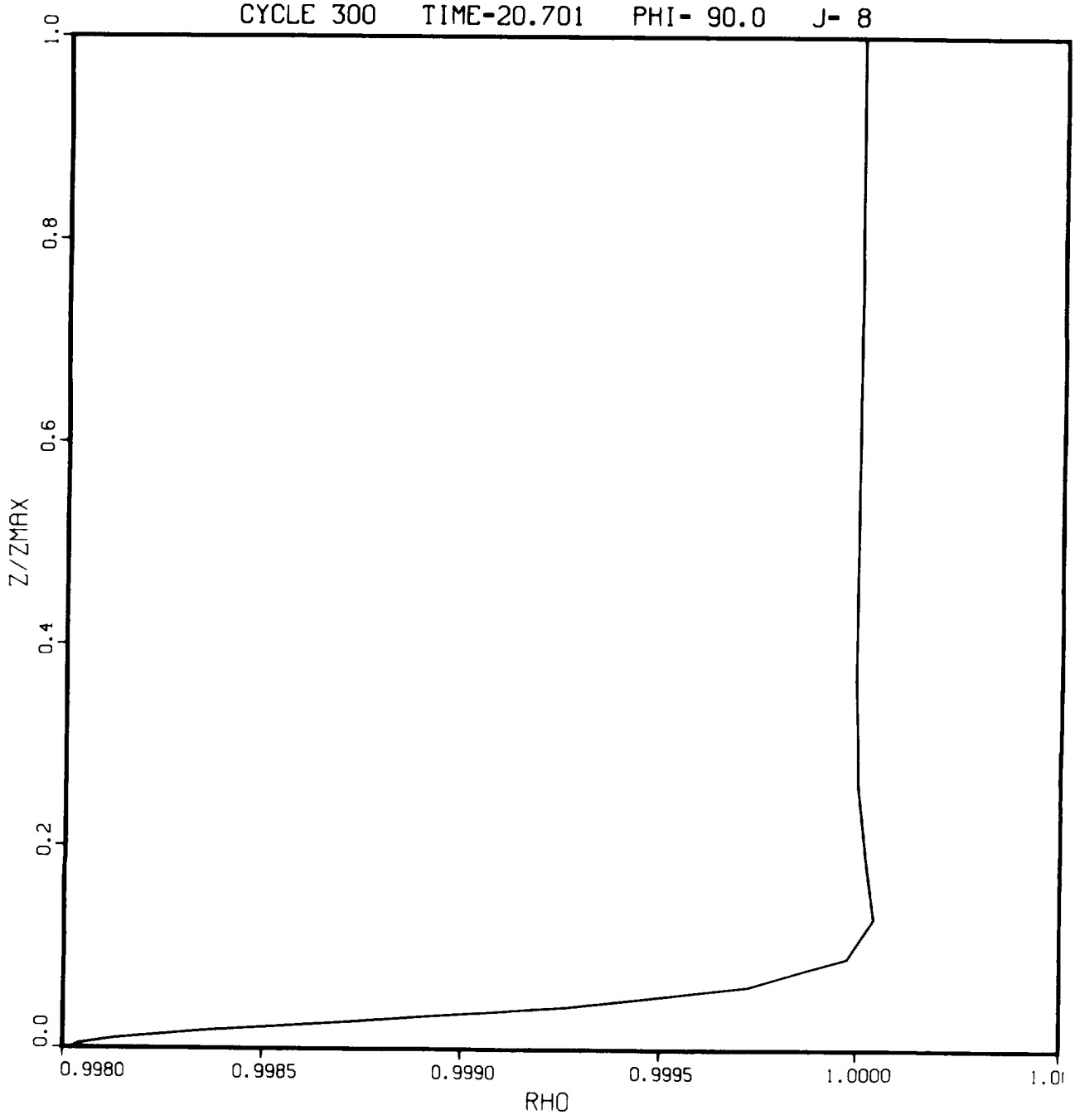

Fig. 5-5 Density Profile at a Station Midway Along Plate, $M_\infty = 0.1$

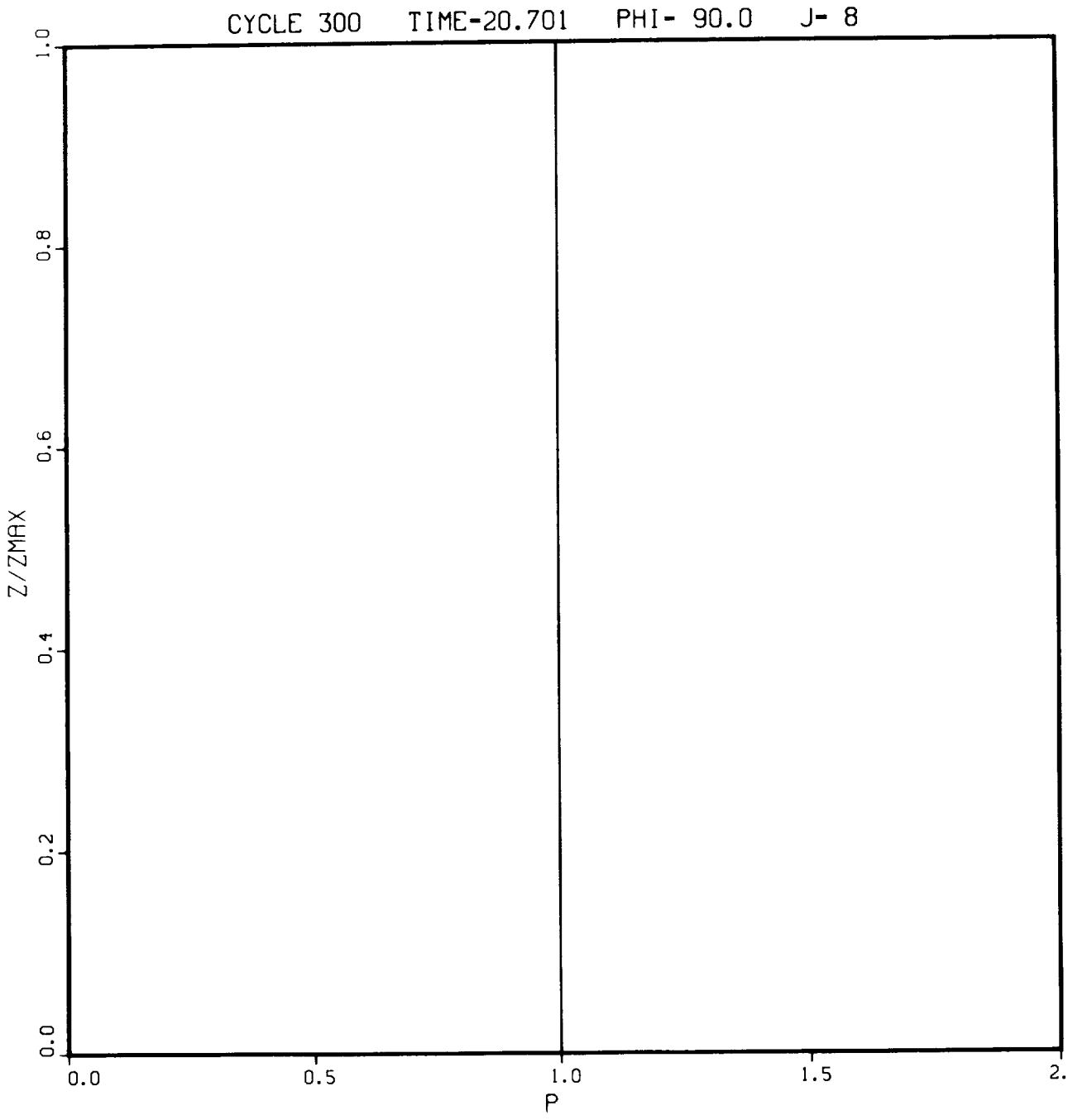

Fig. 5-6 Pressure Profile at a Station Midway Along Plate, $M_\infty = 0.1$

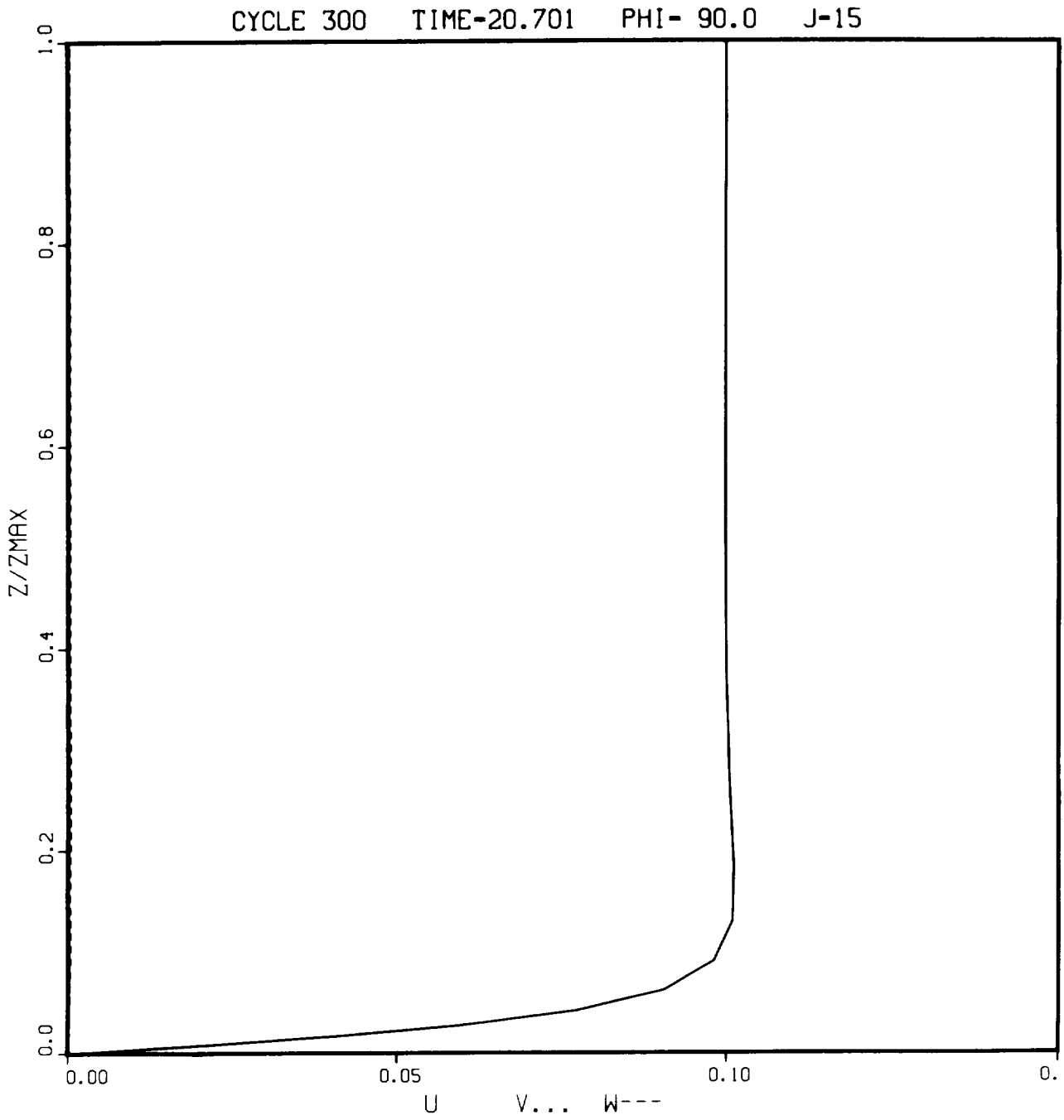

Fig. 5-7 Velocity Profiles at Trailing Edge, $M_\infty = 0.1$

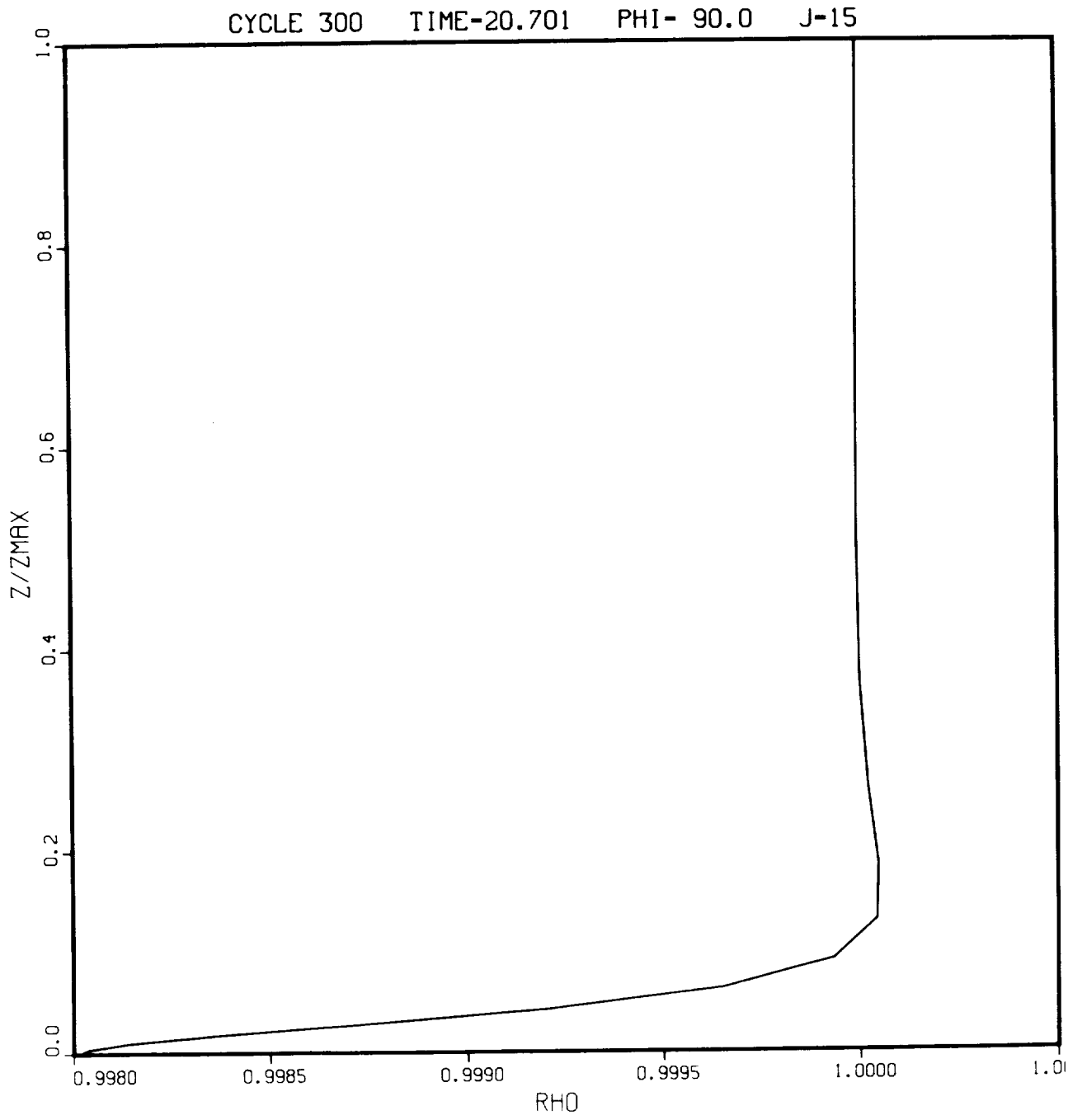

Fig. 5-8 Density Profile at Trailing Edge, $M_\infty = 0.1$

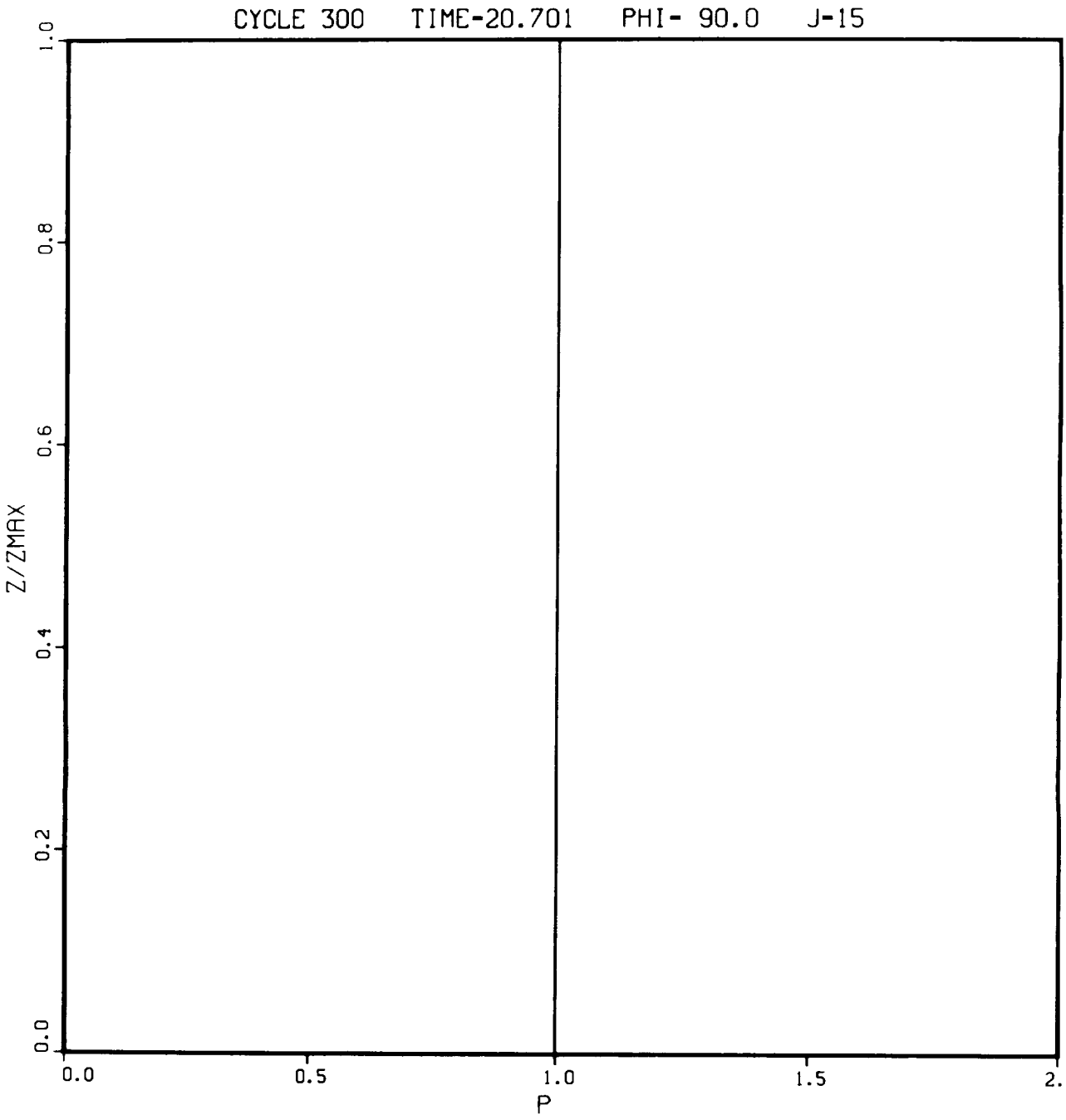

Fig. 5-9 Pressure Profile at Trailing Edge, $M_\infty = 0.1$

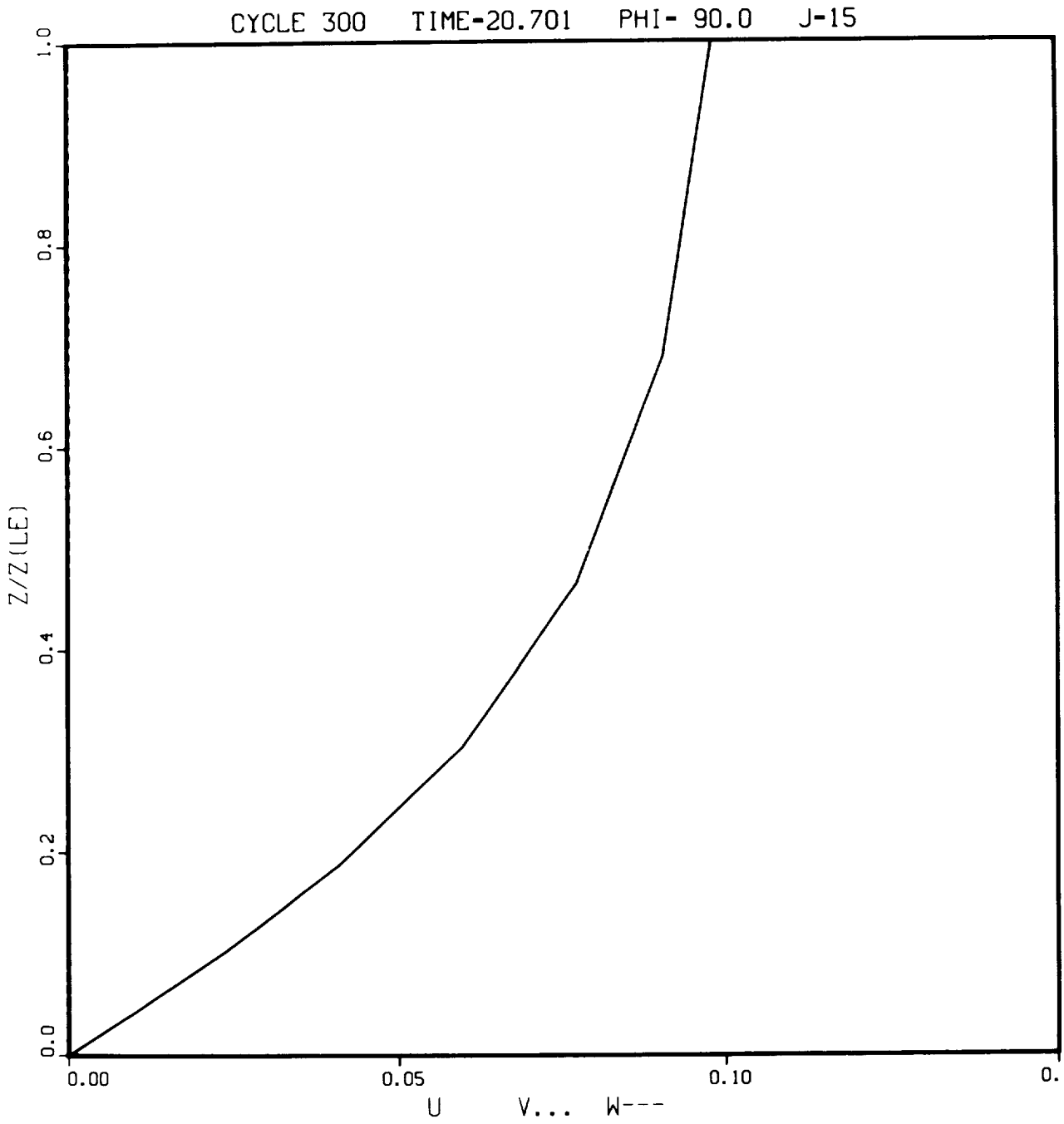

Fig. 5-10 Velocity Profiles Across Inner Viscous Layer at Trailing Edge, $M_\infty = 0.1$

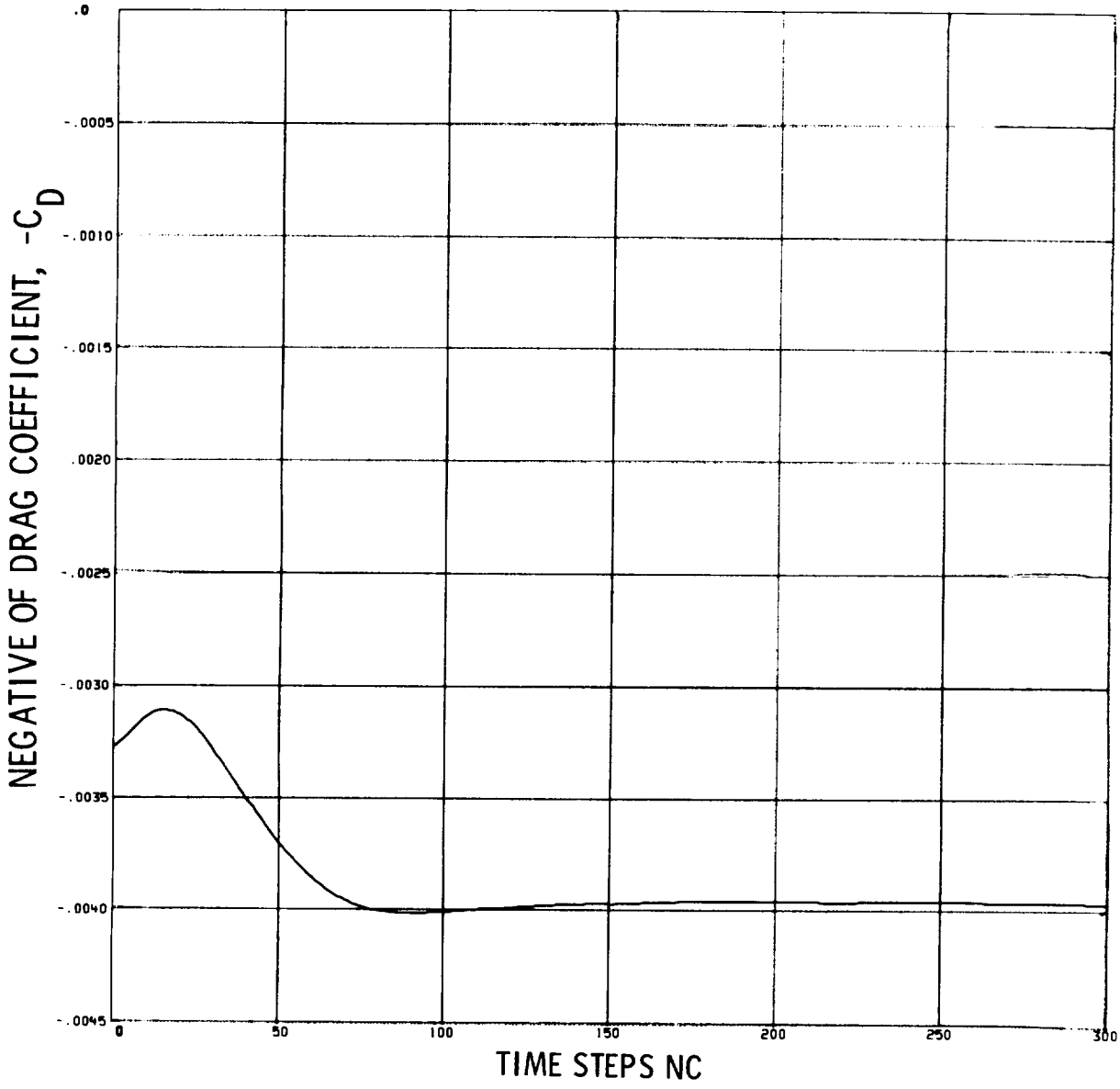

Fig. 5-11 Drag Coefficient as a Function of Number of Time Steps, $M_\infty = 0.1$. Maximum Courant Number Co = 200

very low freestream Mach number $M_\infty = 0.1$. The pressure is uniform across the entire computational region, as shown in Fig. 5-6.

The profiles are similar at the trailing edge of the plate, which coincides with the outflow boundary (Figs. 5-7 to 5-9). Figure 5-10 shows a magnified view of the velocity profiles across the near-wall viscous layer at the trailing edge.

We have found the computed drag coefficient to be a sensitive indicator of convergence to steady state. The variation in drag as a function of the number of time steps computed is shown in Fig. 5-11. The negative sign is associated with the sign convention used to denote the direction of a force component. The steady state is seen to be reached in less than 200 time steps, according to the drag computation. This was confirmed by the fact that an additional 100 steps produced no further change in any flow variable at any grid point, to within machine roundoff error. Furthermore, the root mean square residual over all grid points had decayed to the order of the machine roundoff error, where the residual is defined as the set of steady-state terms in the flow equations. By this definition, the residual should vanish at steady state.

The asymptotic steady state value of the computed drag coefficient is $C_D = 3.97 \times 10^{-3}$, about 5 percent lower than the value predicted by the approximate Blasius boundary layer solution for incompressible flow (Ref. 21). The Blasius value is

$$C_D = 1.328/\sqrt{Re_\infty} = 4.20 \times 10^{-3} \tag{5.1}$$

One would expect the same freestream boundary computation procedure to be valid for supersonic flow. This was confirmed by a successful computation for a freestream Mach number $M_\infty = 3$, again at a Reynolds number $Re_\infty = 10^5$. For a supersonic freestream, the viscous interaction induces a shock wave in the predominantly inviscid flow outside the viscous wall boundary layer. The computed surface pressure distribution in Fig. 5-12 shows that the shock-induced elevation in surface pressure is

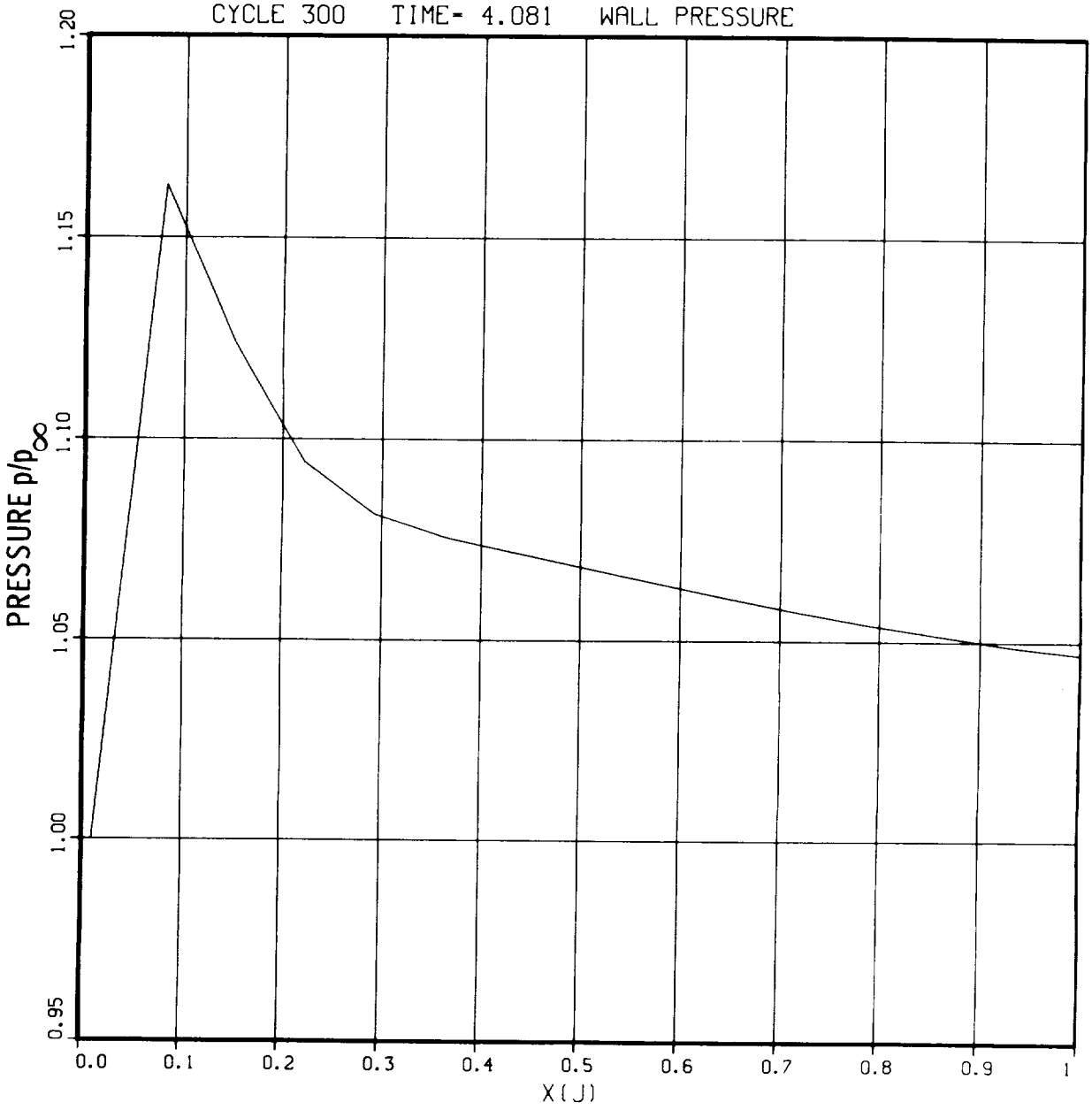

Fig. 5-12 Surface Pressure Distribution, $M_\infty = 3$

greatest near the leading edge, where the shock is strongest. Note the smooth variation in pressure all the way to the trailing edge, where the conservative outflow boundary computation procedure is used.

Figure 5-13 shows the velocity profiles at midplate. The weak embedded shock wave is evident in the abrupt decay of the vertical velocity v (dashed line) across the shock. The shock is poorly resolved by the exponentially stretched grid used in this test case. The shock is again evident in the pressure profile (Fig. 5-14) at the same station. The post-shock oscillation is common with such shocks that are "captured" by the numerical method, but probably is aggravated by the aforementioned poor resolution of the shock jump.

Similar velocity and pressure profiles at the trailing edge are displayed in Figs. 5-15 and 5-16. The density profile at the trailing edge is given in Fig. 5-17 to show the large density change that occurs across the boundary layer. The density change is a consequence of the temperature rise associated with viscous dissipation of kinetic energy, which is much greater here than in subsonic flow (cf. Fig. 5-8). Magnified views of the velocity, pressure, and density profiles across the inner viscous boundary layer region at the trailing edge are given in Figs. 5-18 to 5-20 to show the smoothness of the solution, and the good resolution that is achieved with as few as eight grid points across the layer.

The computed drag coefficient history is shown in Fig. 5-21. The Courant number based on the time stepsize is about 100 for this case, and steady state is again achieved within about 200 time steps. The computed drag coefficient at steady state is $C_D = 4.54 \times 10^{-3}$. According to laminar boundary-layer theory, the drag is independent of Mach number for $Pr = 1$ and viscosity proportional to temperature, and the incompressible Blasius value of Eq. (5.1) applies (Ref. 20). The computed drag is about 8 percent larger than the Blasius value. The discrepancy is not surprising, in view of the fact that boundary-layer theory neglects the viscous interaction, and does not account for the presence of the external shock wave.

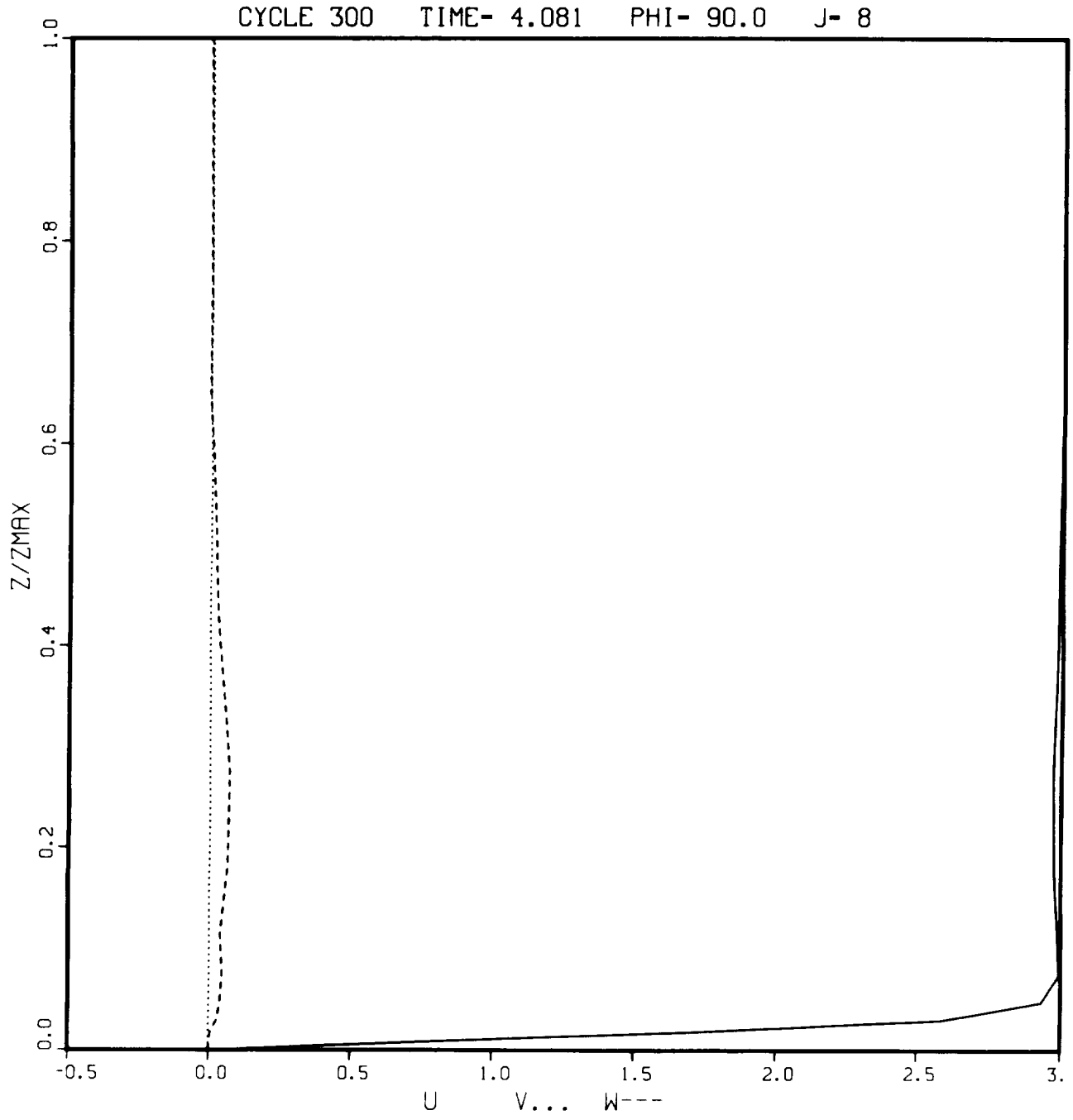

Fig. 5-13 Velocity Profiles at a Station Midway Along Plate, $M_\infty = 3$

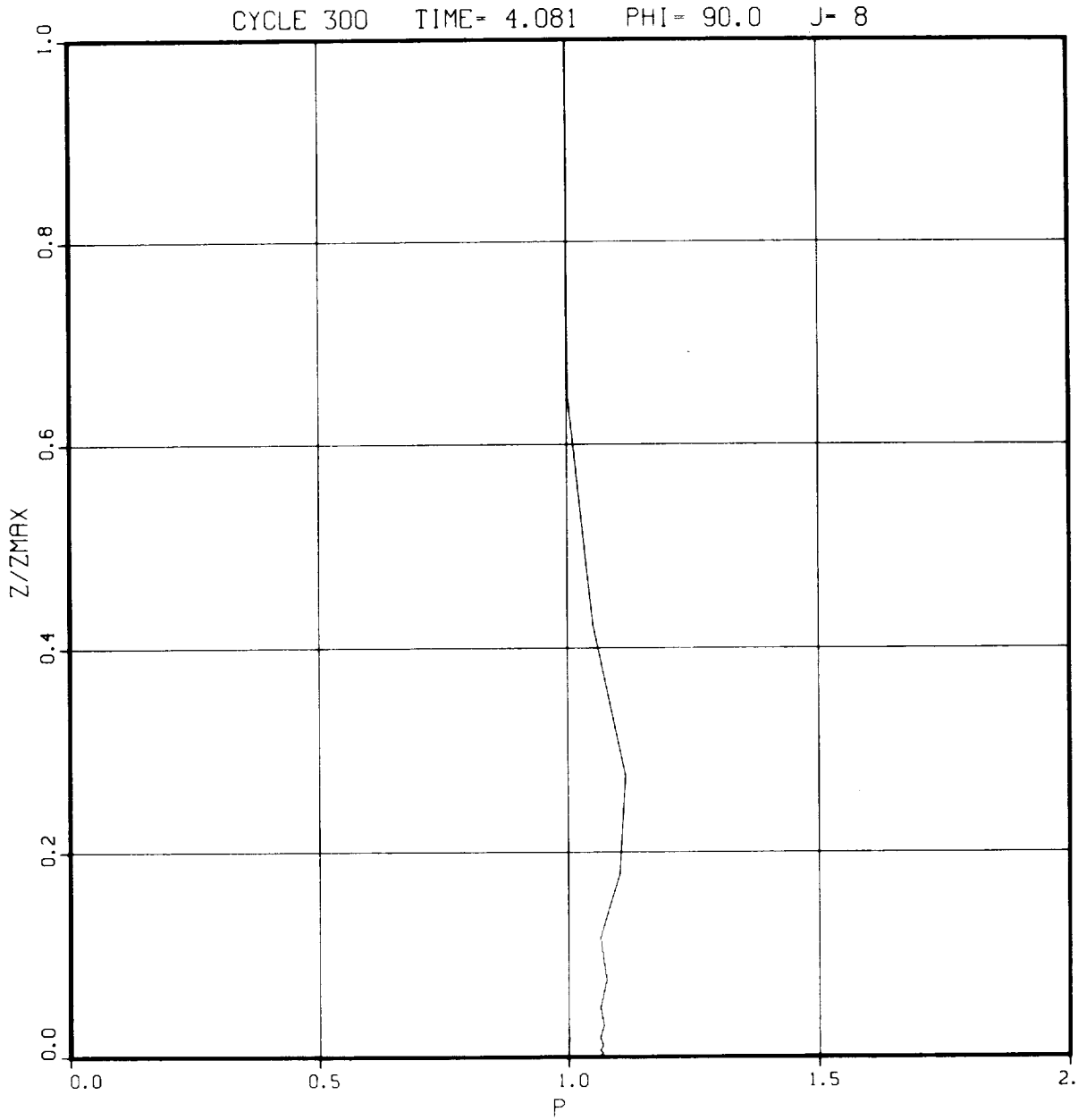

Fig. 5-14 Pressure Profile at a Station Midway Along Plate, $M_\infty = 3$

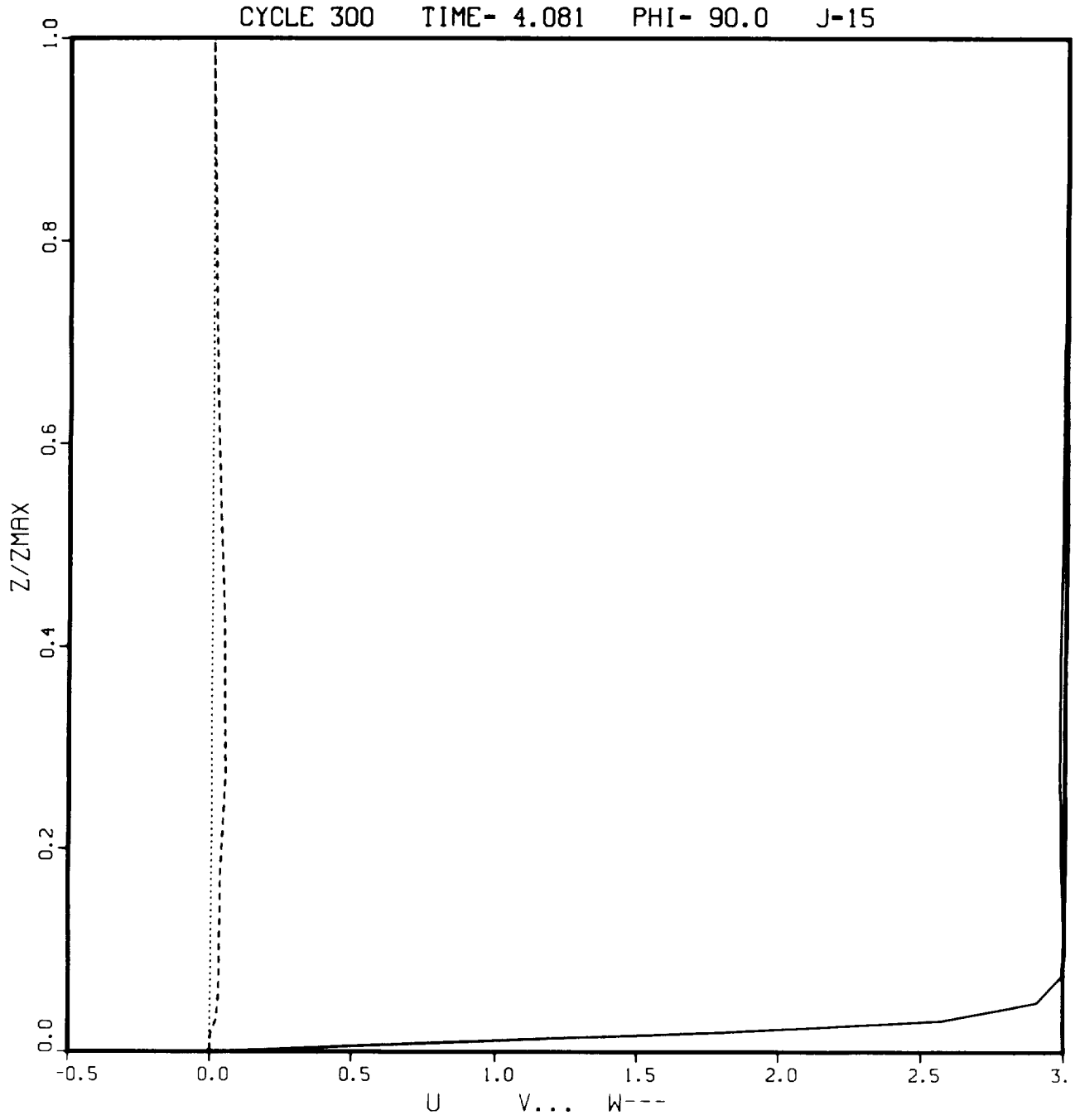

Fig. 5-15 Velocity Profiles at Trailing Edge, $M_\infty = 3$

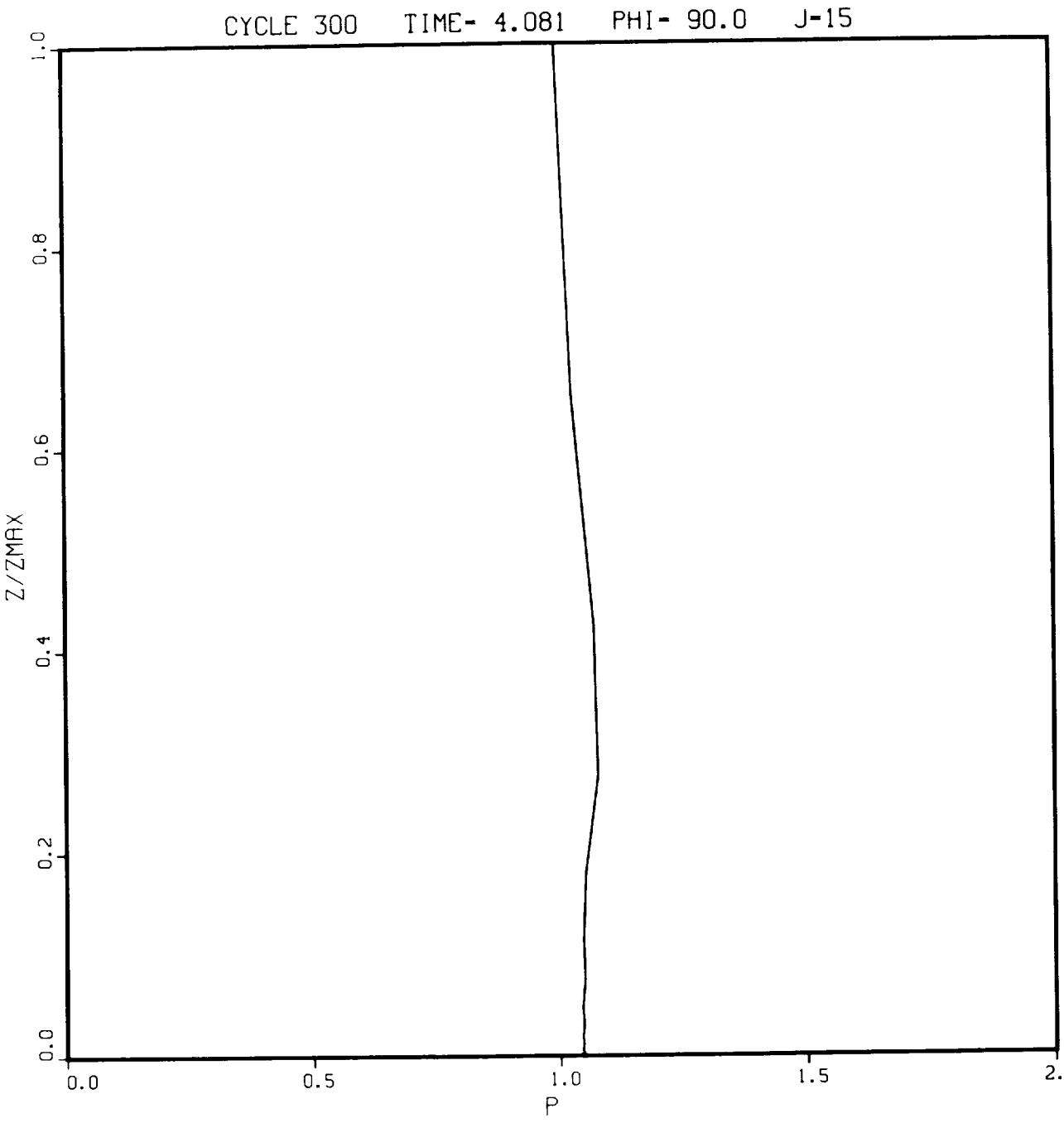

Fig. 5-16 Pressure Profile at Trailing Edge, $M_\infty = 3$

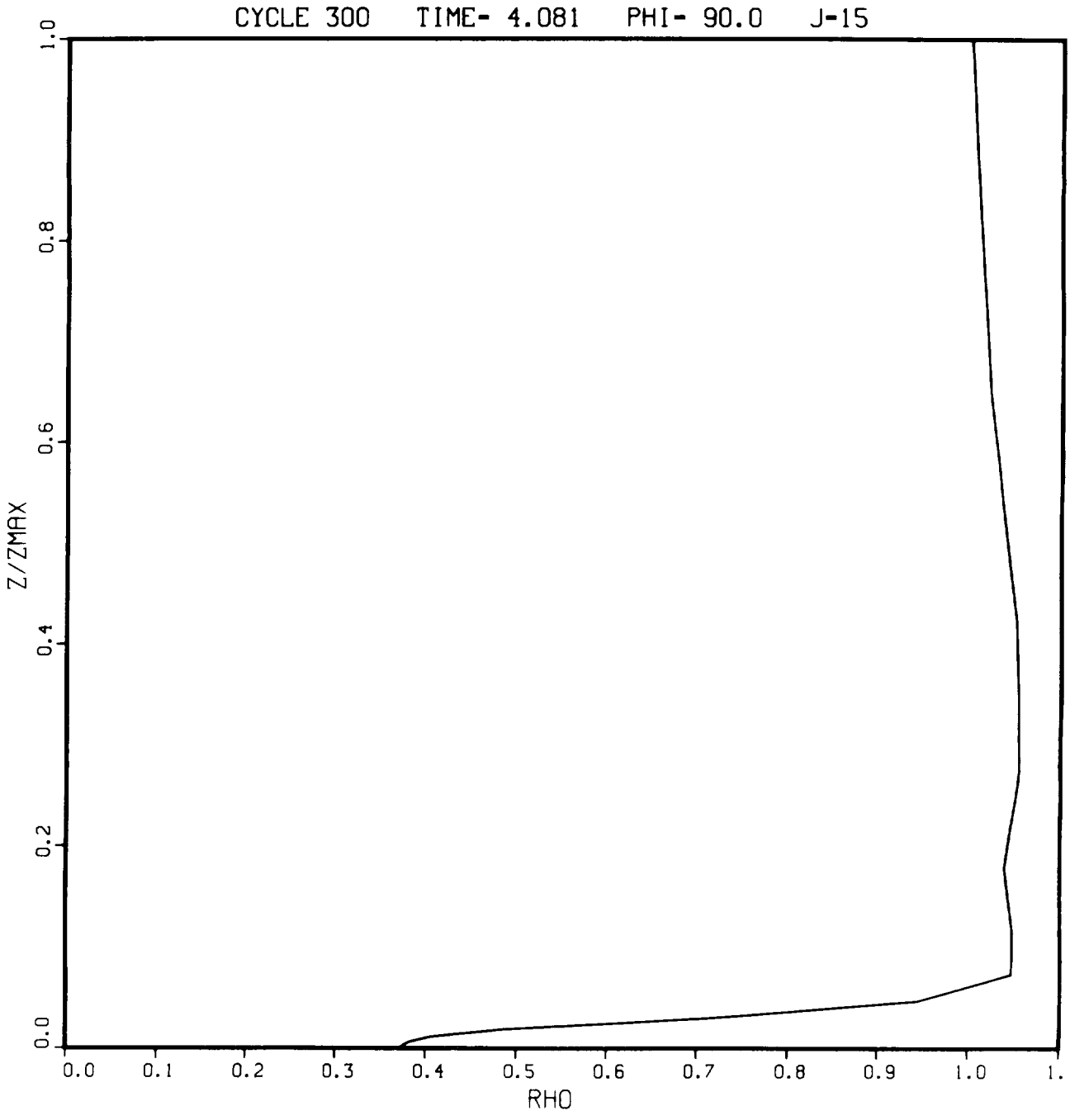

Fig. 5-17 Density Profile at Trailing Edge, $M_\infty = 3$

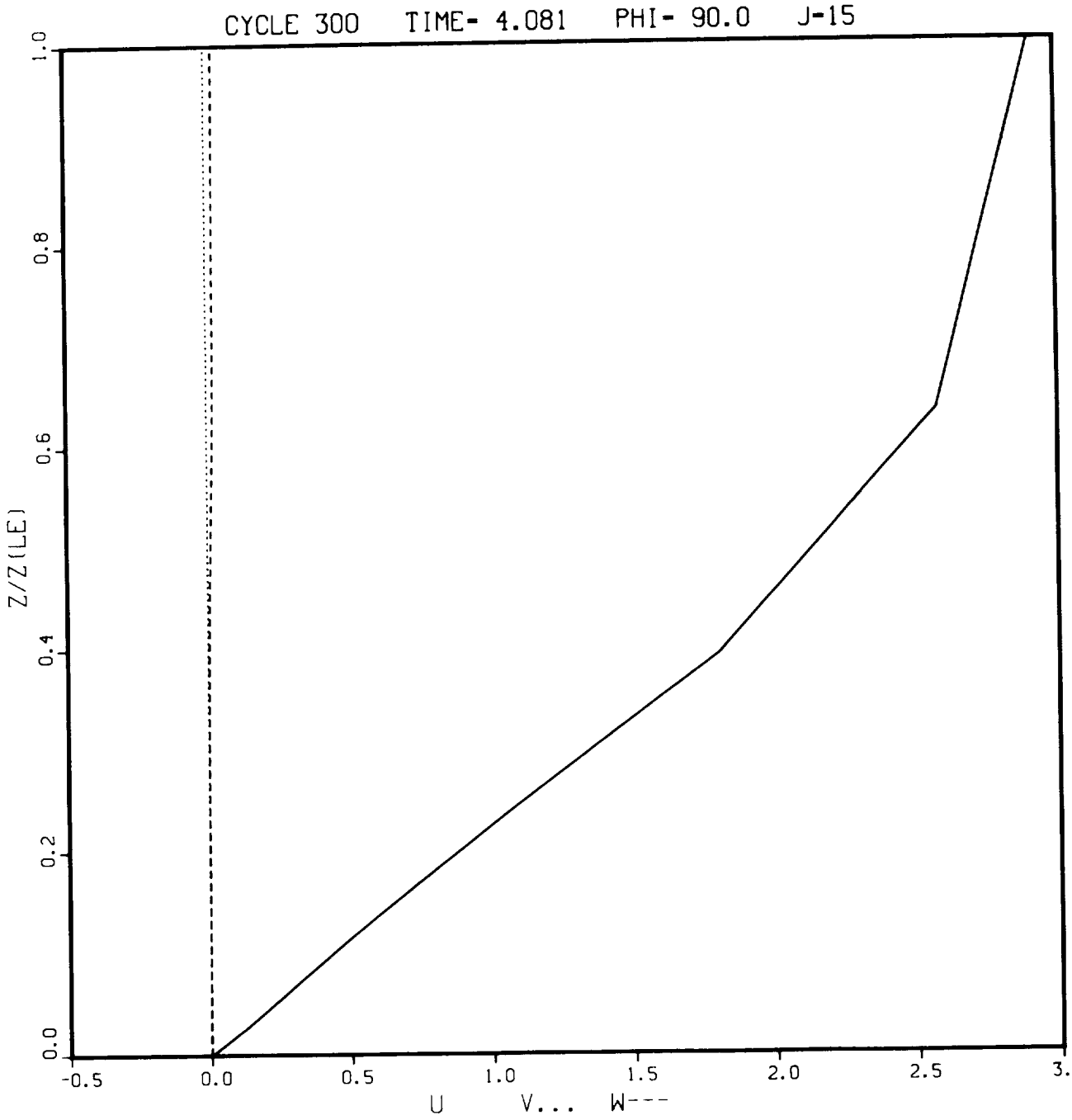

Fig. 5-18 Velocity Profiles Across Inner Viscous Layer at Trailing Edge, $M_\infty = 3$

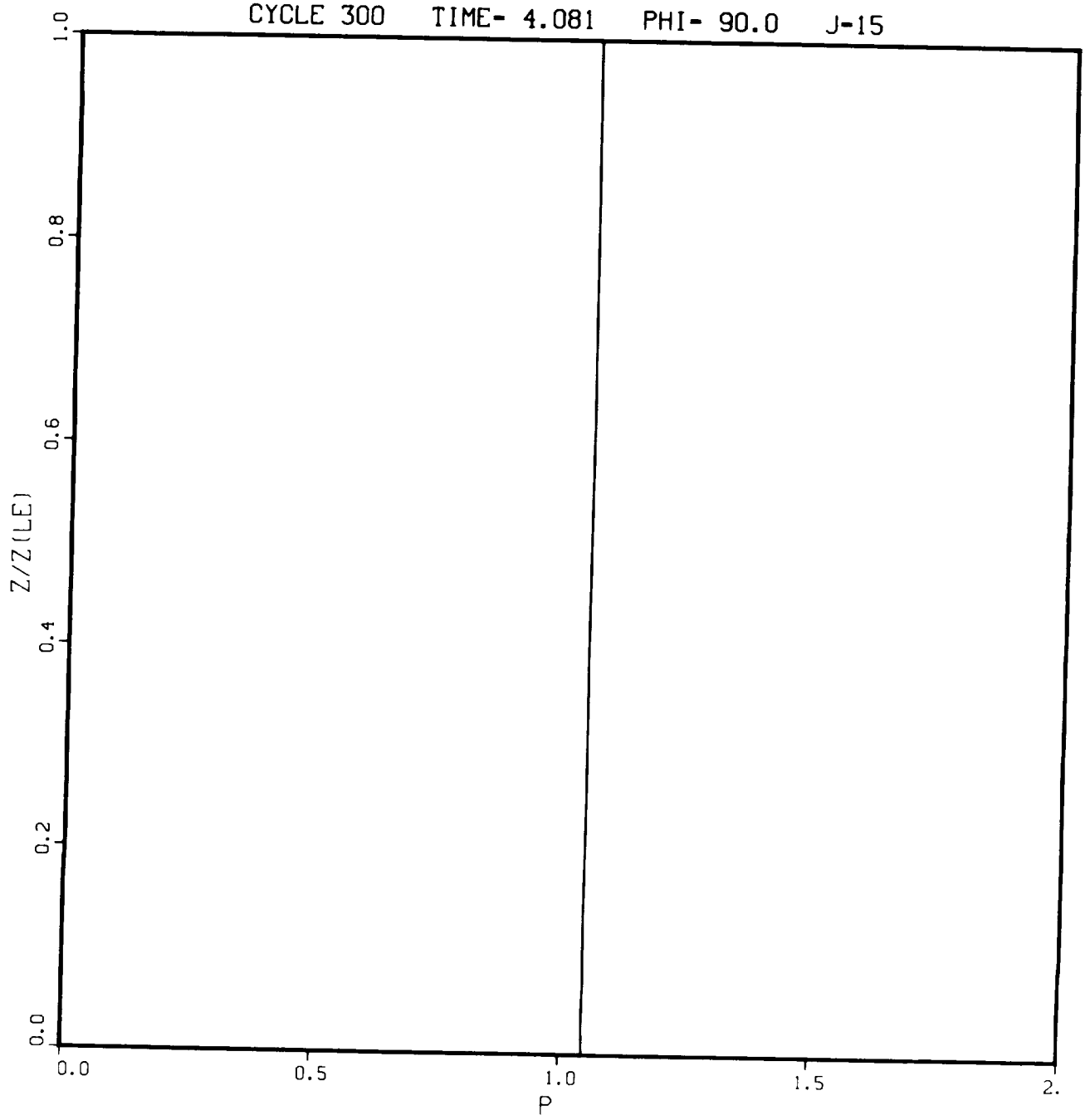

Fig. 5-19 Pressure Profile Across Inner Viscous Layer at Trailing Edge, $M_\infty = 3$

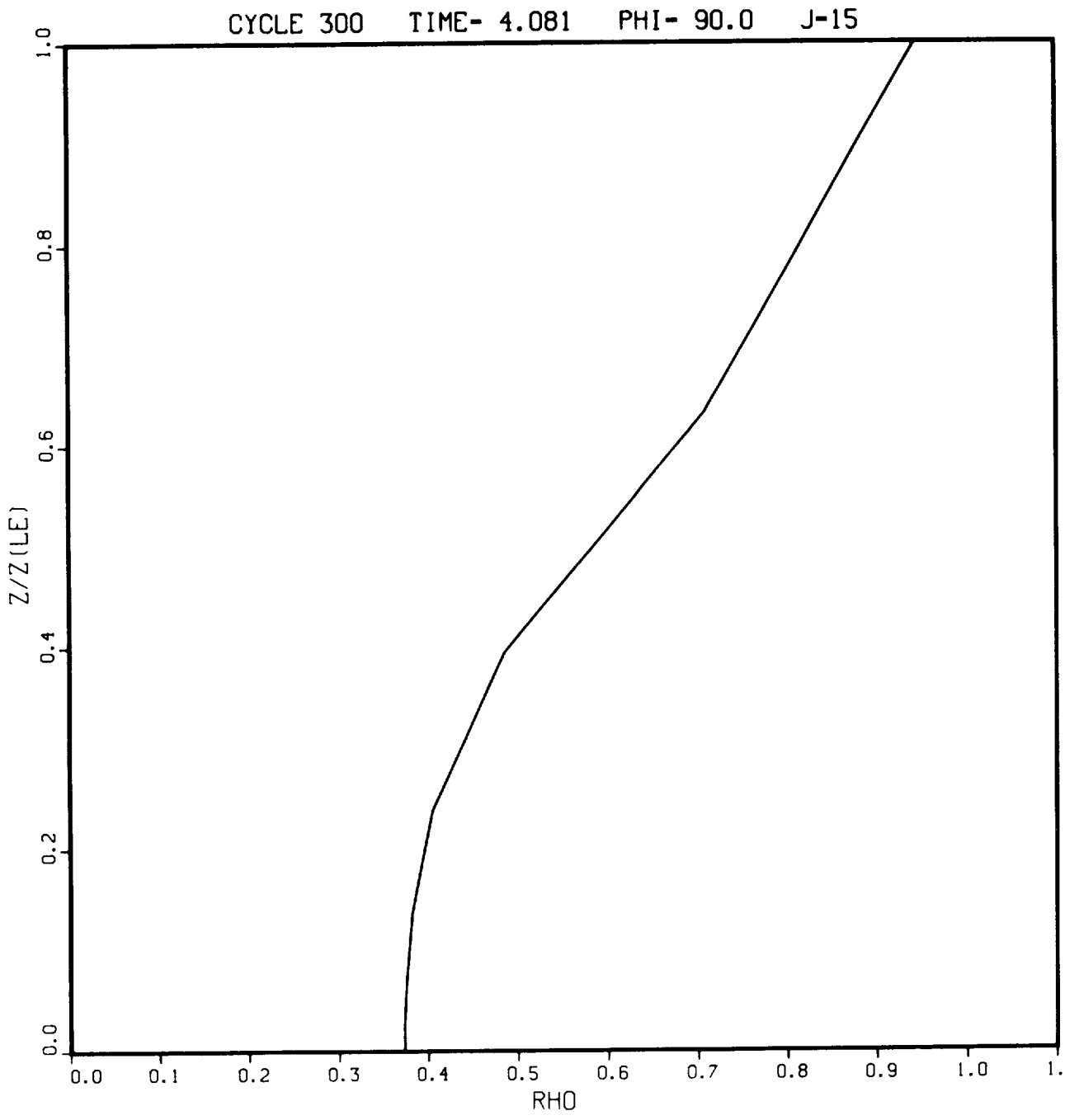

Fig. 5-20 Density Profile Across Inner Viscous Layer at Trailing Edge, $M_\infty = 3$

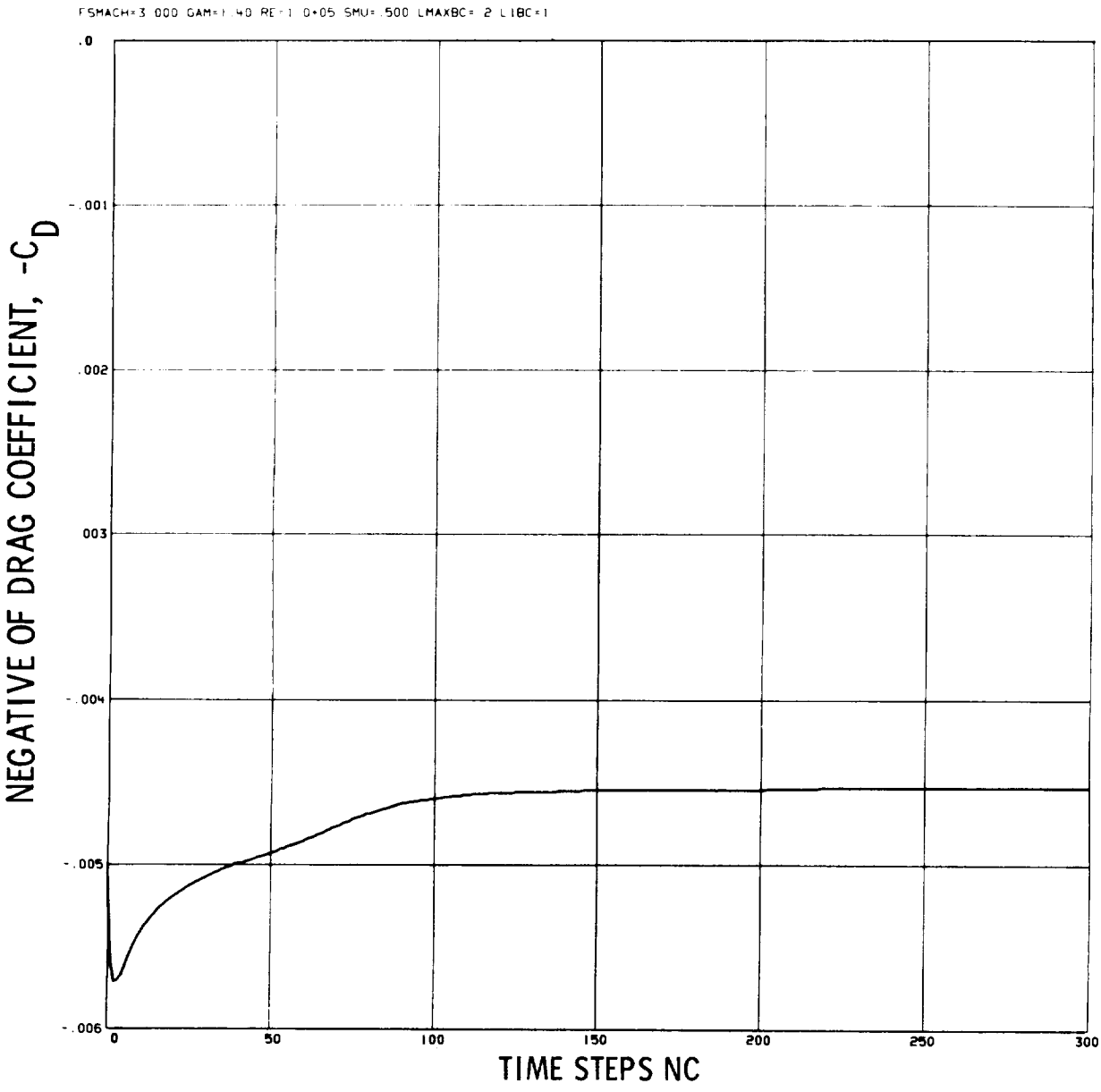

Fig. 5-21 Drag Coefficient as a Function of Number of Time Steps, $M_\infty = 3$. Maximum Courant No. Co = 100

From these numerical experiments, we conclude that the described procedures for computing the flow at outflow boundaries and at freestream boundaries are valid over the whole range of subsonic, transonic, and supersonic flow conditions. The numerical experiments played a vital role in the final formulation of the boundary conditions presented in Section 2.4, and in the development of the boundary point difference equations presented in Section 4.2.

5.3 EFFECT OF SMOOTHING TERMS ON THE SOLUTION

Numerical experiments also have been performed to explore the effects of various types of explicit smoothing terms on the solution. Both the conservative smoothing terms of Section 4.3 and the nonconservative terms of Refs. 3, 7, and 13 have been tested. In general, the conservative smoothing terms have been found to be superior in two respects.

First, the nonconservative smoothing terms produce a substantial overshoot in both the density and the streamwise velocity component at grid points situated near the boundary layer edge, where the curvature in the profiles of these variables is greatest. That is, the values exceed the freestream values in this region. For the same value of the smoothing coefficient, the conservative smoothing terms produce much less overshoot. Some overshoot is still present, as evidenced by the profiles in Figs. 5-4 to 5-20, which were computed using the conservative smoothing terms.

Second, the conservative smoothing terms do not cause the difference equations to violate the global conservation property of the differential equations that govern the flow. This is not true of the nonconservative smoothing terms. The significance of the global conservation property became evident when we attempted to compute the drag by integrating the momentum defect over all boundaries permeable to the flow. The drag computed by this method differed by nearly a factor of two from that obtained from a direct integration of the surface stresses because of the fact that the nonconservative smoothing terms contribute errors to the global mass, momentum, and energy

balances over the flow region. The conservative smoothing terms make no net contribution to the global balances. Consequently, the drag computed by momentum defect is in agreement with that obtained by integrating surface stresses.

Section 6

TURBULENCE MODELS

6.1 INTERNAL AND EXTERNAL WALL BOUNDARY LAYERS

The boundary layer flow along the external and internal nozzle walls, as well as on the wedge plug and on the side plates, can be modeled using a two-layer eddy viscosity model which has been employed successfully in previous calculations of compressible boundary layer flows at subsonic and supersonic Mach numbers. Implicit in this model is the assumption of two-dimensional, thin shear layers in local equilibrium; i.e., the turbulent flow in the boundary layer represents local mean flow conditions. A relaxation eddy viscosity model is available and will be incorporated into the calculations in cases where streamwise pressure gradients lead to flow separation. The relaxation model accounts for the lag in turbulence response to rapid changes in mean flow conditions. The application of other turbulence models such as those of Refs. 22, 23, and 24 which entail solving differential equations for the Reynolds stresses, turbulent kinetic energy, and length scale appear not warranted in the present application. Such models do not offer significantly better performance, but only increase computational work.

With these assumptions, the turbulent stresses τ_t in the boundary layer are modeled in terms of the eddy viscosity μ_t by

$$\tau_t = \mu_t \frac{\partial U}{\partial y} \tag{6.1}$$

where U is the velocity component parallel to the wall, and y is the coordinate normal to and measured from the wall. In the inner region (also known as sublayer), μ_t is calculated from the Van Driest eddy viscosity formulation with damping in the sublayer which was modified by Cebeci et al. (Ref. 25) for the case of compressible flow

with pressure gradient,

$$\mu_t = \rho k^2 y^2 \left(1 - e^{y^+/A^+}\right)^2 \frac{\partial U}{\partial y} \tag{6.2}$$

where the damping constant A^+ depends upon the streamwise pressure gradient as

$$A^+ = 26\left(1 + \frac{y}{\rho u_\tau^2}\frac{dp}{ds}\right)^{-1/2} \tag{6.3}$$

$u_\tau = \left(\tau_w/\rho_w\right)^{1/2}$ is the friction velocity based upon the wall shear stress and density. The constant k has the value of 0.40. A slightly different expression for A^+ is obtained by replacing y in Eq. (6.3) with the sublayer thickness y_s^+ defined by

$$y_s^+ = \frac{\rho\, y_s\, u_\tau}{\mu} = 11.8 \tag{6.4}$$

so that

$$A^+ = 26\left(1 + 11.8\, P^+\right)^{-1/2} \tag{6.5}$$

where P^+ is the pressure gradient parameter

$$P^+ = \frac{\mu}{\rho^2 u_\tau^3}\frac{dp}{ds} \tag{6.6}$$

In the outer region of the boundary layer, the eddy viscosity is determined from the Clauser defect law

$$\mu_t = \frac{0.0168\,\rho}{\left[1 + 5.5\left(\frac{y}{\delta}\right)^6\right]} \int_0^{\delta} (U_c - U)\, dy \qquad (6.7)$$

U_c represents the core flow velocity at the edge of the boundary layer. Equation (6.7) includes in the denominator Klebanoff's intermittency factor (Ref. 26) in order to account for the intermittent nature of turbulent flow in the outer region of the boundary layer. The choice of Eqs. (6.2) or (6.7) is made so as to assure continuity of μ_t from the inner to the outer region. Equation (6.7) involves the core velocity U_c and the boundary layer thickness δ, both of which may not be well defined in the nozzle interior for nonuniform inlet conditions. In this case, a mass-flow averaged core flow velocity can be defined to represent the flow velocity outside the boundary layer. The boundary layer thickness δ can be defined as the distance from the wall within which the velocity or its gradient dU/dy approaches the corresponding values of the external stream to within a specified tolerance.

6.2 INTERNAL CORE FLOW

The nature of turbulence is characterized by slow response to sudden changes in rates of strain, for which reason the turbulence of the nozzle core flow is expected to undergo negligible changes during its passage through the nozzle. A constant eddy viscosity will be determined for the flow outside the boundary layer from the relationship for a round jet according to Schlichting (Ref. 20),

$$\mu_c = \kappa\, \rho\, b\, U_o \qquad (6.8)$$

where $\kappa = 0.0256$, b is the nozzle inlet radius, and U_o is the average inlet velocity. If the eddy viscosity of the core flow is considerably greater than μ_t of the outer wall region, it would be advantageous to suppress the intermittency factor in Eq. (6.7) since the eddy viscosity in this region is increased by entrainment of turbulence.

During the passage of the core flow through the nonaxisymmetric nozzle, lateral redistribution of temperature by turbulent fluctuations or diffusion will be small, but will be taken into account according to specified nonuniformities of the inlet flow. Either temperature or adiabatic boundary conditions can be specified along the nozzle wall. In either case, a constant turbulent Prandtl number of $Pr_t = 0.9$ will be used in the energy equation. This value has been shown by Cebeci (Ref. 27) to lead to excellent predictions of the boundary layer properties at various Mach numbers up to $M = 6.6$. The turbulent eddy conductivity k_t is thus defined by

$$Pr_t = \frac{\mu_t c_p}{k_t} = 0.9 \tag{6.9}$$

The wall boundary layers external to the nozzle belong to computational Region C illustrated in Fig. 6-1. They will be computed using the same eddy viscosity models described above. Although the sketched geometry does not indicate regions of separated flow, exterior flow separation may occur in the region of confluence with the interior flow. In such cases, the relaxation eddy viscosity model of Shang and Hankey (Ref. 28) can be used to correct the local equilibrium eddy viscosity model for the effects of upstream history (nonequilibrium effects) upon the development of turbulence. The model computes a nonequilibrium eddy viscosity μ_n from local and upstream values,

$$\mu_n = \mu_t + (\mu_o - \mu_t)\left(1 - \exp - \frac{z - z_o}{\lambda \delta_o}\right) \tag{6.10}$$

where the subscript "o" refers to the upstream location where an abrupt change in streamwise pressure gradient occurs. The relaxation length λ has typically a value of 2.5 to 10. In the calculations of turbulent, separated flow over axisymmetric afterbody boattail configurations by Holst (Ref. 29), best comparison with experimental data was obtained for $\lambda = 2.5$.

6.3 FREE SHEAR LAYER AND DEVELOPED JET REGION

The flow in Region B of Fig. 6-1, outside the boundary layers on the side plates, can be characterized as a two-dimensional free shear layer. This flow changes later into

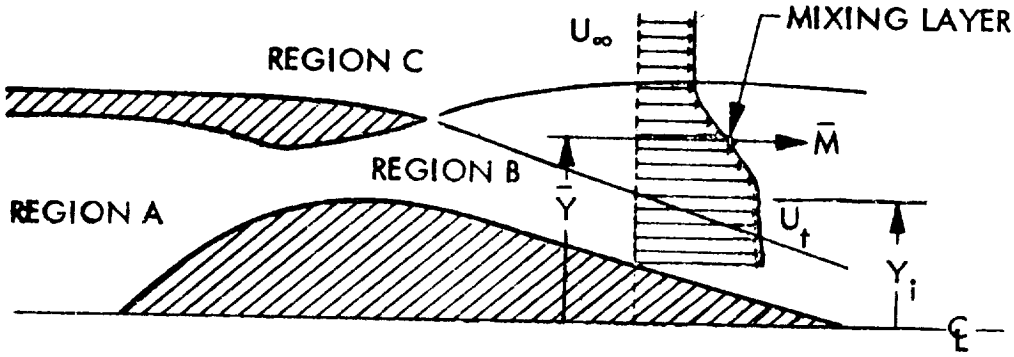

Fig. 6-1 Definition of Mixing Layer Flow in Region B

a developed free jet after the mixing layer spreads and envelopes the entire exhaust stream. Compressible shear layers of this type with differences in temperature and density across the layer have been computed successfully with eddy viscosity models where μ_t is proportional to the width of the mixing region and to a characteristic velocity. As in the case of the internal and external boundary layers, we favor the eddy viscosity approach for computational reasons over more complicated models, e.g., Varma et al. (Ref. 24). In particular, the model used by Donaldson and Gray (Ref. 30) represents a convenient and accurate method for computing the merging of the two mixing layers in regions into a single jet, although it may not be necessary to carry the computations into the fully developed turbulent region. The eddy viscosity of the mixing layers is then given by

$$\mu_t = \frac{1}{2} k (\bar{Y} - Y_i) (U_c - U_\infty) \qquad (6.11a)$$

where U_c is the maximum streamwise velocity component of Region B, and $\bar{Y}$, Y_i are coordinates measured from the nozzle centerline as indicated in Fig. 6-1. Using

the calculated and experimental data of Ref. 30, k depends upon the Mach number $\overline{M}$ at the point where the shear layer velocity equals $(U_c + U_\infty)/2$,

$$\begin{aligned} k &= 0.046 - 0.016\,\overline{M} \quad \text{for} \quad \overline{M} \leq 1.3 \\ k &= 0.025 \qquad\qquad\quad \text{for} \quad \overline{M} > 1.3 \end{aligned} \tag{6.11b}$$

The dependence of k upon M implies that the existence of a stationary shock structure in a free mixing layer has no first-order effects upon the mixing rate. If the downstream computational boundary reaches into the developed jet region, μ_t is calculated from Eq. (6.11) with $Y_i = 0$ and with U_c representing the maximum velocity in the jet.

Section 7
REFERENCES

1. Thomas, P. D.; Vinokur, M.; Bastianon, R. A.; and Conti, R. J.: Numerical Solution for Three-Dimensional Inviscid Supersonic Flow. AIAA J., vol. 10, no. 7, 1972, pp. 887–894.

2. Viviand, H.; and Ghazzi, W.: Numerical Solution of the Compressible Navier-Stokes Equation at High Reynolds Numbers With Applications to the Blunt Body Problem, Lecture Notes in Physics, no. 59, Springer-Verlag, 1976.

3. Steger, J. L.: Implicit Finite Difference Simulation of Flow About Arbitrary Geometries, AIAA J., vol. 16, no. 7, Jul. 1978.

4. Thompson, J. F.; Thames, F. C.; and Mastin, C. M.: Automatic Numerical Generation of Body-Fitted Curvilinear Coordinate System for Fields Containing Any Number of Arbitrary Two-Dimensional Bodies., J. of Comp. Physics, vol. 15, 1974, pp. 299–319.

5. Peyret, R.; and Viviand, H.: Computation of Viscous Compressible Flows Based on the Navier-Stokes Equations. AGARD-AG-212, 1975.

6. Thomas, P. D.; and Lombard, C. K.: The Geometric Conservation Law – A Link Between the Finite-Difference and Finite-Volume Methods of Flow Computation on Moving Grids. AIAA paper 78-1208, Jul. 1978.

7. Pulliam, T. H.; and Steger, J. L.: On Implicit Finite-Difference Simulations of Three-Dimensional Flow. AIAA paper 78–10, Jan. 1978.

8. Cline, M. C.: NAP: A Computer Program for the Computation of Two-Dimensional Time-Dependent, Inviscid Nozzle Flow. LA-5984, Los Alamos Scientific Laboratory, Los Alamos, N. M., Jan. 1977.

9. Shapiro, A. H.: The Dynamics and Thermodynamics of Compressible Fluid Flow, vol. I, Ronald Press, 1953.

10. Thompson, J. F.; Thames, F. C.; and Mastin, C. W.: Boundary-Fitted Curvilinear Coordinate Systems for Solution of Partial Differential Equations on Fields Containing any Number of Arbitrary Two-Dimensional Bodies. NASA CR-2729, 1976.

11. Thompson, J. F.; Thames, F. C.; Mastin, C. W.; and Shanks, S. P.: Use of Numerically Generated Body-Fitted Coordinate Systems for Solution of the Navier-Stokes Equations. AIAA 2nd Computational Fluid Dynamics Conference, Proceedings, Hartford, Conn., 1975, pp. 68−80.

12. Kumar, D.; Hester, L. R.; and Thompson, J. F.: Development of Partial Channel Flow for Arbitrary Input Velocity Distribution Using Boundary-Fitted Coordinate Systems. ASME 99th Winter Annual Meeting, Dec. 1978.

13. Beam, R.; and Warming, R. F.: An Implicit Factored Scheme for the Compressible Navier-Stokes Equations. AIAA J. vol. 18, no. 4, pp. 397−402.

14. Briley, W. R.; and MacDonald, H.: Solution of the Multidimensional Compressible Navier-Stokes Equations by a Generalized Implicit Method, J. of Computational Physics, vol. 24, 1977, pp. 372−397.

15. Thomas, P. D.: Boundary Conditions and Conservative Smoothing Operators for Implicit Numerical Solutions to the Compressible Flow Navier-Stokes Equations, LMSC-D630729, Lockheed Palo Alto Research Laboratory, Palo Alto, Ca., Oct 1978.

16. Stanton, R. G.: Numerical Methods for Science and Engineering. Prentice-Hall, Inc., 1961, chaps. 1 and 3.

17. MacCormack, R. W.; and Paullay, A. J.: The Influence of the Computational Mesh on Accuracy for Initial Value Problems With Discontinuous or Non-Unique Solutions. Computers and Fluids, vol. 2, 1974, pp. 339−361.

18. Rizzi, A. W.; and Inouye, M.: Time-Split Finite-Volume Method for Three-Dimensional Blunt-Body Flow. AIAA J., vol. 11, no. 11, 1973, pp. 1478−1485.

19. Warming, R. F.; and Beam, R. M.: On the Construction and Application of Implicit Factored Schemes for Conservation Laws. SIAM-AMS Proceedings of the Symposium on Computational Fluid Dynamics, New York, Apr. 16 – 17, 1977.

20. Schlichting, H.: Boundary Layer Theory, McGraw-Hill Book Co., 1955.

21. Van Dyke, M.: Perturbation Methods in Fluid Mechanics, Pergamon Press, New Jersey, 1964.

22. P. Bradshaw; and D. H. Ferriss: "Applications of a General Method of Calculating Turbulent Shear Layers," J. Basic Eng., vol. 94D, no. 2, 1972, pp. 345 – 351; ASME Paper No. 71-WA/FE-8, 1971.

23. K. H. Ng; and D. B. Spalding: "Turbulence Models for Boundary Layers Near Walls," The Physics of Fluids, vol. 15, No. 1, 1972, pp. 20 – 30.

24. A. K. Varma; R. A. Beddini; R. D. Sullivan; and C. DuP. Donaldson: "Application of an Invariant Second-Order Closure Model to Compressible Turbulent Shear Layers," AIAA 7th Fluid and Plasma Dynamics Conference, Palo Alto, California, 17 – 19 Jun 1974; AIAA Paper No. 74-592.

25. T. Cebeci; A. M. O. Smith; and G. Mosinskis: "Calculation of Compressible Adiabatic Turbulent Layers," AIAA J., vol. 8, no. 11, 1970, 1974 – 1982.

26. P. S. Klebanoff: "Characteristics of Turbulence in a Boundary Layer With Zero Pressure Gradient," TN 3178, Jul 1954, NACA.

27. T. Cebeci: "A Model for Eddy Conductivity and Turbulent Prandtl Number," ASME Paper No. 72-WA/HT-13, 1972.

28. J. S. Shang, and W. L. Hankey, Jr.: "Numerical Solution for Supersonic Turbulent Flow Over a Compression Ramp," AIAA J., vol. 13, no. 10, 1975, 1369 – 1374.

29. T. L. Holst: "Numerical Solution of Axisymmetric Boattail Fields with Plume Simulators," AIAA Paper No. 77-224, 1977.

30. C. DuP Donaldson and K. E. Gray: "Theoretical and Experimental Investigation of Compressible Free Mixing of Two Dissimilar Gases," AIAA J., vol. 4, No. 11, 1966, 2017 – 2025.

Appendix A

IMPLICIT OPERATOR MATRICES FOR THE VISCOUS TERMS

The elements of the operator matrix R in Eq. (4.5a) can be derived most easily as follows. We first expand the vector product terms that enter into Eq. (2.16b) for $\hat{\theta}^{(\eta)}$ and eliminate the temperature T by using the equation-of-state (2.6b). The result is

$$\hat{\theta}^{(\eta)} = \mu J \begin{bmatrix} 0 \\ \alpha_1 u_\eta + \beta_1 v_\eta + \beta_3 w_\eta \\ \beta_1 u_\eta + \alpha_2 v_\eta + \beta_2 w_\eta \\ \beta_3 u_\eta + \beta_2 v_\eta + \alpha_3 w_\eta \\ \alpha_4 (\epsilon/\rho)_\eta + (\alpha_1 - \alpha_4)(u^2/2)_\eta + (\alpha_2 - \alpha_4)(v^2/2)_\eta \\ \qquad + (\alpha_3 - \alpha_4)(w^2/2)_\eta + \beta_1 (uv)_\eta + \beta_2 (vw)_\eta \\ \qquad\qquad + \beta_3 (wu)_\eta \end{bmatrix} \tag{A.1}$$

$$\alpha_1 = |\nabla\eta|^2 + \eta_x^2/3 \qquad \alpha_2 = |\nabla\eta|^2 + \eta_y^2/3 \qquad \alpha_3 = |\nabla\eta|^2 + \eta_z^2/3$$

$$\beta_1 = \eta_x \eta_y/3 \qquad \beta_2 = \eta_y \eta_z/3 \qquad \beta_3 = \eta_z \eta_x/3$$

$$\alpha_4 = (\gamma/\mathrm{Pr})|\nabla\eta|^2$$

The corresponding equation for $\hat{\omega}^{(\xi)}$ can be obtained from Eqs. A.1 by making the substitutions $\theta, \eta \rightarrow \omega, \xi$.

Now, R denotes the Jacobian matrix operator

$$R = \frac{\partial \hat{\theta}(\eta)}{\partial \hat{q}} = J^{-1} R' \tag{A.2a}$$

$$\text{where} \qquad R' = \frac{\partial \hat{\theta}(\eta)}{\partial \vec{q}} \tag{A.2b}$$

If θ_i denotes the i'^{th} component of the vector $\hat{\theta}(\eta)$ and q_j denotes the j'^{th} component of the vector $\vec{q}$, then the elements of the matrix operator R' are

$$\left\{ r'_{ij} \right\} = \left\{ \frac{\partial \theta_i}{\partial q_j} \right\}$$

If we neglect any dependence of μ, γ, or Pr on $\vec{q}$, then the matrix elements can be computed easily after writing the quantities u, v, w in Eq. (A.1) in terms of the components of $\vec{q}$

$$\vec{q} = (\rho, \rho u, \rho v, \rho w, \epsilon)^T = (q_1, q_2, q_3, q_4, q_5)^T$$

$$u = q_2/q_1 \qquad v = q_3/q_1 \qquad w = q_4/q_1 \tag{A.3}$$

The operator matrix R' then can be written in the bordered form (cf. Ref. 7)

$$R' = \left[\begin{array}{c|ccc|c} 0 & 0 & 0 & 0 & 0 \\ \hline r'_{21} & & & & 0 \\ r'_{31} & & P & & 0 \\ r'_{41} & & & & 0 \\ \hline r'_{51} & r'_{52} & r'_{53} & r'_{54} & r'_{55} \end{array}\right] \tag{A.4a}$$

where the submatrix operator P may be written as the product of an ordinary matrix Q and a scalar differential operator

$$P = Q \frac{\partial}{\partial \eta}(1/\rho) \tag{A.4b}$$

where Q is symmetric

$$Q = \begin{bmatrix} \alpha_1 & \beta_1 & \beta_3 \\ \beta_1 & \alpha_2 & \beta_2 \\ \beta_3 & \beta_2 & \alpha_3 \end{bmatrix} \tag{A.4c}$$

The non-zero border elements of R' are given by

$$\begin{bmatrix} r'_{21} \\ r'_{31} \\ r'_{41} \end{bmatrix} = -Q \begin{bmatrix} \frac{\partial}{\partial \eta}(u/\rho) \\ \frac{\partial}{\partial \eta}(v/\rho) \\ \frac{\partial}{\partial \eta}(w/\rho) \end{bmatrix} \tag{A.4d}$$

$$r'_{51} = \alpha_4 \frac{\partial}{\partial \eta}\left[(V^2 - \epsilon/\rho)/\rho\right] - \alpha_1 \frac{\partial}{\partial \eta}(u^2/\rho) - \alpha_2 \frac{\partial}{\partial \eta}(v^2/\rho) - \alpha_3 \frac{\partial}{\partial \eta}(w^2/\rho)$$
$$- 2\beta_1 \frac{\partial}{\partial \eta}(uv/\rho) - 2\beta_2 \frac{\partial}{\partial \eta}(vw/\rho) - 2\beta_3 \frac{\partial}{\partial \eta}(wu/\rho)$$

$$\begin{aligned} r'_{52} &= -r'_{21} - \alpha_4 \frac{\partial}{\partial \eta}(u/\rho) \\ r'_{53} &= -r'_{31} - \alpha_4 \frac{\partial}{\partial \eta}(v/\rho) \\ r'_{54} &= -r'_{41} - \alpha_4 \frac{\partial}{\partial \eta}(w/\rho) \\ r'_{55} &= \alpha_4 \frac{\partial}{\partial \eta}(1/\rho) \end{aligned} \tag{A.4e}$$

The operator notation employed in Eqs. (A.4) is to be interpreted as follows. For example, the final term that appears in the fifth component of the vector $R^n \Delta\hat{q}$ of Eq. (4.5a) is the term

$$\left(r'_{55}\right)^n \Delta q_5 = \alpha_4 \frac{\partial}{\partial \eta} (1/\rho^n) \Delta\epsilon \tag{A.5}$$

The latter signifies the differential operator $\alpha_4 \frac{\partial}{\partial \eta}$ operating on the product of $1/\rho^n$ and $\Delta\epsilon$

$$\alpha_4 \frac{\partial}{\partial \eta} (1/\rho^n) \Delta\epsilon \equiv \alpha_4 \frac{\partial}{\partial \eta} \left(\frac{\Delta\epsilon}{\rho^n}\right) \tag{A.6}$$

The elements s_{ij} of the matrix operator S can be obtained from Eqs. (A.4) by the simple substitution $\eta \rightarrow \zeta$.

1. Report No.	2. Government Accession No.	3. Recipient's Catalog No.
NASA CR-3147		

4. Title and Subtitle	5. Report Date
Numerical Method for Predicting Flow Characteristics and Performance of Nonaxisymmetric Nozzles - Theory	September 1979
	6. Performing Organization Code

7. Author(s)	8. Performing Organization Report No.
P. D. Thomas	LMSC-D633457
	10. Work Unit No.

9. Performing Organization Name and Address	11. Contract or Grant No.
Lockheed Missiles and Space Company, Inc. Palo Alto Research Laboratories Palo Alto, CA 94304	NAS1-15084
	13. Type of Report and Period Covered
12. Sponsoring Agency Name and Address	Contractor Report
National Aeronautics and Space Administration Washington, D.C. 20546	14. Sponsoring Agency Code

15. Supplementary Notes

Langley Technical Monitor: Lawrence E. Putnam

Topical Report

16. Abstract

The report presents the theoretical foundation and formulation of a numerical method for predicting the viscous flowfield in and about isolated three-dimensional nozzles of geometrically complex configuration. High Reynolds number turbulent flows are of primary interest for any combination of subsonic, transonic, and supersonic flow conditions inside or outside the nozzle. An alternating-direction implicit (ADI) numerical technique is employed to integrate the unsteady Navier-Stokes equations until an asymptotic steady-state solution is reached. Boundary conditions are computed with an implicit technique compatible with the ADI technique employed at interior points of the flow region.

The equations are formulated and solved in a boundary-conforming curvilinear coordinate system. The curvilinear coordinate system and computational grid is generated numerically as the solution to an elliptic boundary value problem. A new method is developed that automatically adjusts the elliptic system so that the interior grid spacing is controlled directly by the a priori selection of the grid spacing on the boundaries of the flow region. Results are presented from numerical experiments that have been conducted to verify the principal aspects of the numerical method. A discussion is given of turbulence models that apply in the various subregions of the flowfield that have phenomenologically different flow structure.

17. Key Words (Suggested by Author(s))	18. Distribution Statement
Nozzle Afterbody Flow Navier-Stokes Equations Jet Interactions Transonic Speeds Implicit Numerical Method	Unclassified - Unlimited Subject Category 02

19. Security Classif. (of this report)	20. Security Classif. (of this page)	21. No. of Pages	22. Price*
Unclassified	Unclassified	110	$6.50

* For sale by the National Technical Information Service, Springfield, Virginia 22161

NASA-Langley, 1979